System Analysis and Test Bed for an Air-Breathing Electric Propulsion System

Master Thesis
from
B.Sc. Francesco Romano

Supervised by:
Dr. Georg Herdrich, Universität Stuttgart
Dipl.-Ing Bartomeu Massutí Ballester, Universität Stuttgart
Dr. Tony Schönherr, University of Tokyo
Dr. Daniele Pavarin, University of Padua

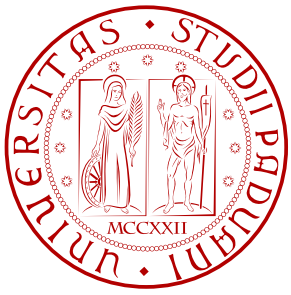

Università degli
Studi di Padova

Institut für
Raumfahrtsysteme

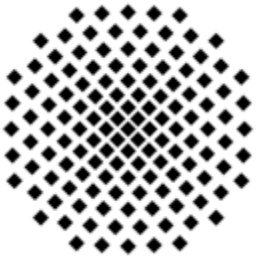

Universität Stuttgart

This is the goal: to make available for life every place where life is possible.
To make inhabitable all worlds as yet uninhabitable, and all life purposeful.
Hermann Oberth, Man Into Space, 1957.

Dedicated to my father Claudio and my mother Maria, to my brothers Luca, Matteo, Paolo and to my sister Silvia.

Contents

List of Figures **vii**

List of Tables **ix**

List of Symbols **xi**

Abstract **xv**

1 Introduction **1**

2 Overview **3**

3 Space Propulsion **5**
3.1 Current Technologies 5
3.1.1 Chemical Propulsion 6
3.1.2 Electric Propulsion 6
3.2 Discussion 10
3.3 Air-Breathing Electric Propulsion 12
3.3.1 General Concept 12
3.3.2 State of the Art 13
3.3.3 Comparison 19
3.4 Thruster Selection 21

4 System Analysis **23**
4.1 Atmospheric Model 23
4.2 Orbit 26
4.3 S/C's Temperature 29
4.4 Air Intake 33
4.5 Drag 35
4.5.1 Knudsen number 36
4.5.2 Continuum 38
4.5.3 Free Molecular Flow 42

4.5.4 Drag Calculation 43
4.6 Power Supply 47
4.7 Thrust Profile 50

5 Inductively Plasma Generation 53
5.1 Plasma 53
5.2 Inductively Coupled Plasma Generation 54
5.3 Research on IPG 55
5.4 IPG6-S Facility 56
5.4.1 Generator 57
5.4.2 Power Supply 60
5.4.3 Vacuum Subsystem 61
5.4.4 Cooling Subsystem 64
5.4.5 Gas Supply 69
5.4.6 Cavity Calorimeter 70
5.4.7 Plasma Jet Condition 71

6 Experimental Set-Up and Results 73
6.1 Experimental Set-Up 73
6.1.1 Gas Input 73
6.1.2 Mass Flow 74
6.1.3 Screen Voltage 74
6.2 Experiment Procedure 75
6.3 Experimental Results 76
6.3.1 Anode Power 76
6.3.2 Anode Current 78
6.3.3 Tank and Injector Pressure 79
6.3.4 Calorimeter Power 81
6.3.5 Total Efficiency 82
6.3.6 Exhaust Velocity 84
6.3.7 Thrust 88
6.3.8 Thrust Density 92
6.3.9 Thrust to Drag Ratio 93

7 Summary 99

8 Acceleration Strategies 101

Prospect and Improvements 105

Bibliography 106

Acknowledgements **113**

A. Diagrams **114**

B. Matlab scripts **116**
8.1 Molar Mass Script . . . 117
8.2 Temperature and Heat Flux Calculation . . . 118
8.3 Knudsen Number Calculation . . . 119
8.4 Drag Calculation Script . . . 120
8.5 Solar Array . . . 121

C. Experiments Data **122**
8.6 Low Mass Flows Air . . . 123
8.6.1 0.550 kV . . . 123
8.6.2 0.850 kV . . . 124
8.6.3 1.000 kV . . . 124
8.7 Low Mass Flows Oxygen . . . 125
8.7.1 0.550 kV . . . 125
8.7.2 0.850 kV . . . 125
8.7.3 1.000 kV . . . 126
8.8 High Mass Flows Air . . . 126
8.8.1 0.550 kV . . . 126
8.8.2 0.850 kV . . . 127
8.8.3 1.000 kV . . . 127
8.9 High Mass Flows Oxygen . . . 127
8.9.1 0.550 kV . . . 127
8.9.2 0.850 kV . . . 128
8.9.3 1.000 kV . . . 128
8.10 Checklist . . . 130
8.10.1 Operation Checklist . . . 130
8.10.2 Emergency Checklist . . . 133

D. Drawings **134**
8.11 Plexiglas Case . . . 137
8.12 Adapter . . . 139
8.13 Water Cooled Bottom Flange . . . 141
8.14 Closure of the Water Cooled Bottom Flange . . . 143

List of Figures

1.1 Earth from the International Space Station. 1

3.1 F-1 engine, Saturn V and their engineer Wernher von Braun. . . . 5
3.2 "Copernicus" Nuclear Thermal Rocket. 6
3.3 TALOS Arcjet operating with Ammonia, Universität Stuttgart. . 7
3.4 Ion and Hall Thruster Operating. 8
3.5 ZT1 MPD at 6 kW and 10 mg/s. 9
3.6 JAXA proposal for RAM-EP 12
3.7 ESA's RAM-EP proposal 14
3.8 Small S/C with EP proposal 15
3.9 RAM-EP system proposal from Shabshelowitz 15
3.10 RAM-EP HET proposal from Pekker, Keidar. 16
3.11 ESA's rendering of GOCE in orbit 17
3.12 MABHET S/C concept 18
3.13 JAXA proposed intake 19
3.14 JAXA Air-Breathing Ion Engine 19

4.1 Numerical density of atmospheric components as a function of altitude. 24
4.2 Atmosphere density as a function of altitude and solar/geomagnetic activity 25
4.3 Molar mass of atmosphere as a function of altitude. 26
4.4 VLEO and LEO altitude range 26
4.5 Orbital Velocity in VLEO. 27
4.6 Atmospheric Density ρ vs Altitude from NRLMSISE-00 model. . . 28
4.7 Temperature and heat flux vs. altitude of a flat plate orbiting Earth. 31
4.8 JAXA's proposed S/C and intake 33
4.9 Mass Flow $\dot{m}$ vs Altitude, $A_{inlet} = 1\,\mathrm{m}^2$. 34
4.10 Mass Flow $\dot{m}$ vs Altitude, $A_{inlet} = 0.3\,\mathrm{m}^2$. 35
4.11 Knudsen number vs Altitude for different mean lengths. 37

4.12 Detail Knudsen number vs Altitude for different mean lengths and solar activity. . . . 38
4.13 Physical drag coefficient for a spherical satellite as a function of altitude and solar activity . . . 39
4.14 Light-ray and 1/S shadow lines . . . 40
4.15 Investigated attitude motions . . . 41
4.16 Drag in continuum flow vs Altitude. . . . 44
4.17 Drag vs Altitude, free flow and continuum, $A_f = 1\,\mathrm{m}^2$. . . . 45
4.18 Drag vs Altitude, free flow and continuum, $A_f = 0.3\,\mathrm{m}^2$. . . . 46
4.19 Thrust to Drag ratio vs altitude in continuum, $A_f = 1\,\mathrm{m}^2$. $A_f = 0.3\,\mathrm{m}^2$ shows the same values. . . . 51
4.20 Thrust to Drag ratio vs altitude in FMF, $A_f = 1\,\mathrm{m}^2$. . . . 52
4.21 Thrust to Drag ratio vs altitude in FMF, $A_f = 0.3\,\mathrm{m}^2$. . . . 52

5.1 Reentry plasma from inside of Gemini 2, 19 January 1965. . . . 53
5.2 Electrodynamic relations in an IPG . . . 55
5.3 The IPG6-S facility. . . . 56
5.4 IPG6-S Generator mounted on the Vacuum Chamber . . . 57
5.5 The 5.5 turns coil. . . . 59
5.6 New water-cooled bottom flange. . . . 60
5.7 Assembly of bottom flange, adapter, and vacuum chamber. . . . 60
5.8 3D model view of the vacuum tank. . . . 61
5.9 Pressure in the vacuum tank vs mass flow. . . . 62
5.10 Pressure in the vacuum tank for different mass flows. . . . 63
5.11 Facility cooling system . . . 65
5.12 New valve assembly for the water cooling system. . . . 66
5.13 New water connections for the bottom flange. . . . 68
5.14 IPG6-S Calorimeter. . . . 70
5.15 Plasma leaving the generator. . . . 71

6.1 Experimental Set-Up. . . . 74
6.2 Anode Power vs Mass Flow, Air. . . . 77
6.3 Anode Power vs Mass Flow, Oxygen. . . . 77
6.4 Anode Current vs Mass Flow. . . . 78
6.5 Anode Current vs Mass Flow. . . . 79
6.6 Pressure ratio p_{inj}/p_{tank} vs Mass Flow, Air. . . . 80
6.7 Pressure ratio p_{inj}/p_{tank} vs Mass Flow, Oxygen. . . . 80
6.8 Example of temperature and P_{cal} plots for IPG6-S operating with Air at low mass flows. . . . 82
6.9 Total Efficiency for IPG6-S operating with Air at low mass flows. 83
6.10 Exhaust Velocity $A_{inlet} = 1\,\mathrm{m}^2$, Oxygen. . . . 84

6.11 Exhaust Velocity $A_{inlet} = 1\,\mathrm{m}^2$, Air. 85
6.12 Exhaust Velocity $A_{inlet} = 0.3\,\mathrm{m}^2$, Oxygen. 86
6.13 Exhaust Velocity $A_{inlet} = 0.3\,\mathrm{m}^2$, Air. 87
6.14 Thrust, $A_{inlet} = 1\,\mathrm{m}^2$, Air. 88
6.15 Thrust, $A_{inlet} = 1\,\mathrm{m}^2$, Oxygen. 89
6.16 Thrust, $A_{inlet} = 0.3\,\mathrm{m}^2$, Air. 90
6.17 Thrust, $A_{inlet} = 0.3\,\mathrm{m}^2$, Oxygen. 91
6.18 Thrust density. 92
6.19 Thrust to Drag Ratio $A_{inlet} = 0.3\,\mathrm{m}^2$, Air 94
6.20 Thrust to Drag Ratio $A_{inlet} = 1\,\mathrm{m}^2$, Air 95
6.21 Thrust to Drag Ratio $A_{inlet} = 0.3\,\mathrm{m}^2$, Oxygen 96
6.22 Thrust to Drag Ratio $A_{inlet} = 1\,\mathrm{m}^2$, Oxygen 97

8.1 Acceleration Strategies. 102
8.2 FRC Acceleration. 103
8.3 S/C Lifetime as a function of altitude, solar cycle phase, ballistic coefficient 115
8.4 Modified Plexiglas case of IPG6-S. 137
8.5 Adapter for the connection of the bottom flange to the vacuum chamber. 139
8.6 Water Cooled Bottom Flange. 141
8.7 Closure of the Water Cooled Bottom Flange. 143

List of Tables

3.1 Typical Propulsion Systems Performance. 10
3.2 Electric Propulsion Systems Performance. 11
3.3 Comparison of the RAM-EP and similar studies. 20

4.1 Estimated Operational Altitudes for a Planetary Orbital Cruiser . 29
4.2 Calculation of the S/C's temperature 30
4.3 $Kn = 1$, transition altitude for different mean lengths. 37
4.4 Drag coefficients of different attitude modes 41
4.5 C_D for the investigated studies. 42
4.6 Power vs. SA Area - EOL 48
4.7 Voltage vs. Solar String Area - EOL 48
4.8 Power obtainable from a thermionic generator of efficiency $\eta =$ 42% as a function of altitude for a surface of $A_f = 1\,\mathrm{m}^2$. 49
4.9 Drag compensation capability for IPG6-S, $c_e = 3872.98\,\mathrm{m/s}$. . . . 52

5.1 Electromagnetic and Geometric values of IPG6-S Coil. 59
5.2 VAROVAC S400F Vacuum pump specifications 62
5.3 Alcatel 2063 Vacuum pump specifications 63
5.4 PFEIFFER-Vacuum PKR 251 Pressure Gauge specifications . . . 64
5.5 PVDF characteristics. 68

6.1 Mass Flow for Tests. 75

List of Symbols

Latin Symbols

a	-, $\mathrm{m/s^2}$	Albedo's coefficient, acceleration
A	$\mathrm{m^2}$	Area
A_p	-	Geomagnetic index
B	T	Magnetic flux
c_e	m/s	Exhaust velocity
C_D	-	Drag coefficient
d	m	Distance, diameter
D	$\mathrm{C/m^2}$, N	Electric displacement field, drag force
e	$1.602\,18 \times 10^{-19}\,\mathrm{C}$	Electric charge of an electron
E	V/m, J	Electric field strength, energy
f	Hz	Frequency
F	-	Form factor
$F10.7$	SFU	Solar radio flux at $\lambda = 10.7\,\mathrm{cm}$
F_D	N	Drag force
F_L	N	Lorentz force
F_T	N	Thrust force
g_0	$9.806\,65\,\mathrm{m/s^2}$	Standard gravity
h	J/kg, km	Mean specific enthalpy, altitude
H	A/m	Magnetic field strength
I_{sp}	s	Specific impulse
i	°	Orbit inclination
I	A	Electric current
j, J	$\mathrm{A/m^2}$	Current density
k_B	$1.380\,65 \times 10^{-23}\,\mathrm{J/K}$	Boltzmann's constant
K_n	-	Knudsen number
l	m	Length
L	H, m	Inductance, mean length
m	kg	Mass
$\dot{m}$	kg/s	Mass flow rate
M	g/mol	Molar mass

n	m^{-3}	Number density
N	-	Number of coil turns
p	Pa	Pressure
P	W	Power
Q	$\mathrm{W/m}^2$	Power heat flux
q_∞	Pa	Dynamic pressure
r	m,-	Radius, molecules speed ratio
R	J/Kmol	Gas constant
R_E	$6.378\,14 \times 10^6\,\mathrm{m}$	Earth's radius
t	s	Time
T	K,N	Temperature, thrust force
v	m/s	Velocity
V	m^3,V	Volume, voltage

Greek Symbols

α	-	Absorptivity, accommodation coefficient
β	$\mathrm{kg/m}^2$	Ballistic coefficient
δ	mm	Skin depth
Δv	km/s	Velocity difference
ϵ	-	Emissivity
ϵ_0	$8.8541 \times 10^{-12}\,\mathrm{F/m}$	Electric constant
ζ	rad	Pitch angle
η	-, %	Efficiency
η_c	-, %	Collector efficiency
λ	m	Mean free path, wavelength
λ_D	m	Debye's length
π	3.14159	Pi
ρ	$\mathrm{kg/m}^3$	Density
σ	$5.6703 \times 10^{-8}\,\mathrm{W/(m^2K^4)}$, S/m	Stefan-Boltzmann's constant, electrical conductivity
σ_t	-	Tangential momentum exchange coefficient
σ_n	-	Normal momentum exchange coefficient
τ	Pa	Shear stress
ω	Hz	Frequency
Ω_E	$7.289 \times 10^{-5}\,\mathrm{rad/s}$	Earth's angular velocity

Indexes

a	Atmosphere
al	Albedo
B	Breakdown, Boltzmann
c	Collector
coil	Coil
drag	Drag
e	Exhaust, electron
f	Frontal
IR	Infra-red
inlet	Inlet
k	Kinetical
L	Lorentz
min	Minimum
max	Maximum
P/L	Payload
part	Particles
perp	Perpendicular
PI	Integral power
ref	Reference
rel	Relative
req	Required
S/C	Spacecraft
S/A	Solar array
sat	Satellite
sp	Specific
SUN	Sun
thr	Thruster
tot	Total

Abbreviations

AC	Alternate Current
ACS	Attitude Control System
circ	Circular
DC	Direct Current
DoD	Depth of Discharge
DSMC	Direct Simulation Monte Carlo
EOL	End of Life

EP	Electric Propulsion
ESA	European Space Agency
FEEP	Field Emission Electric Propulsion
FMF	Free molecular flow
GEO	Geocentric Earth Orbit
GIE	Gridded Ion Engine
GOCE	Gravity field and steady-state ocean circulation explorer
HET	Hall Effect Thruster
HHT	Helicon Hall Thruster
IPG6-S	Inductively heated Plasma Generator 6 - Stuttgart
IR	Infra-red
IT	Ion Thruster
JAXA	Japan Aerospace Exploration Agency
LEO	Low Earth Orbit
MHD	Magnetohydrodynamic
MPD	Magnetoplasmadynamic
NASA	National Aeronautics and Space Administration
PPT	Pulsed Plasma Thruster
PTFE	Polytetrafluoroethylene (Teflon®)
RAM EP	Air-Breathing Electric Propulsion
RF	Radio Frequency
RIT	Radio-frequency Ion Thruster
S/C	Spacecraft
S/A	Solar Array
SSO	Sun-Synchronous Orbit
VASIMR	Variable Specific Impulse Plasma Rocket
VEGA	Vettore Europeo di Generazione Avanzata
VLEO	Very Low Earth Orbit

Abstract

Electric space propulsion was conceived as a more efficient and suitable propulsion system in size for medium-size and small-satellite missions compared to conventional chemical engines. Very challenging types of mission scenarios include those in Earth orbit (i.e., LEO, GEO), where the residual atmosphere, especially at low altitudes, creates significant drag to spacecrafts and forces their orbit to decay. For drag compensation propulsion systems are used requiring on-board propellant and electric power. Enhancing the lifetime of Earth-orbiting satellites without any substantial increase in costs is an important objective for governmental as well as commercial operators.

An air-breathing electric propulsion system (RAM-EP) ingests the air of the residual atmosphere through a mechanical intake and uses it as propellant for an electric thruster. This system theoretically allows a S/C to orbit for an unlimited time without carrying propellant on board. Moreover, with such a propulsion system, a new range of altitudes (120-250 km) can be accessed, filling the gap between ramjet atmospheric propulsion and low Earth orbit - LEO - space propulsion, thereby enabling many new scientific missions.

Preliminary studies have shown that the propellant flow necessary for electrostatic propulsion exceeds the available mass intake with reasonable limits, and that electrode erosion due to aggressive gases, such as oxygen, which is highly present in LEO, might limit thruster efficiency and lifetime. The electrode-less design of inductive plasma generators or IPGs can handle those aggressive gases with no harmful effects. Characterisation of such plasma generators using pure O_2 and CO_2 gases exists and shows highly electric-to-thermal coupling efficiencies [1].

A system analysis is shown within this work to derive the main design drivers for a RAM-EP mission application. Atmospheric modelling, orbit considerations, heat fluxes, drag force, air intake, and available mass flow for a wide altitude range have been investigated. Preliminary results show that partial to full drag compensation is possible. The small-scale inductive plasma generator IPG6-S of the University of Stuttgart is continually improved, and is used as a test bed for a RAM-EP system using an IPG source. A set of mass flows has been defined, depending on altitude, inlet area, and intake efficiency to simulate relevant mission conditions. IPG6-S has been tested for mass flow rates between 220 mg/s down to 0.25 mg/s with air and pure oxygen. The mean mass-specific energies of the plasma plume were assessed and are used to estimate the exhaust velocities for the system analysis of the RAM-EP concept.

Chapter 1

Introduction

With more than 50 years of space flight exploration, the observation of the Earth from satellites in LEO - *Low Earth Orbit* - and GEO - *Geostationary Earth Orbit* - orbits has revolutionized life on Earth, see Fig. 1.1.
Observations of the planet have allowed the development of world-scaled weather forecasts, the monitoring of the oceanic currents, of the changing of the polar ice caps, of desertification, fires and surveillance for both civil and military services.

Figure 1.1: Earth from the International Space Station [2].

Higher accuracy of the observation of our planet can be achieved by improving the resolution of the S/C's instrumentation. The improvement of the instrumentation usually means heavier and complex optics and expensive sensors assembly which results in higher costs. Improving the resolution of the instruments without increasing complexity and weight of the payload can be achieved by flying closer to Earth's surface, in the VLEO - *Very-Low Earth Orbit* -.
Furthermore this will enable the investigation of the lower layers of Earth's atmosphere with permanent measurement, providing more detailed information about the atmosphere, temperature, components, and density and filling the gap between sounding rockets and balloons, and S/Cs in LEO.

Moreover a better understanding of the Earth's gravitational field has been enabled and recently improved by higher resolution mapping of the Earth's geoid by ESA's mission GOCE - *Gravity field and steady-state ocean circulation explorer* - ended in October 2013 - orbiting as low as 229 km [3], as gravitational fields data depend on the inverse square of the distance from the planet's center.
When flying at altitudes between 100 and 300 km two main aspects must be considered for designing the mission: the first is the aerodynamic drag, and the second is the aerodynamic heating. The number of particles impacting the S/C will increase when descending in the atmosphere due to higher density. Every impact means an exchange of energy between the particle and the S/C. A part of this energy will be transferred by an exchange of motion and drag will be generated; the other part of this energy will heat up the S/C.
The generated drag will slow down the S/C and limit the mission lifetime if no thrust is provided. Therefore, to extend the mission lifetime, a propulsion system capable to compensate the drag must be provided. This system should extend the lifetime of the S/C until a maximum which will be defined by the on-board propellant, however, carrying more propellant will result in higher expenses for the mission. Extending S/C's lifetimes means also in an higher economic income as the time for generating valuable data will be longer.
In this master thesis a RAM-EP system - *Atmosphere-Breathing Electric Propulsion* for application in LEO to VLEO orbits will be investigated. This kind of propulsion system is suitable to operate in those altitudes as it uses the gases of the residual atmosphere as propellant. This might enable missions and extend mission lifetime at these altitudes, and at the same time reduce the costs as the required amount of on-board stored propellant will be smaller.
For the development of this work, the IPG6-S, a small scale inductively heated plasma generator operating at power levels of up to 20 kW available at the Universität Stuttgart, will be used as a first test-bed for the evaluation of the performances of such a propulsion system. This evaluation will be done by the measurement of the enthalpy of the plasma through a calorimeter and exhaust velocities will be estimated to obtain thrust values. The input mass flow will be varied to simulate different altitudes and different gases like air, O_2 and N_2. The values obtained will be used for the system and sensitivity analysis of drag compensation profiles.

Chapter 2

Overview

This Chapter is intended to describe the structure of this master thesis.

After the introduction in Chapter 1 and this overview in Chapter 2, Chapter 3 presents the actual space propulsion technologies, and its descriptions as well as a comparison between them. Afterwards the RAM-EP concept is presented together with a motivated choice for a RAM-EP thruster.

Chapter 4 describes the System Analysis developed for this work: it takes into account the main design drivers for a RAM-EP mission application and describes them in detail in order to better understand their influence on the design and to evidence the issues and the limitations for the application of this kind of technology.

In Chapter 5 plasma is defined as well as the inductively coupled plasma generation principle of operation. Afterwards a brief review of the actual operating IPGs is presented. Subsequently the IPG6-S facility is presented in detail and the improvements done during this work are shown.

Chapter 6 presents the experimental set-up, the test procedure and the experimental results as well as the post-processed results.

In Chapter 7 the Conclusions of the work are made.

Furthermore Chapter 8 presents a review of the current electrodeless acceleration devices which can be applied to an IPG, as an outlook for further work.

The Chapter 8 discuss in detail the improvement that are needed to the facility in order to improve experimental results.

Chapter 3

Space Propulsion

This chapter gives an overview of the different propulsion systems available and theoretically feasible for spacecrafts and satellites and explains their working principles. Afterwards a comparison between chemical and electrical propulsion is made and advantages and disadvantages are shown. A section about inductive plasma generation is introduced and intended for the reader as a motivation for the use of an IPG in RAM-EP, introducing its working principle, advantages and disadvantages in respect to the other presented technologies. In the last section Air-Breathing Electric Propulsion working principle is described. This is completed by a state-of-the-art of the actual RAM-EP and similar small S/Cs designed for orbiting in LEO and VLEO studies. An overview reassuming the different studies is presented at the end of the chapter and it is followed by a choice of the RAM-EP thruster for this work.

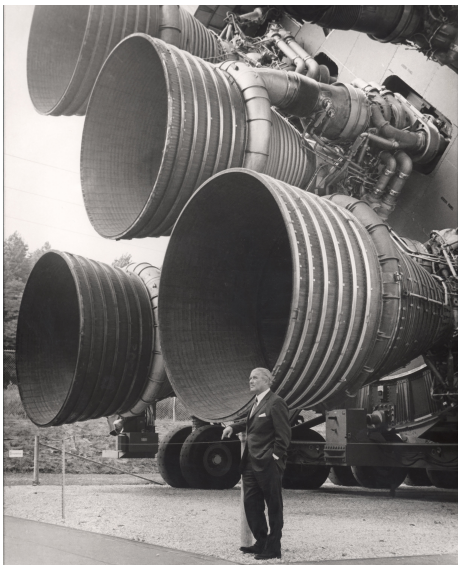

Figure 3.1: F-1 engines and their engineer Wernher von Braun [4].

3.1 Current Technologies

Since the beginning of the space age, man has developed many different kind of propulsion systems to achieve the goal of flying into space. The very first propulsion systems where chemical, with solid and liquid propellant. Afterwards electric propulsion system where investigated as a more efficient way to generate thrust, reducing the on-board propellant requirements. Hereby these two kind of propulsion system are differentiated and described.

3.1.1 Chemical Propulsion

Chemical propulsion systems, both solid and liquid, use combustion of reactants to increase temperature of the gases products and expel them through a nozzle where are accelerated, converting their thermal energy into kinetic energy, producing thrust.
This technology provides high level of achievable thrust but also high propellant consumption together with the requirement, in the case of liquid propellant, of complex and heavy subsystems like: turbo pumps, gas generator and propellant feed lines, see Fig. 3.1. A higher specific impulse, defined as $I_{sp} = \frac{F}{\dot{m} g_0}$ (F is the thrust, $\dot{m}$ is the mass flow rate and g_0 the standard gravitational acceleration on Earth), means a more efficient use of the propellant.

Nuclear propulsion systems use a nuclear reactor to heat up a working fluid, typically H_2, which is expelled and accelerated through a nozzle. As stated before, the I_{sp} is higher and exhaust velocities and thrust are higher as well, up to 900 s and 1×10^7 N for fission nuclear reactors and theoretically up to 100 000 s and 1×10^6 N with a fusion reactor. An example of this kind of propulsion applied to a mission is shown in Fig. 3.2.

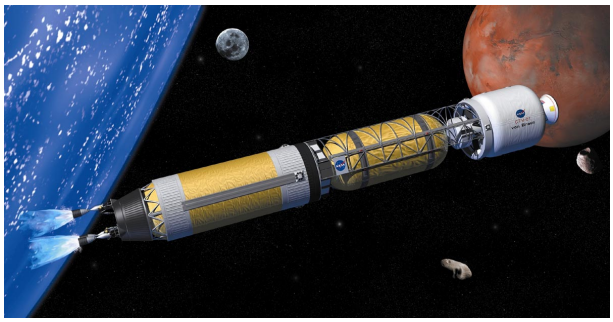

Figure 3.2: "Copernicus" Nuclear Thermal Rocket [5].

3.1.2 Electric Propulsion

Electric propulsion systems can be divided into three subcategories according to their type of acceleration strategy:

- Electrothermal: the electric power is used to heat up the propellant which expands through a nozzle;
- Electrostatic: the electric power is used to ionize the propellant and an electrostatic field is used to accelerate it;

- Electromagnetic: the electric power is used to ionize the propellant and an electromagnetic field is used to accelerate it.

Electrothermal

Under the Electrothermal subcategory there are Resistojet, and Arcjet, see Fig. 3.3.

In the first, the temperature of the propellant is increased with an arc discharge. The latter uses a combination of an heat exchanger connected to a resistive heater element which heats up the propellant that is afterwards ejected through a nozzle. They have been both well developed and already flying on different S/Cs.
Typical power consumption for Resistojet varies between 0.5 and 1.5 kW using NH_3 or N_2H_4 as propellant producing and thrust between 100 and 500 mN with a typical $I_{sp} = 300$ s. Arcjet use the same propellants and requires a power between 0.3 and 100 kW generating thrust between 200 and 2000 mN with an higher I_{sp} between 200 and 2000 s. Other kinds of propulsions system which should be mentioned under this subcategory are those of Solar, Laser and Microwave Thermal propulsion systems. The energy coming from these sources can be beamed and concentrated on an heat exchanger or on the propellant itself in order to heat it up and expel it afterwards through the nozzle.

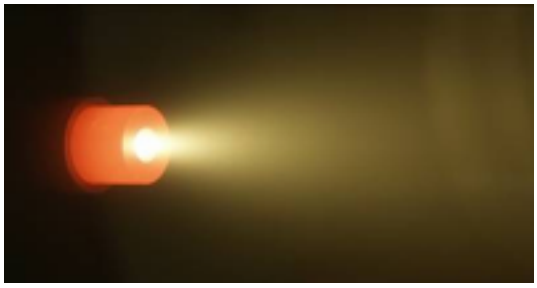

Figure 3.3: TALOS Arcjet operating with NH_3, Universität Stuttgart [6].

Electrostatic

Under the Electrostatic subcategory there are FEEP, Colloid, Laser-Accelerated, Ion and Hall Effect thrusters.

FEEP thrusters, or Field Emission Electric Propulsion thrusters extract directly and accelerate, through an electric field, atomic ions from the surface of a metal exposed to vacuum: the propellant is usually liquid metal yielding thrust

in the range from µN to mN with I_{sp} up to 12 000 s requiring acceleration voltages up to 10 kV. The result is a thrust-to-power ratio of about $60 - 75\,\mathrm{W/mN}$. Colloid thrusters accelerate through an electrostatic field droplets of an electrically charged and conducting fluid. The required power is actually very high, but studies are being conducted for reducing the power requirements for voltages below 10 kV [7].

Laser-Accelerated thrusters operate by concentrating a high intensity laser on ultrashort times (under ps) on a small spot on a surface. This generates a high temperature plasma which produces electrons at speeds close to light speed, these electrons penetrate the surface of the target generating high electric fields which can accelerates the ions out of the target surface producing thrust. The thrust generated would produce an output of 100 mN of thrust with an $I_{sp} = 1 \times 10^7$ s but requiring a huge power source of 1 MW [7].

Ion and Hall effect thrusters, Fig. 3.4(a) and Fig. 3.4(b), are at the moment the most successful thrusters, since they are already been tested and applied in various space missions. They both extract ions from the plasma with an electrostatic field and expel them at high velocity to produce thrust. Hall effect

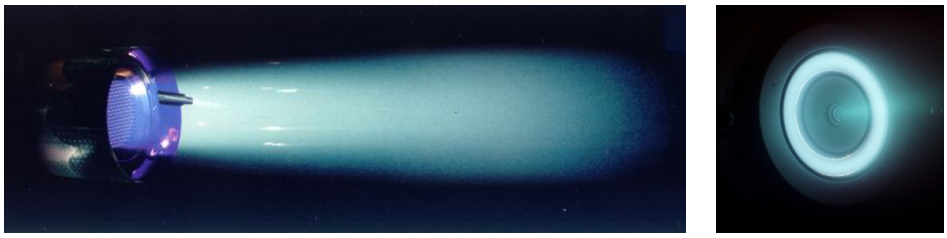

(a) Ion Thruster RIT-10 in operation with Xenon, [8].

(b) Hall Thruster in operation, [9]

Figure 3.4: Ion and Hall Thruster Operating.

thrusters require higher powers than ion thruster and yield lower I_{sp}, but they show a much higher thrust density.

Electromagnetic

Under the Electromagnetic subcategory there are Pulsed Plasma Thruster (PPT), Magnetoplasmadynamic (MPD) and Inductively Plasma Generators (IPG).

PPTs mostly use PTFE propellant bars which are crossed by an electrical discharge on the surface which causes the propellant to ablate and sublimate, the heat generated causes the resultant gas to ionize and become plasma. A charged cloud is generated and due to the force of ablation the plasma flows between an anode and a cathode completing the circuit. A current flows through the plasma generating strong magnetic fields which exerts a Lorentz's force on the plasma accelerating and expelling it out of the PPT. The use of liquid and gas propellant (H_2O and Ar) have been tested in the past on PPTs, also at IRS, [10]. Their power consumption is down to 1 W with an I_{sp} of 1000 s generating thrust up to 100 mN.

In an MPD, Fig. 3.5, the gaseous fuel is turned into plasma and sent into an acceleration chamber where magnetic and electrical fields are applied by a power source in the AF-MPD (Applied-Field) or generated by a self inducted field SF-MPD (Self-Field). Here the ionized particles are driven by the Lorentz's force which is the result of the interaction between the current flowing in the plasma and the magnetic field in the chamber. They can operate with NH_3, H and Li requiring a power between 1 and 4000 kW with an I_{sp} between 2000 and 3000 s generating thrust between 1 and 200 N.

The Variable I_{sp} Plasma Rocket, developed in the VASIMR concept, is also a kind of electromagnetic propulsion system which has been in development for decades. Ionized hydrogen is injected into the main combustion chamber through a Magneto plasma device, its magnetic field separates the plasma from the chamber's wall allowing the plasma to reach very high temperatures. In the main chamber resonant radio frequency RF fields are applied in order to heat up the plasma. The change of the RF allows the control of the I_{sp} which varies between $I_{sp} = 3000 - 30\,000$ s. It requires a power between 1 and 10 MW and generates thrust between 1 and 2 kN.

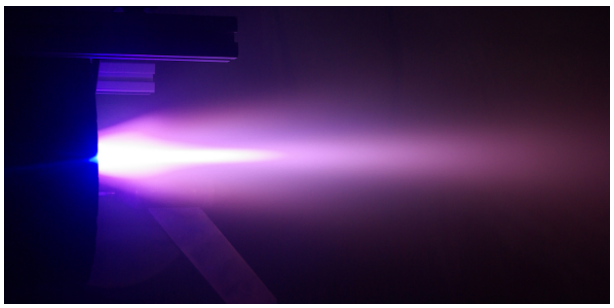

Figure 3.5: ZT1 MPD at 6 kW and 10 mg/s [11].

Inductively heated plasma generators - IPG - ionize the particles of a gas

flowing in a tube, typically made of quartz, through a coil traversed by high-frequency current which is not in direct contact with the flow. The plasma so generated is accelerated and expelled by the Lorentz body forces arising from the interaction of the plasma current and the magnetic field generated, producing thrust.
IPGs are electrodeless, this means that the lifetime and contamination issues related to electrode erosion are eliminated, as stated before this allows a wider variety of propellants for use.

Table 3.1: Typical Propulsion Systems Performance [7, p. 11].
Δv assuming $\frac{m}{m_0} = 0.1$

Propulsion System		I_{sp} s	Max. Δv km/s	Max. Thrust N
Chemical	Solid	$250 - 310$	$5.7 - 7.1$	10^7
	Liquid	$300 - 500$	$6.9 - 11.5$	10^7
Magnetohydro--dynamic (MHD)		200	4.6	10^7
Nuclear	Fission	$500 - 900$	$11.5 - 20.7$	10^6
	Fusion	10k−100k	$230 - 2300$	10^5
Electric	Electrothermal	$150 - 1200$	$3.5 - 27.6$	10^1
	Electrostatic	1.2k−10k	$27.6 - 230$	3×10^{-1}
	Electromagnetic	$700 - 5000$	$16.1 - 115$	10^2

3.2 Discussion

In the Tab. 3.1 and Tab. 3.2 a general performance chart for different kind of propulsion systems and a more specified chart for electric propulsion systems are shown.
Chemical propulsion systems should be discarded as an application for small S/C because of their high complexity, cost, weight, and limited operation time. The specific impulse is lower than other kind of propulsion system.
Nuclear propulsion has not yet flown in space and it is at this time unlikely to be applied to S/Cs mainly because of the risk of explosion during lift-off and consequent spread of radioactive products over Earth. These are big issues and the public opinion is still, at this time, against such a kind of technology.
The specific impulse for electric propulsion systems is usually higher, which means they use the propellant in a very efficient way. The power required are scalable to

Table 3.2: Electric Propulsion Systems Performance [7, p. 76].

	Thruster	Propellant	Power kW	I_{sp} s	η %	Thrust mN
Electrothermal	Resistojet	N_2H_4, NH_3	$0.5-1.5$	300	80	$100-500$
	Arcjet	N_2H_4, NH_3	$0.3-100$	$500-2$k	35	$200-2000$
Electrostatic	Ion	Xe	$0.5-2.5$	3k	$60-80$	$100-200$
	Hall	Xe, Kr, Ar	$1.5-5$	$1.5k-2$k	50	$80-200$
	FEEP	In, Cs	$0.01-0.15$	$8k-12$k	$30-90$	$0.001-1$
	Colloid	Glycerol + Add.	$0.005-0.05$	$500-1.5$k	$60-90$	$0.001-1$
	Laser acc.	Any	1000	10^7	?	$0-100$
Electromagnetic	PPT	PTFE, H_2O, Ar	$0.001-0.2$	1k	5	$1-100$
	MPD	NH_3, H, Li	$1-4000$	2k–5k	25	$1-200\,\mathrm{N}$
	Var. I_{sp} Plasma	H	$1-10\,\mathrm{MW}$	3k–3k	< 60	$1-2\,\mathrm{kN}$

application in small S/Cs as well as the components since the complexity is lower than nuclear and chemical propulsion systems. Therefore an electric propulsion system is chosen.

3.3 Air-Breathing Electric Propulsion

Air-breathing Electric Propulsion, which can be shortened as RAM-EP, is a technology which could allow thrust generation in low orbits without the need of on-board propellant, as it uses the residual gases of the atmosphere as propellant. The conventional state-of-the-art electric thrusters do not allow yet to fly at low altitudes for long period of times, usually no more than 2 years [12], because of the limitation in propellant storage and in the amount of thrust generated, which forces the S/C to decay.

3.3.1 General Concept

A RAM-EP system is basically composed by an intake and an electric thruster: the principle of operation is to use the same rarefied gases which are responsible for the generation of the drag in LEO and VLEO *(Low and Very Low Earth Orbit)*, as propellant. The use of this technology would allow S/Cs to fly at very low orbits ideally without the need of on-board propellant, allowing longer time missions in a new section of atmosphere's altitudes, interesting for scientific missions as well as military and civil surveillance services.

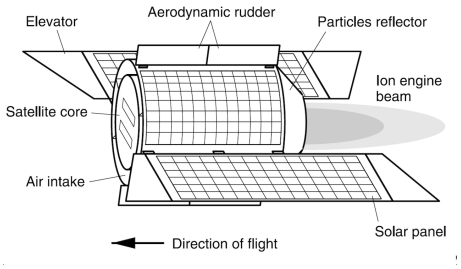

Figure 3.6: JAXA proposal for RAM-EP [13].

A special intake will be used in order to collect the gas molecules and direct them, keeping their velocity and pressure values, to the thruster. The molecules will then be ionized by the thruster and then expelled from the nozzle at a very high velocity to generate thrust. The electric power needed can be provided by the same power subsystems developed for the actual electric propulsion systems, likely a combination of solar arrays and batteries, but other kind of electric power subsystems can be considered. RAM-EP shall be able to extend the lifetime of satellites in LEO and VLEO by compensating the atmospheric drag during their time of operation. An example of such a propulsion system applied to a small S/C it is shown in the Fig. 3.6.
Not only Earth can be considered a suitable planet for this kind of propulsion

but also other planets with atmosphere, first of all Mars [14].
The main design drivers which must be taken into account when developing a S/C operating with an Air-Breathing Electric Propulsion System are defined by the orbit environment and by the S/C parameters.
The choice of the atmospheric model is an important design driver as it affects all the calculations of drag, mass flow, and mission lifetime.
The orbit is defined by the altitude, the eccentricity, and the inclination. These parameters determines the environment in which the S/C will orbit. The orbit determines the mass flow which the S/C encounters, the orbital velocity, the drag force, and the period of eclipses and sunlight during each orbit.
The S/C parameters are defined by the geometry and the subsystems performances.
The geometry determines the drag, the intake configuration determines the mass flow effectively entering in the thruster. The choice of the power subsystem will determine the thrust profile. The thruster performance and the thrust profile, together with the mass of the S/C, determines the effective mission lifetime.

3.3.2 State of the Art

A state-of-the-art research has been done through the review of different papers and studies on the topic. A summary of proposed and real missions profiles which are suitable or which take into account the use of a RAM-EP is presented subsequently. At the end of the Chapter a comparison between these studies will be done in order to estimate the mission and S/C's parameters for the System Analysis.

ESA 2007 [12]

The first case is the ESA study from 2007 which proposed a technology demonstration mission featuring a RAM-EP propulsion system [12], the system concept is shown in Fig. 3.7.
The S/C mass is of $m = 1000\,\text{kg}$ equipped with $4 \times$ ASTRIUM RIT-10 GIE (Gridded Ion Engine) operating with the incoming air molecules, which will be mostly atomic oxygen and nitrogen. For a thruster discharge chamber length of 1.0 m the collector can provide at the inlet of the thruster a pressure of $1 \times 10^{-3}\,\text{Pa}$.
The S/C is carried in space from a VEGA launcher and will be set into a circular Sun-Synchronous orbit at an altitude of $h = 200\,\text{km}$ for a duration of 7 years.
For the simulations a drag coefficient of $C_D = 2$ and a front area of $A_f = 1\,\text{m}^2$ have been assumed. The maximum power available for the propulsion system is of $P_{max} = 1\,\text{kW}$ enabling thrust of $F_T = 2$ to $20\,\text{mN}$. The solar array surface will be of $A_{S/A} = 19.74\,\text{m}^2$ to provide a power in end-of-life of $P_{EOL} = 2.9\,\text{kW}$ and

will be combined with a 612 W h Li-Ion battery. Short and long eclipse will take place (up to 16 and 29 min long) in this orbit, the power subsystem is designed to deliver enough power for thrusting up to 17 min in eclipse time.

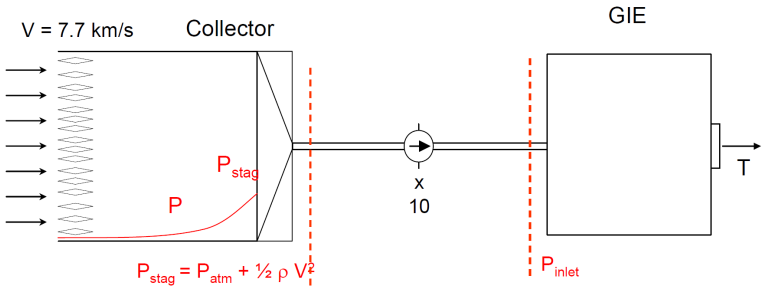

Figure 3.7: ESA's RAM-EP proposal [12].

Diamant [15]

The second presented case is from the Diamant's study [15] which suggests mission proposal for drag compensation on a small satellite at an altitude of approximately $h = 200\,\text{km}$ with a 2-stage cylindrical Hall thruster and propellant ingested from the atmosphere. The first stage is an electron cyclotron resonance ionization stage and the second stage is a cylindrical Hall thruster. A compression ratio of 500 is assumed to be achieved passively, according to [16], and would deliver to the thruster a pressure of 0.01 Pa.
The considered S/C has to provide a power of $P = 1\,\text{kW}$ to the propulsion system, the assumed frontal area is of $A_f = 0.5\,\text{m}^2$ with a $C_D = 2.2$. In this case the collector efficiency is defined, it is the ratio between the collected particle flow and the incoming particle flow and it is assumed to be $\eta_c = 35\%$.

Ceccanti, Marcuccio EP [17]

The study from Ceccanti e Marcuccio [17] proposes a mission launched by a Vega rocket with 3 small satellites with EP system for drag compensation on low altitudes, the S/C's concept is shown in Fig. 3.8. Each S/C weights 450 kg and it is intended to be set into a $h = 296-220\,\text{km}$ orbit with an inclination of $i = 96.52°$ in condition of maximum solar flux for a mission duration of 8 years. The S/C is assumed to have a front area of $A_f = 0.8\,\text{m}^2$ with a drag coefficient of $C_D = 3$. The power subsystem should provide $P = 200 - 400\,\text{W}$ with a peak of 660 W through 2 solar panels each of the size of $1 \times 2.5\,\text{m}$ together with Li-Ion battery with a 30% DoD (depth of discharge). The propulsion system is composed by 3 HET (Hall effect thrusters) of $P = 650\,\text{W}$ of nominal power operating with Xenon each with a thrust of $F_T = 40\,\text{mN}$.

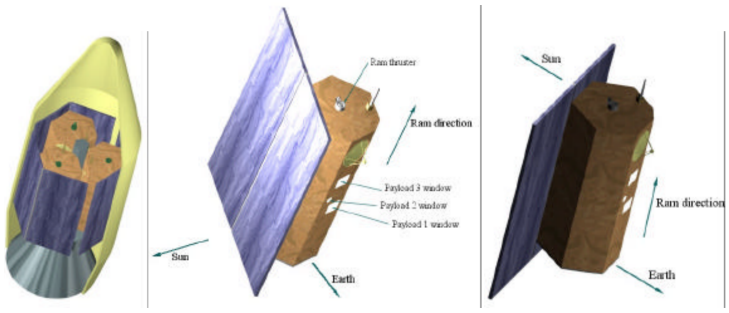

Figure 3.8: Small S/C with EP proposal from [17].

Shabshelowitz RF RAM-EP[18]

The PhD dissertation from Shabshelowitz [18] investigates RF Plasma technology applied to an Air-Breathing Electric propulsion system, the RAM-EP system concept is shown in Fig.3.9.
The S/C has a mass of $m = 325\,\text{kg}$ and it is intended to be set into a circular orbit at an altitude of $h = 200\,\text{km}$ for a mission duration of 3 years.
It is assumed a frontal area of $A_f = 0.39\,\text{m}^2$, a length of $L = 2.1\,\text{m}$, and the S/C is intended to be covered with solar cells. The ratio of the frontal area through the area reserved for the thruster inlet is of $A_f/A_{inlet} = 0.5$ and the collector efficiency is assumed to be $\eta_c = 90\%$.
The propulsion system is composed by a single-stage HHT - Helicon Hall Thruster - operating with air but provided with a tank of propellant used for ballast, see Fig.3.9, as the density of the atmosphere fluctuates.
The thruster requires a power of $P_{thr} = 306\,\text{W}$ and provides a measured thrust density of $29 - 59\,\text{mN/kW}$.

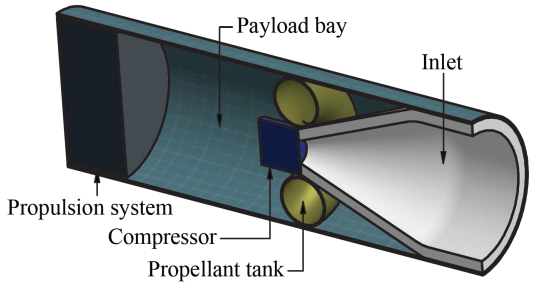

Figure 3.9: RAM-EP system proposal from Shabshelowitz [18].
Propellant line from tank to the propulsion system is not shown.

Pekker, Keidar HET [19]

The study developed by Pekker and Keidar [19] studied an HET using air of the atmosphere as propellant in the range of altitude between $h = 70 - 120\,\text{km}$.
The study investigated a S/C set into a circular orbit at an altitude of $h = 90\,\text{km}$ and $h = 95\,\text{km}$.
The gas leaving the chamber of the HHT is considered to be fully ionized and under this condition the achievable thrust is of $F_{T@90\,\text{km}} = 22\,\text{N}$ and of $F_{T@95\,\text{km}} = 9.1\,\text{N}$ with a thrust density of $13\,\text{mN/kW}$. The power required at the two altitudes is of $P_{req@90\,\text{km}} = 1.6 - 2\,\text{MW}$ and $P_{req@95\,\text{km}} = 700 - 800\,\text{kW}$.
The required power might be provided by recuperation of heat, 200 kW have been assumed to be radiate with a radiator temperature of $T = 1200\,\text{K}$ which would lead to a $1.7\,\text{m}^2$ surface for the radiator which should add only a minimum drag penalty.
The propulsion system proposed is shown in Fig. 3.10.

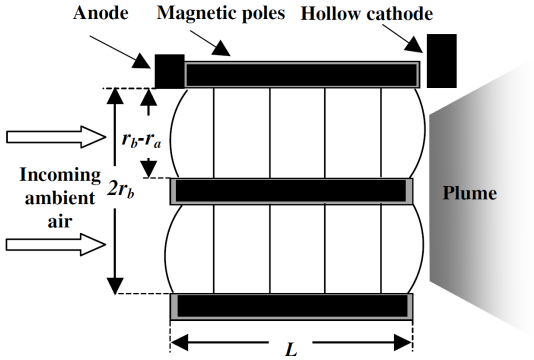

Figure 3.10: RAM-EP HET proposal from Pekker, Keidar [19].
Struts holding the center piece not shown.

GOCE [3]

The ESA's GOCE mission successfully ended last year, the mission profile would have been very suitable for a RAM-EP system application, because of the low altitude, high resolution and lifetime requirements. GOCE [3] provided global and regional models of the Earth gravity field and of the geoid with high spatial resolution and accuracy, Fig.3.11.
The S/C had a mass of $m = 1090\,\text{kg}$ and flew into a $h = 250 - 265\,\text{km}$ Sun-Sync dawn-dusk orbit for a predicted mission lifetime of $20 - 30$ months, but it reached finally 4 years of operation.
The frontal area was of $A_f = 1.1\,\text{m}^2$ with a drag coefficient used for calculations of $C_D = 3.7$ [3].

The S/C was provided with two Ion thrusters derived from the QinetiQ T5 (one for backup) operating with Xenon and providing thrust between $T = 1.5$ and 20 mN. The solar array for the power subsystems was providing $P_{EOL} = 1.6$ kW in EOL and was completed by 78 A h battery.

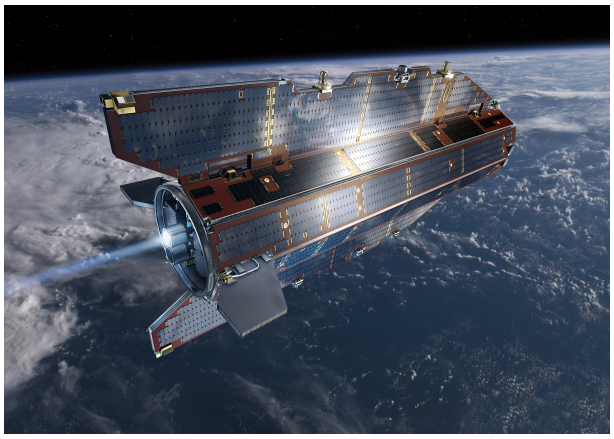

Figure 3.11: ESA's rendering of GOCE in orbit [3].

BUSEK [14]

The BUSEK company developed a study for an Air-Breathing Electric Propulsion applied to a small S/C orbiting Mars. A Final Report has been produced and have shown the feasibility of a Martian Atmosphere-Breathing Hall Effect Thruster - MABHET -, the concept of the S/C is shown in Fig. 3.12. An Hall thruster has been run with a gas mixture which reproduces the Mars atmosphere, the most present component is CO_2. The thrust to power peak ratio for an unmodified Hall thruster (designed to operate with Xenon) has been measured, with Mars-like gas mixture, to be around 30 mN/kW with a low peak of 19 mN/kW. An inlet frontal area has been assumed of $A_{inlet} = 0.15\,\text{m}^2$ considering a $C_D = 3$ because of long S/C, there is interaction with the flow on the sides of the S/C, and a frontal area $A_f = 0.30\,\text{m}^2$ double of the inlet area. The collector efficiency is required to be $\eta_c = 35\%$. Compression of the incoming air flow is required to achieve better performance of the thruster, thus a compression system should be evaluated.
The report states that MABHET may work better in Mars atmosphere than in Earth's, because of the lower density and temperature of the atmosphere and of the accommodation coefficients.

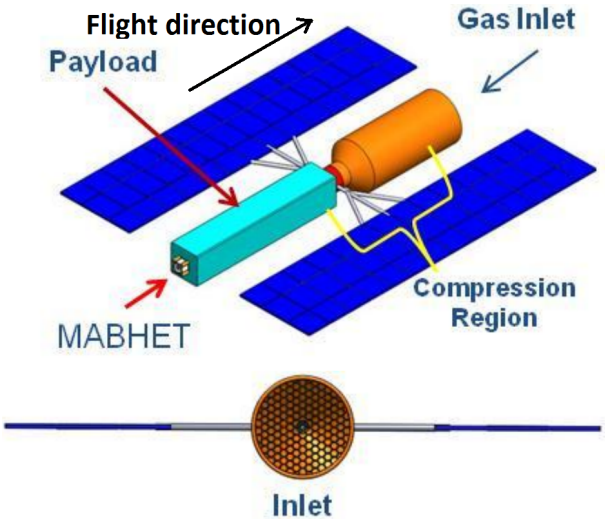

Figure 3.12: MABHET S/C concept [14].

JAXA [13], [20], [21]

The study developed from JAXA has shown a concept for an Air-Breathing Ion Engine - ABIE: the ABIE is composed by an air intake, a discharge chamber, grids, and a neutralizer. In the ABIE propulsion system, the low density atmosphere surrounding the satellite is used as propellant for the Electron Cyclotron Resonance (ECR).
Following the previous study [20] a S/C has been proposed orbiting in a SSO circular polar orbit of $h = 170\,\text{km}$ for at least 2 years. The frontal area of $A_f = 1.5\,\text{m}^2$ with a drag coefficient $C_D = 2$ and an inlet area of $A_{inlet} = 0.48\,\text{m}^2$. The propulsion system should deliver a thrust to power ratio between $10 - 14\,\text{mN/kW}$ In a subsequent study, [21], it has been verified that at an altitude of 200 km the compression of the incoming air flow obtained by the intake design shown in Fig .3.13 is enough, reaching a pressure of 0.5 Pa, to ignite the plasma inside the ECR. The altitudes of 185 and 145 km have been investigated showing a power required for the thruster, Fig. 3.14, respectively of 470 W and 3.3 kW.

A comparison of the precedent studies is shown in Tab. 3.3.

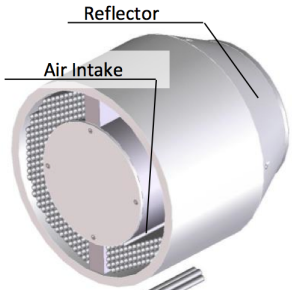

Figure 3.13: JAXA proposed intake [21].

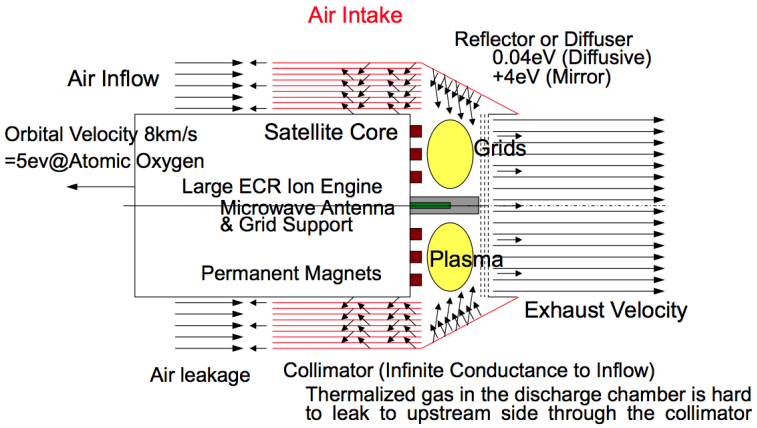

Figure 3.14: JAXA Air-Breathing Ion Engine [21].

3.3.3 Comparison

A collection of state-of-the art studies and values for the required and expected performance of the subsystems for small S/Cs orbiting in LEO and VLEO have been presented. With this first review, a range in which the research should be directed is in terms of mass, frontal area, orbit, altitude, lifetime, thrust density, power, collector efficiency, and thruster type defined.
The mass of the S/C depends on the launcher, the studies hereby presented show a mass below 1090 kg.
The frontal area reaches the maximum of 1.5 m^2 for JAXA study and the minimum of 0.30 m^2 for the BUSEK MABHET study.
The orbit of the S/C are circular and mostly with SSO, in order to get continuous power generation with solar arrays. The altitude varies between 250 and 90 km for RAM-EP application with an expected lifetime between 2 and 8 years.
The thrust density is to be between 10 and 59 mN/kW. The power generated for the S/C is between 660 W and 2.9 kW for the ESA proposal.
The collector efficiency has a minimum of 35% and a maximum of 90%, and the

Table 3.3: Comparison of the RAM-EP and similar studies.

		ESA [12]	Diamant [15]	Ceccanti, Mariuccio [17]	Shabshelowitz [18]	Pekker, Keidar [19]	GOCE [3]	MABHET [14]	JAXA [13], [20], [21]
Launcher	-	VEGA	-	VEGA	-	-	ROCKOT	-	-
S/C mass	kg	1000	-	450	325	-	1090	-	-
A_f	m^2	1	0.5	0.8	0.39	-	1.1	0.30	1.5
A_{inlet}	m^2	-	-	-	-	-	-	0.15	0.48
L	m	-	-	-	2.1	-	-	-	-
C_D	-	2	2.2	3	2-4	-	3.7	3	2
Orbit	-	SSO	circ.	circ.	circ.	circ.	SSO	-	SSO
Altitude	km	200-250	200	220-296	200	90*, 95**	250-265	-	200^{+-} 145^{+}, 185^{++}
Lifetime	years	7	-	8	3	-	4	-	> 2
Thruster	-	RIT-10 GIE	2-stage HET	HET Xe	HHT	HHT	GIT, QinetiQ T5, Xe	HET	GIT
T	mN	2-20	-	40	-	22 N* 9.1 N**	1.5-20	-	-
P_{EOL}	kW	2.9	-	max 0.66	-		1.6	-	-
$P_{thruster}$	kW	1	1	0.65	0.306	1.6-2 MW* 700-800**	-	-	3.3 kW^{+} 470 W^{++}
Power density	mN/kW	-	-	-	29-59	13	-	19-30	10-14
η_c	%	-	35	N/A	90	-	N/A	35	-
Inlet pressure	Pa	10^{-3}	0.01	N/A	-	-	N/A	-	0.5^{+-}

ideal case of 100%.
In the precedent studies Gridded Ion Engine, Hall Effect Thruster, Hall Helicon Thruster and Ion Thrusters have been considered.

3.4 Thruster Selection

In this section a selection of the thruster for RAM-EP application between the different electric propulsion systems technologies, shown in Subsection 3.1.2, will be done. The selection will be supported by the results of the State-of-the-art studies presented.

Arcjet and Resistojet suffer of erosion due to heat and the propellants used are usually oxygen-free. Their lifetime is limited and therefore an application for RAM-EP should be discarded.
MPDs, according to [22], the necessary mass flow rates for the thruster operation might be to high for a RAM-EP application.
PPTs have been tested with gas but further experimental investigation is required especially to derive the erosion of the cathode behavior. According to [22] thrust to power ratio of 6 mN/kW has been achieved with a few µg of Ar per shot. Unlike ablative PPTs the amount of injected mass can be varied independently from the energy, so an optimum ratio to be followed through different altitudes is expected [22]. However further optimization of the design might lead to better performances.
Ion thruster has been studied for RAM-EP application [20] but full thrust compensation might be not reached as the surface area of a RIT-10 is only about $0.02\,m^2$, however grid erosion was studied and long lifetime operation with oxygen can be achieved [22].
Hall thruster provides a higher thrust density when compared to ion thrusters, this means between 19 and 60 mN/kW. Problems due to erosion at the anode might arise.
In the electric propulsion systems discussed before, the main disadvantage was the presence of electrodes, or of accelerations grids which degrade and therefore decrease thruster's performance with time when using aggressive gases.
An inductive plasma generator avoid this issue by being electrode-less. As stated before, plasma is ignited by induction and the quartz tube is the only component in direct contact with the ionized gas.
This is a very good feature for a RAM-EP application.
Miniaturized inductively heated plasma sources are currently being developed within a cooperation between Baylor University (Waco, TX, USA) and the In-

stitut für Raumfahrtsysteme at Universität Stuttgart, Germany. These sources IPG6-S (Stuttgart) and IPG6-B (Baylor) are set in operation and qualification has been performed using air, oxygen and carbon dioxide [23], [1].
Tests have been successfully conducted with CO_2 and the design of both the IPG6 is suitable for operating with oxygen.
This qualifies IPG6 as a candidate fas a RAM-EP test-bed, capable to operate in environments where aggressive propellants are used, such as LEO with oxygen and Mars atmosphere with CO_2.

Chapter 4

System Analysis

This Chapter investigates the design drivers for the preliminary design of a S/C with RAM-EP application.
The Sec. 4.1 will describe the selection of the atmospheric model, afterwards Sec. 4.2 will discuss the orbit selection.
In Sec. 4.3 the calculation of the S/C's temperature depending on the altitude will be described and Sec. 4.4 will investigate the air intake and its parameters.
Sec. 4.5 will describe the calculation of the drag. The choice of the drag coefficient will be discussed as well as the calculation to determine which kind of flow should be considered.
The last two Sections, Sec. 4.6 and Sec. 4.7, will investigate the power supply for the S/C and the thrust profile for the mission.

4.1 Atmospheric Model

Many atmospheric models have been developed during the past decades, and by the time new models have been introduced and older models improved.
The model chosen for this study is the NRLMSISE-00. NRL stays for Naval Research Laboratory, MSIS stands for Mass Spectrometer and Incoherent Scatter Radar and E indicates that the model extends from the ground to space [24]. It is an empirical global model for describing the Earth's atmosphere under different conditions of solar and geomagnetic activities.
Atmospheric models provide informations about: composition, density, temperature as a function of altitude, time, geographic/geomagnetic latitude and longitude and solar/geomagnetic activity.
The output required for the system analysis is in term of numeric density for each component and temperature of the atmosphere, as function of the altitude.
Solar and geomagnetic activities are defined by two indexes: the F10.7 solar flux,

which is the solar radio flux at a wavelength of $\lambda = 10.7$ cm, and the geomagnetic index Ap. According to [22] mean solar and geomagnetic activities have been chosen by $F10.7 = F10.7_{avg} = 140$ and $Ap = 15$.
Pardini, Tobiska and Anselmo [25] estimated decay for six spherical S/Cs in orbits lower than 500 km using MSISE-90 and JR-71 atmospheric models: both of them overestimate the local air density below 350 km for low solar activity (MSISE-90 model the best with F10.7) and below 500 km for high solar activity (JR-71 model the finest with F10.7).
NRLMSISE-00 has been chosen because it is the current more accurate model for composition of the residual atmosphere in particular for VLEO, it includes also anomalous oxygen and improved modelling through further verification by in-space measurements [22].
This model is suitable for precision orbit determination and space object re-entry [24]. The element present in the model are He, O, N_2, O_2, Ar, H, N and Anomalous O, which is a combination of hot atomic oxygen O_h and atomic oxygen ions O^+. The Fig. 4.1 shows the number density of the constituents of Earth's atmosphere as a function of the altitude in conditions of mean solar (given by the $F10.7$ value) and geomagnetic (given by the A_p value) activities. The solar

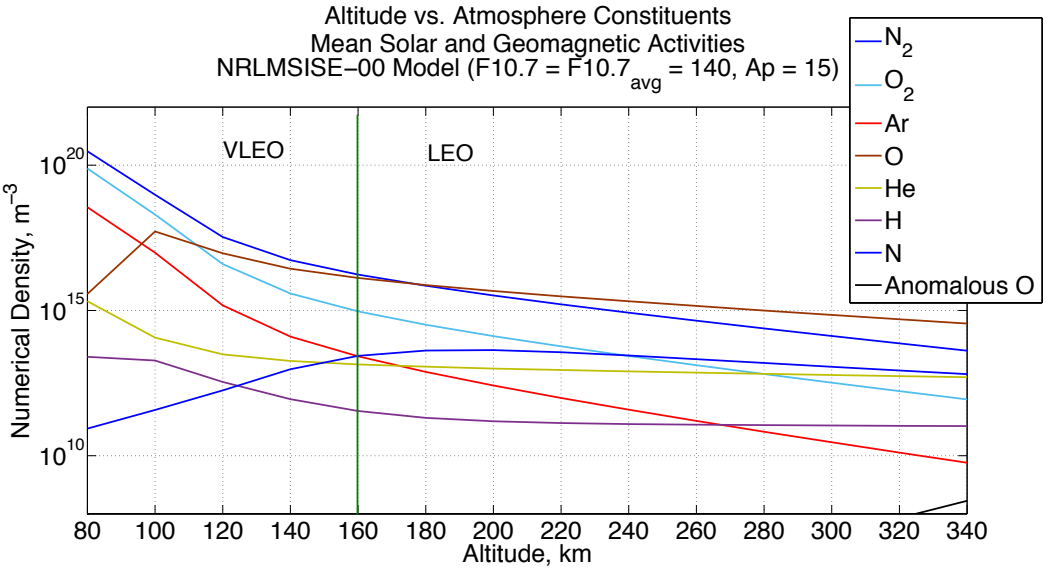

Figure 4.1: Numerical density of atmospheric components as a function of altitude.

activity influences the Earth's atmosphere, see Fig. 4.2. If the solar activity is higher, then the atmosphere is compressed by the solar wind and this leads to higher atmosphere density at the same altitude compared to low solar activity

levels. The opposite is reached with minimum solar activity. Thus, the solar cycle, which usually is 11 years long, must be taken into account in designing the mission. This effect is shown in Fig. 8.3. Considering the design of a mission in VLEO, the main atmosphere's constituents which should be taken into account are: N_2, O_2 and O. If we instead consider a mission in LEO, the main atmospheres constituents are mainly O and N_2 depending on the altitude of the orbit, since a wider altitude range is hereby possible.

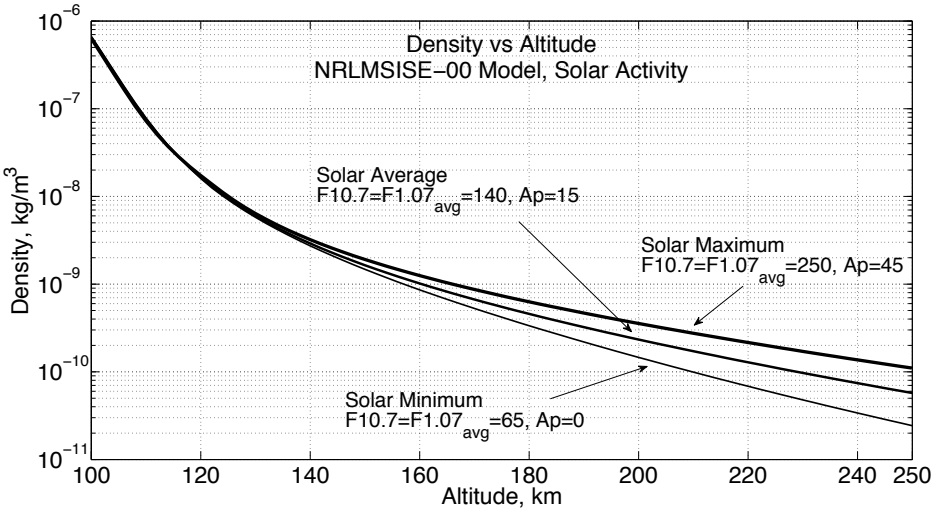

Figure 4.2: Atmosphere density as a function of altitude and solar/geomagnetic activity.

The molar mass of the atmosphere as a function of altitude, has been calculated with a Matlab script using the data of the NRLMSISE-00 model, see Appendix B, the result is plotted in the Fig. 4.3.
For this work the model has a resolution of 2 km in the altitude range 80-300 km.

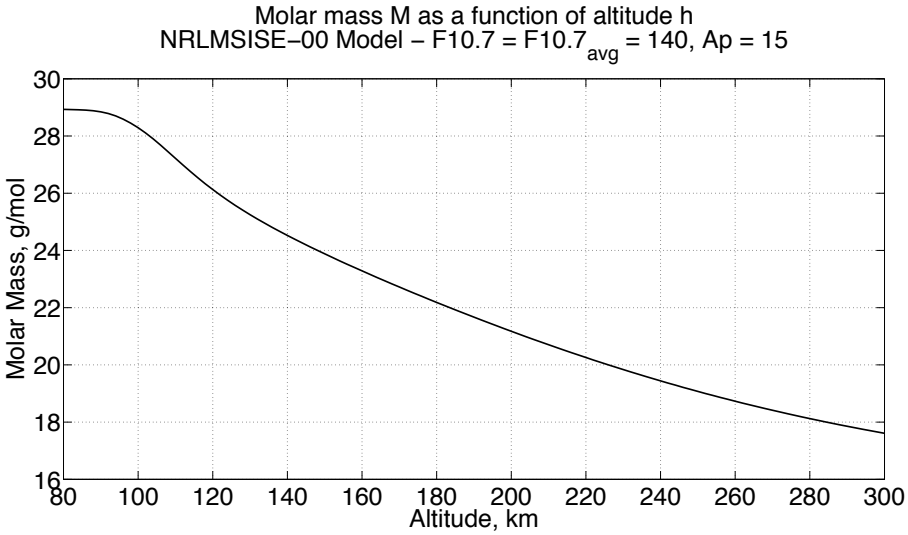

Figure 4.3: Molar mass of atmosphere as a function of altitude.

4.2 Orbit

This section will discuss the altitude ranges and the other orbit parameters suitable for a RAM-EP application.

With the altitude changes the velocity, the period of the orbit, but also the composition of the atmosphere, the density and the temperature. These parameters affects the design of the mission.
LEO extends in the range from 160 to 2000 km, VLEO from 100 to 160 km.
According to [12], altitudes for a RAM-EP system application are those below 250 km, so the upper limit is hereby set.
For orbits below 250 km, the orbital velocity can be considered constant at a value of 7.8 km/s as it is shown in the diagram in Fig. 4.5.

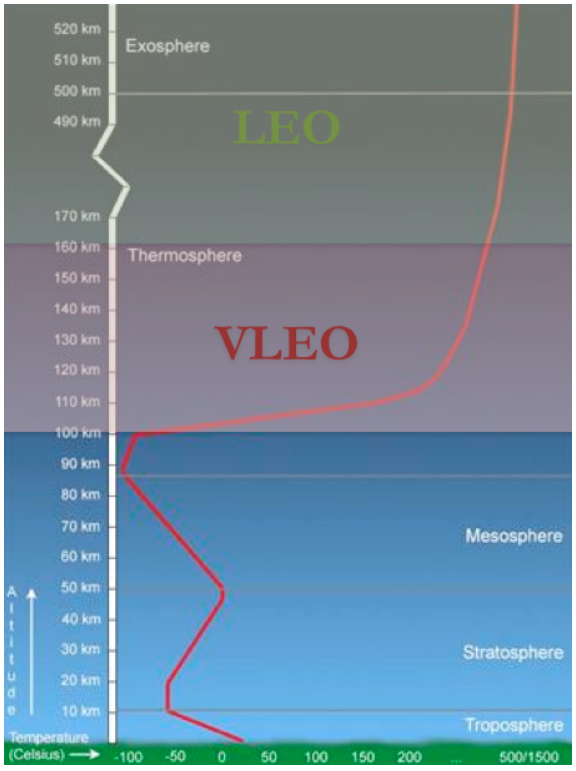

Figure 4.4: VLEO and LEO altitude range

The velocity is calculated as shown in Eq. 4.1.

$$v = \sqrt{\frac{GM}{R_E + h}} \tag{4.1}$$

Where, according to [26], GM is the geocentric constant of gravitation equal to $GM = 3.986004 \times 10^{14}$ m^3/m^2 and R_E the Earth's radius equal to $R_E = 6.37814 \times 10^6$ m and h is the altitude. The period of the orbit, T_o, is the time

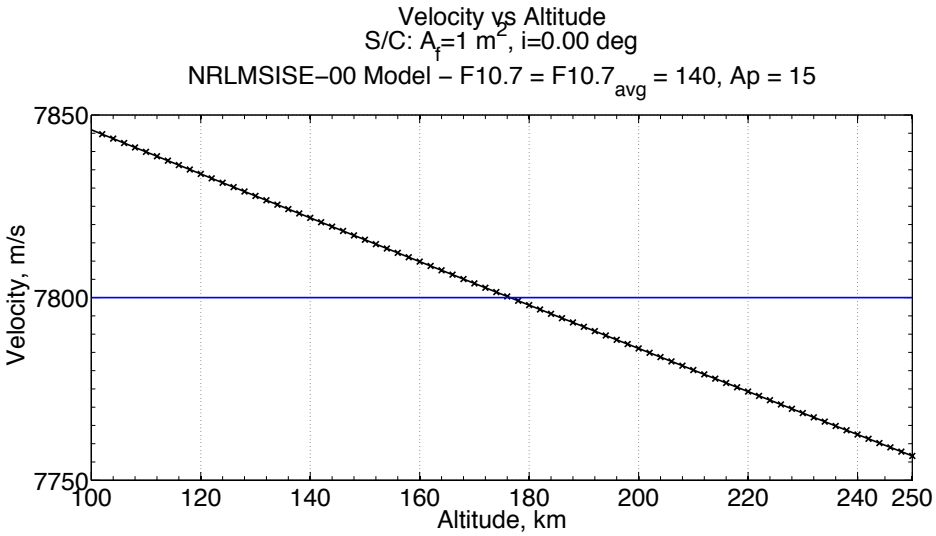

Figure 4.5: Orbital Velocity in VLEO.

which a S/C needs for one revolution around the planet. It can be divided in the time in which the S/C is illuminated by the Sun, T_s, and the time when the S/C is eclipsed by the planet, T_e. This depends on the period of the orbit, on the solar angle β and on the altitude h. The solar angle is defined as the angle between the orbital plane and the Sun vector, the vector from the center of the Sun to the Earth. β depends directly from the inclination of the orbit i, defined as the angle between the equatorial plane of the planet and the S/C's orbit.
These parameters must be investigated into detail when considering the power requirements of the S/C and of the RAM-EP system.
The power system must provide the electrical power required from the thruster and from the S/C's subsystems during the entire orbit. This can be obtained continuously, for example, with solar arrays in a Sun-Synchronous, Dawn-Dusk orbit. In this kind of orbit the S/C crosses the equator always at dawn or sunset local time, β is 90°, so that the S/C is always illuminated by the Sun and $T_s = T_o$.
The change of the density with the altitude will directly affect the drag force, and the maximum mass flow which can be collected by the intake. Important is the

fact that the density-to-altitude profile is very steep in the VLEO region, as it is shown in Fig. 4.6, and, thus, descending in this altitude range brings the S/C in a higher density atmosphere. This leads to a greater mass flow, hence, thrust produced. But this also results in a much higher drag force to compensate.

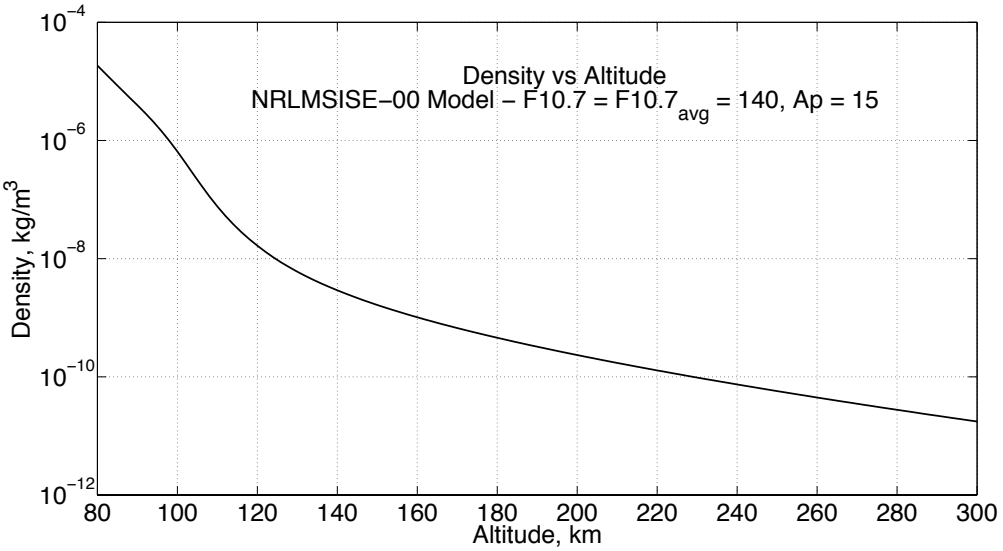

Figure 4.6: Atmospheric Density ρ vs Altitude from NRLMSISE-00 model.

The altitude of the orbit has to be chosen as an optimum condition between the power available, the required drag compensation profile, and the payload requirements (i.e. resolution required for the optical instruments).
Following Tab. 4.1, [27] is considering the altitude limits for Thermospheric Cruiser, an S/C with a RAM-EP thruster, depending on different factors. The first is for a mission lifetime of 10 years with a ballistic coefficient of 65 kg/m^2, defined as $\beta = \frac{m}{C_D A_f}$, determining a minimum operational altitude of 600 km in Earth orbit and 550 km in Mars orbit; the second is a limit due to heating effects on the S/C considered to be a flat plate normal to direction of flight, limited set to 120 km in Earth orbit and 100 km in Mars orbit; the third is considering the solar panel drag vs. the power produced for a S/C flying with solar arrays perpendicular and parallel to the flow, setting 120 and 60 km for Earth orbit and 50 and 200 km for Mars orbit.
This value, together with the maximum altitude for RAM-EP given by [12], might fix the range of altitude for RAM-EP between 120 and 250 km.

Table 4.1: Estimated Operational Altitudes for a Planetary Orbital Cruiser, [27].

Consideration	Assumptions	Earth h km	Mars h km
Ballistic Sat. Lifetime	Deorbit due to drag, 10 yr, solar max., $\beta = 65\,\mathrm{kg/m^2}$	~ 600	~ 550
Drag Heating Effects	Flat plate normal to incoming flow.	~ 120	~ 100
Solar Panel Drag vs Power Produced	Bounds placed by flat plates normal and parallel to flow.	~ 300 norm. ~ 65 par.	~ 200 norm. ~ 50 par.

4.3 S/C's Temperature

The temperature of the surfaces of the S/C must be calculated to investigate if in an hypothetical RAM-EP mission in VLEO the usual materials of which a S/C is made could withstand the environment. Moreover the calculation of the S/C's temperature is needed for the calculation of the drag in free molecular flow and for the DSMC simulations. Indeed, the temperature of the S/C's surfaces changes the interaction between particle and surface, described by the accommodation coefficient which will be introduced later.
A calculation, which confirms the limit of 120 km due to heating effects according to [27] has been done through a Matlab script, see Appendix B 8.2.
The script uses the NRLMSISE-00 model for Maximum Solar and Geomagnetic Activities, for $F10.7 = F10.7_{avg} = 140, Ap = 15$ and calculates the heat fluxes on a flat plate perpendicular to the direction of flight. The calculation has been done in the worst case scenario, the hottest. This takes into account the heating due to impact of the incoming particles, taken from the model, the heating flux coming from the Sun, the IR emission and the albedo of the Earth.
The assumption for the S/C is to be a "black body", this means that the absorptivity α and the emissivity ϵ are both equal to 1. Moreover, the S/C is assumed to be a flat plate oriented perpendicularly to the direction of flight in an orbit of $i = 0°$ inclination. The hypotheses for the calculation are following [28]. The first contribution is the power flux due to the direct Sun radiation which has a maximum value of $Q_{sun} = 1420\,\mathrm{W/m^2}$, when orbiting Earth at a distance from the Sun of 1 ua according to [29, p. 432].
The second contribution is the power flux due to the infra-red radiation coming from the Earth: this has a maximum value of $Q_{IR_E} = 275\,\mathrm{W/m^2}$ with a form factor, with the S/C orientated as above specified for altitudes below 200 km according to [29, p. 909], of $F_{IR} = 0.3476$.

This leads to a power flux due to Earth's IR radiation of $Q_{IR} = \alpha F_{IR} Q_{IR_E} = 95.5900\,\mathrm{W/m^2}$.
The third contribution is given by the reflection of the Sun's radiation on the Earth's surface, this phenomena is called albedo and it is specified by the albedo's coefficient which at this orbit with a maximum value of $a = 0.30$ in orbits between 0° and 30° of inclination; the altitude and the S/C's attitude define a form factor $F_{al} = 0.3511$ according to [29, p. 910], which leads to a power flux due to albedo of $Q_{al} = \epsilon Q_{sun} a F_{al} = 134.6117\,\mathrm{W/m^2}$.
The fourth contribution is due to the impact of the different atmosphere particles on the flat plate, called free molecular heating. From the NRLMSISE-00 model the number density of the different elements has been taken. The kinetic energy for every element has been calculated as a function of the altitude, using an average mass for the single particle of $1.67 \times 10^{-27}\,\mathrm{kg}$, the atomic number Z, different for each element, and the relative velocity v_{rel}, which is the velocity of the S/C relative to the Earth, with the hypothesis that the atmosphere rotates together with the Earth during the time.
In the Tab. 4.2 the values taken into consideration are shown :

Table 4.2: Calculation of the S/C's temperature

Contribution	Equation	Q_{ij} $\mathrm{W/m^2}$	F_{ij} -	α -	ϵ -	a -
Sun	Q_{sun}	1420	1	1	1	-
Earth's IR	Q_{IR_E}	275	-	-	-	-
	$Q_{IR} = \alpha F_{IR} Q_{IR_E}$	95.5900	0.3476	1	1	-
Albedo	$Q_{al} = \epsilon Q_{sun} a F_{al}$	134.6117	0.3511	1	1	0.30
Particle flux	$Q_{part} = \sum_{i=1}^{el} n_i v_{rel} E_{kin}$	$f(h)$	-	-	-	-
Internal flux	Q_{int}	350	-	-	-	-

The kinetic energy is finally:

$$E_{kin} = \frac{1}{2} Z m_{part} v_{rel}^2 \tag{4.2}$$

The power flux of the particles has been calculated as the product of the numerical density, the kinetic energy, and the relative velocity:

$$q_{part} = n_{part} v_{rel} E_{kel} \tag{4.3}$$

The sum of the contribution of the power flux due to the particle impacts changes with the altitude since the numerical density and the relative velocity are a function of the altitude.

The sum of all the power flux contributions is as following:

$$Q_{tot} = \sum_{i=1}^{4} Q_i = Q_{sun} + Q_{IR} + Q_{al} + Q_{part} \tag{4.4}$$

With Q_{tot} calculated in Eq. 4.4 and σ the Stefan-Boltzmann's constant the temperature of the satellite is calculated as, remembering the assumption of black body:

$$T_{sat} = \sqrt[4]{\frac{Q_{tot}}{\sigma}} \tag{4.5}$$

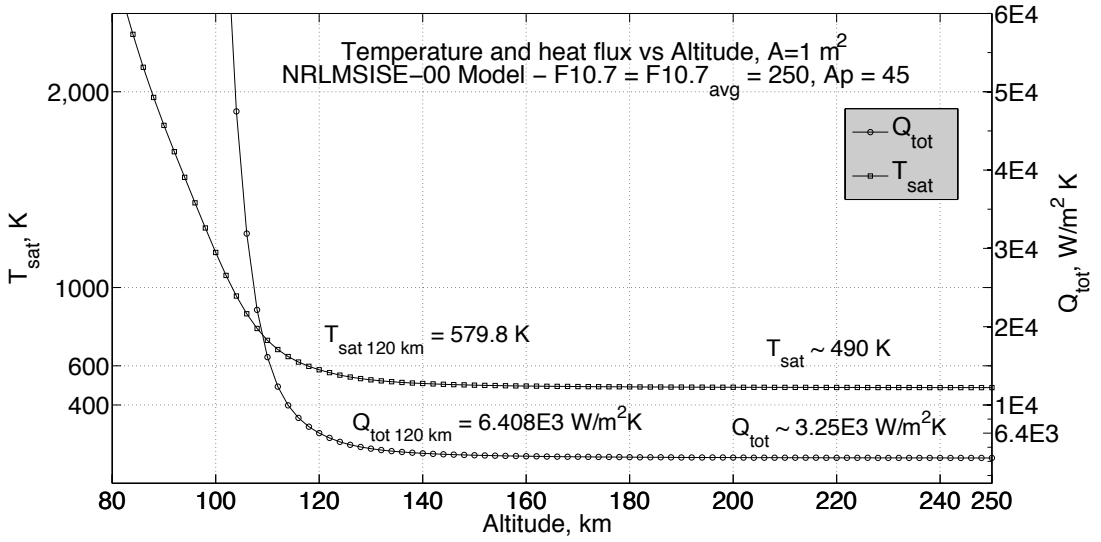

Figure 4.7: Temperature and heat flux vs. altitude of a flat plate orbiting Earth.

The assumption of "black body" does not influence much on the approximation for the calculation of the total heat flux investing the S/C, since the most predominant power flux is given by the Sun directly and in the very low altitudes of interest, since the aim is to determine the bottom limit for a RAM-EP application, by the impact of the molecules which does not depend on the emissivity and absorptivity coefficients as it is shown in Fig. 4.7.
The constant contribution of albedo, IR and Sun is of: $Q_{tot_{part}} = Q_{sun} + Q_{IR} + Q_{al} = 1650.602\,\mathrm{W/m^2}$ in the worst case.
It has to be noted that an estimation of the heat flux dissipated from the internal components of S/C should be done and added to the calculation of the total heat flux of the S/C: this would add a constant value independent from the altitude, what was intended to be shown in this chapter was how the bottom limit for the

orbiting altitude of the S/C could be set by showing the behaviour of the heat flux due to the impacting particles on the S/C. According to [29, p. 440], most S/C range between 100 and 350 $\mathrm{W/m^2}$ dissipated heat from electronics.
The maximum value of 350 $\mathrm{W/m^2}$ has been included in the calculation as the worst case.
As result, at the altitude of 120 km the temperature of the S/C is calculated to be 579.8 K with a total heat flux $Q_{tot} = 6.407 \times 10^3\,\mathrm{W/m^2}$, while at an altitude of 112 km the total heat flux would be at a value of $Q_{tot} = 1.6106 \times 10^4\,\mathrm{W/m^2}$ with a temperature of 730.05 K.
The S/C thermal control subsystem should be able to dissipate this heat in order to maintain the subsystems to their operational temperatures.
In Fig. 4.7 can be seen that an exponential increase of both temperature and heat flux starts at an altitude between $\sim 120 - 130$ km. Deeper investigation should be done on thermal analysis together with an initial design of the S/C, in order to determine a more exact critical value for maximum heat flux and temperature. The value of 120 km as a bottom limit for RAM-EP application, as proposed by [27] will be considered.
For further analysis a mean value of S/C's temperature of 490 K in RAM-EP altitude range is taken as reference for the drag calculation.

4.4 Air Intake

The functions of the intake are of collecting the air while keeping its velocity, compressing it, and driving it into the thruster. According to [22], [15], [14], a general discussion of possible intake possibilities can be made only after Direct Simulation Monte Carlo - DSMC simulations. A mechanical collector has been selected, since a magnetic one has been discarded because of the low ionization degree at low altitude orbits. A comprehensive study has been conducted from JAXA [13] considering an air-breathing ion engine. An air intake has been developed and the working principle has been experimentally verified [21]. Furthermore, according to the same source, a mass collector with a collector efficiency up to $\eta_c = 40\%$ and a compression factor of 100-200 has been achieved. A pressure of 1 mPa can be achieved at the point of injection into the thruster head. This is too little for an electrostatic thruster and on-board gas storage might be required [22].

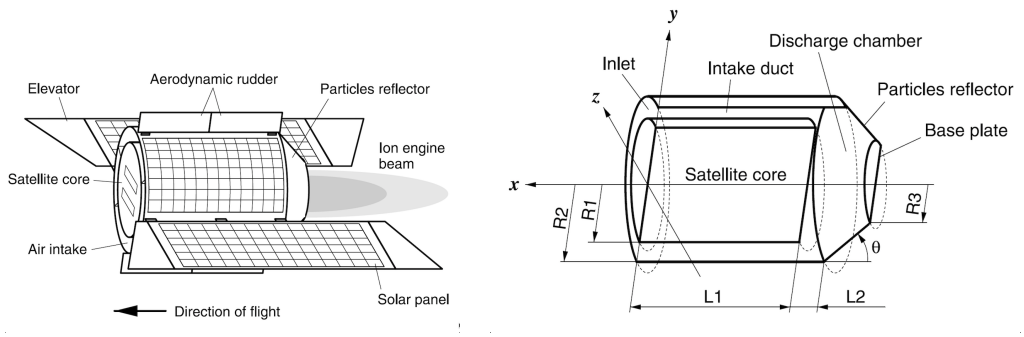

(a) The spacecraft.

(b) The intake and engine core.

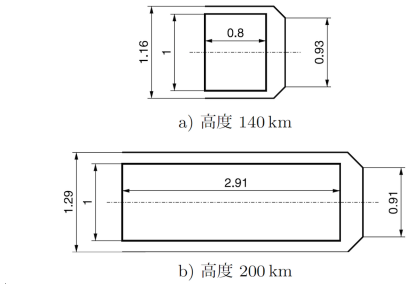

(c) Two different intakes for 140 and 200 km orbiting altitude

Figure 4.8: JAXA's proposed S/C and intake [13].

For most electric propulsion systems, pressure and density at the intake must be higher than the pressure and density of the atmosphere in which the S/C is

flying, thus, collimation for compression is needed.
Driving criteria for a RAM-EP is the mass flow which can be ingested by the air intake, this is a function of the air density, thus, of the altitude and of the collector efficiency, which is defined, see Eq. 4.6, by the ratio between the incoming particle flow, $\dot{m}_{in}$ and the particle flow ingested by the intake and flowing into the thruster, $\dot{m}_{thr}$.

$$\eta_c = \frac{\dot{m}_{thr}}{\dot{m}_{in}} \tag{4.6}$$

In Fig. 4.9, a plot of the mass flow as a function of the altitude and for three different intake frontal sections of the S/C is shown.
The mass flow to the thruster has been calculated using the data from the NRLMSISE-00 model as shown in Eq. 4.7.

$$\dot{m}_{in}(h) = \rho(h) v_{rel}(h) \eta_c A_{inlet} \tag{4.7}$$

The two different frontal area considered are the proposed Hodoyoshi 4 S/C [30] of $0.3\,\mathrm{m}^2$, and the standard size of $1\,\mathrm{m}^2$.

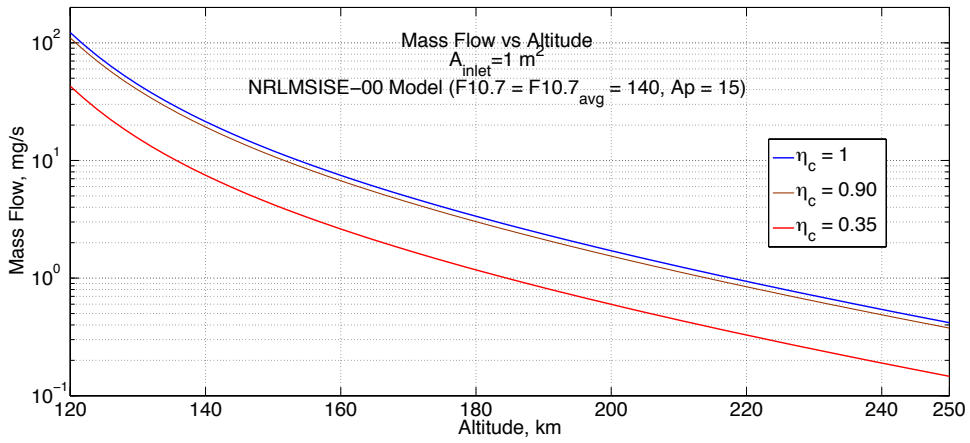

Figure 4.9: Mass Flow $\dot{m}$ vs Altitude, $A_{inlet} = 1\,\mathrm{m}^2$.

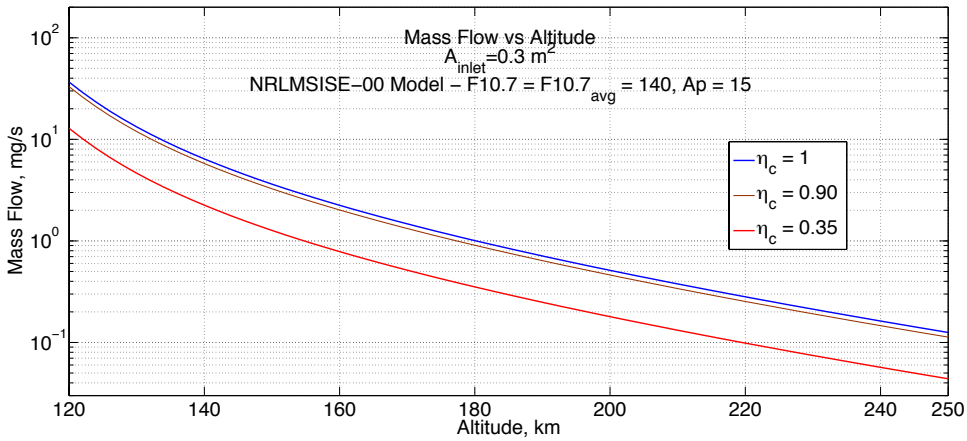

Figure 4.10: Mass Flow $\dot{m}$ vs Altitude, $A_{inlet} = 0.3\,\mathrm{m}^2$.

Another driving criteria for the design of the intake are the phenomena of sputtering, corrosion, and heat generation due to impact of particles on the wall of the intake itself, which would require the use of resistant materials and a modification of the thermal control subsystem to keep the thermal balance of the S/C.
The mass flow capability of the controllers at the facility is between 20 mg/s and 220 mg/s allowing, in best case ($A_{inlet} = 1\,\mathrm{m}^2$, $\eta_c = 1$), to simulate between 119 and 140 km and in the worst case ($A_{inlet}0.3\,\mathrm{m}^2$, $\eta_c = 0.35$), between 107 and 116 km. As this values resulted too low for the altitude limits set above, another mass flow controller has been taken in consideration providing mass flow from 20 to 1.25 mg/s allowing to simulate up to 207 km of altitude in the best case and up to 151 km in the worst case.

4.5 Drag

Drag is the force which acts on a body moving inside a flow, and it is generated by the interaction between the surface of the body and the particles in the flow. In the atmospheric drag determination for a S/C, two fundamentals operations are involved: the determination of the atmospheric density and the interaction between the S/C surfaces and the atmosphere environment. Both have the same importance in the determination of the drag.
The cause of the generation of drag is the momentum transfer from molecules in the atmosphere to the S/C. This momentum exchange depends on the mass distribution in the medium and the geometry and characteristics of the object's surface. Gravitation takes also place in the drag determination, since it results in

hydrostatic pressure and density variation in the atmosphere. However in LEO and VLEO the order of magnitude of these contributions is much lower than the drag itself and for this reason they will be neglected.
The way the drag is calculated depends of in which flow regime the S/C is flying, a different approach will be used for different flow regimes.
The two regimes which will be investigated are continuum and free molecular flow.

4.5.1 Knudsen number

The Knudsen number, named after Danish physicist Martin Knudsen (1871–1949), is a dimensionless number defined as the ratio of the mean free path length of the molecules, λ, to a representative physical length scale, L, as shown in Eq. 4.8.

$$K_n = \frac{\lambda}{L} \tag{4.8}$$

This number will be used in this section to investigate whether the flow in the RAM-EP altitude range is to be considered continuum or free molecular flow.
At the altitudes for a RAM-EP application might be that λ becomes comparable to the mean length of the S/C and, thus, the phenomena of impacts between the particles themselves and between the particles and the S/C is not anymore described by the continuum equations. To determine this, the calculation of the Knudsen number has been done.
The calculation has been done through a Matlab script, see Appendix B.
This Matlab scripts calculates the Knudsen number as a function of the altitude and the mean length of the S/C. A sensitivity analysis as been conducted with the variation of the solar activity, as it will affect the atmosphere density.
The mean free path λ is defined in Eq. 4.9.

$$\lambda = \frac{1}{\sqrt{2}\pi d^2 n} \tag{4.9}$$

where d is the average diameter of the particles and n is the numerical density of the particles, taken from the atmospheric model.
The flow is considered a "free molecular flow" when the Knudsen number K_n is greater than 1 [31]. An average and constant value for the molecular diameter has been selected from [32] which is of $d = 3.78 \times 10^{-10}\,\mathrm{m}$. Since this value is an important influencing factor for the Knudsen number, a sensitivity analysis between a value of $d = 3.78 \times 10^{-10}\,\mathrm{m} \pm 10\%$ has been done. Since a small S/C has been considered, mean lengths of 0.3 m, 1 m and 2 m and 3 m have been analyzed. The results are in the diagrams of Fig. 4.11.

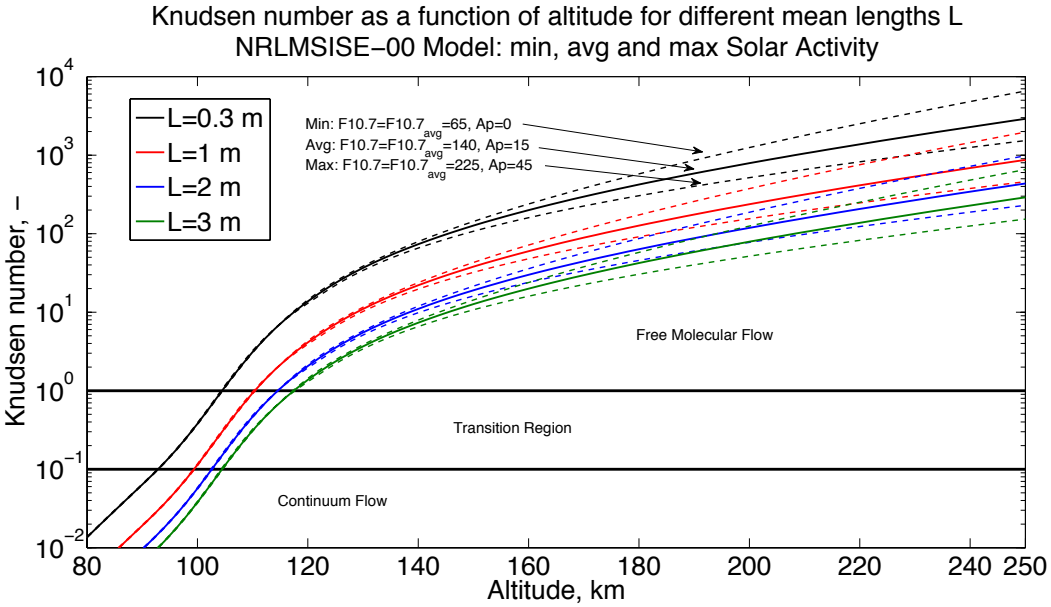

Figure 4.11: Knudsen number vs Altitude for different mean lengths.

In Fig. 4.12 the region of the change from free molecular flow to transition flow is shown.
The change in flow is always below the considered bottom altitude limit of 120 km, see Tab. 4.3, and the influence of the solar activity on the Knudsen number is very small, less than 500 m of altitude uncertainty in the worst case, as can be seen in Fig. 4.12. For a values of L the Knudsen number should be calculated to

Table 4.3: $Kn = 1$, transition altitude for different mean lengths.

Mean Length L m	Altitude h km
0.3	104
1.0	110
2.0	114
3.0	118

determine if a transitional flow should be considered for the mission design or if the mission orbit should be raised.

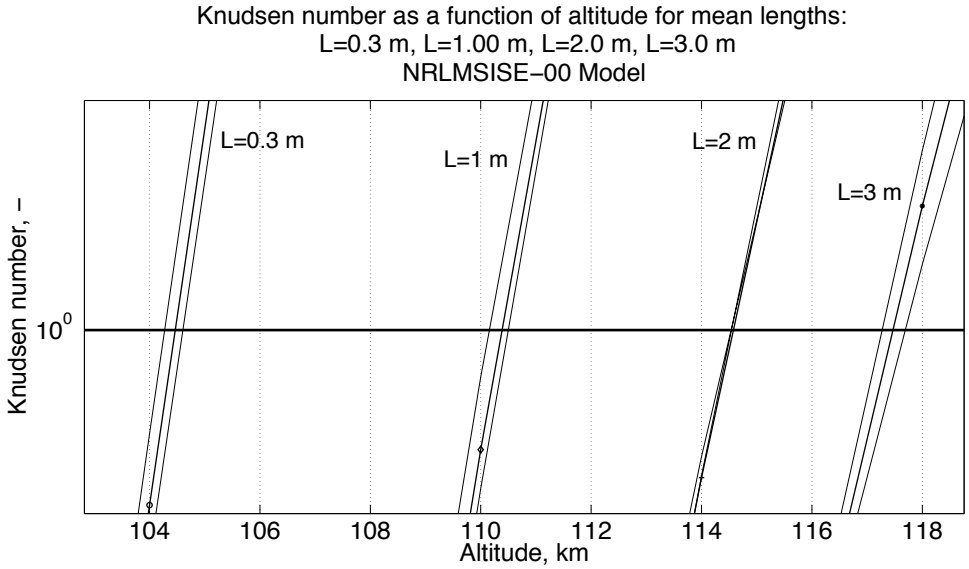

Figure 4.12: Detail Knudsen number vs Altitude for different mean lengths and solar activity.

4.5.2 Continuum

If the flow in which the S/C orbits is considered continuum, the formula for calculating the drag force is given by Eq. 4.10, following [33]:

$$\vec{F_D} = -m\vec{a_{drag}} = \frac{1}{2}\rho C_D A {v_{rel}}^2 \frac{\vec{v_{rel}}}{|\vec{v_{rel}}|} \tag{4.10}$$

F_D is the drag force, ρ is the density of the encountered flow, A is the projection of the surface impacted by the particles perpendicular to the incoming flow, v_{rel} is the velocity of the incoming flow relative to the S/C and C_D is the drag coefficient.
The drag uncertainty is here mainly driven by the product of ρ and C_D: a correct value of the drag coefficient C_D is fundamental for determining the drag force acting on the S/C.

Drag coefficient

A simple approximation of the drag coefficient in continuum is given by:

$$C_D = \frac{2m\vec{a_{drag}}|\vec{v_{rel}}|}{\rho {\vec{v_{rel}}}^2 A \vec{v_{rel}}} \tag{4.11}$$

Together with a good choice of the appropriate atmospheric density model, this can provide a good approximation for drag modeling for the S/C during its lifetime. However the drag coefficient is dependent on many factors such as gas-surface interactions of specular or diffuse reflection of the particles on the S/C, surface characteristics, attitude, shape, temperature, and atmosphere molecular content, density, temperature.
Early in the space age [34] most orbit analysts used $C_D = 2.2$ for satellites of compact shapes, this value was an estimate made by Graham Cook [35], [36].
Pardini, Tobiska and Anselmo [25] estimated decay for six spherical different satellites in orbits lower than 500 km using MSISE-90 and JR-71 atmospheric models. The study states that a $C_D = 2.2 \pm 5\%$ remains practically unchanged, as can be also seen in the Fig. 4.13.
For satellites of compact shapes, from [37], the Atmospheric Explorer (AE) has

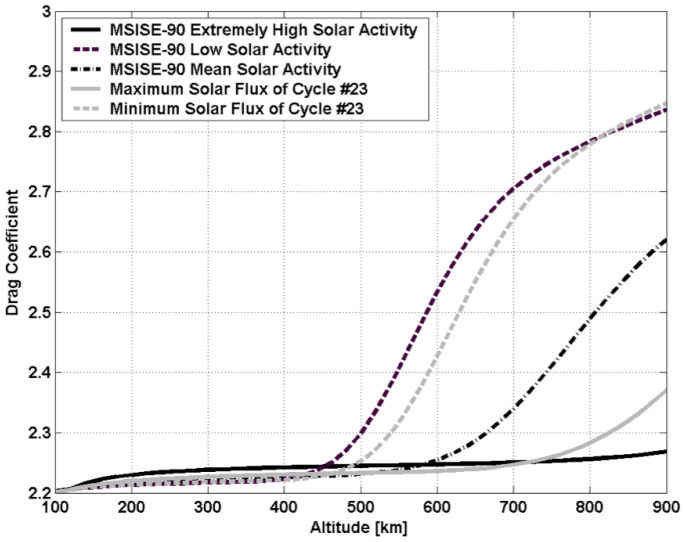

Figure 4.13: Physical drag coefficient for a spherical satellite as a function of altitude and solar activity, from [25, p. 12].

been taken as representative: it is a drum-like cylinder of 1.4 m diameter and 1 m length with a $C_D = 2.35$ at 200 km altitude.
For satellites of cylindrical shapes where length to diameter ratio is of 5 flying like an arrow, a $C_D = 3.3$ has been calculated, with the assumption that the angular distribution of molecules re-emitted form the long sides of the cylinder is diffuse. This means that there is a contribution on the drag coefficient C_D because of the momentum exchange of the molecules with the lateral surfaces of the S/C, this means that a longer S/C will have generally a greater C_D.
In the calculation of the drag, attention must be taken on the shading effect: the following charts take into account the effect of self-shading (e.g., shading on

the back side of a cylinder) but not the shading of one sub-shape by another. *"Shading is the part of a S/C that has been blocked from the incident flow due to another part of the S/C"* [38].
Two methods are used to determine the shading effect.
The "light-ray" method assume that the "light" is a parallel beam to the flow velocity of the incident molecules, thus, any sub-shape that falls into the shadow generated by another part is not subject to the impact with these molecules and yields no contribution to the drag or moment coefficients.
The second method considers the random motion of the molecules. The molecules penetrate into the "light-ray"-defined shadow, the amount of the penetration is approximated by the angle arctan $\left(\frac{1}{S}\right)$, see Fig. 4.14.
As $S \to \infty$, the shadowing tends to 0, if $S \to 1$ than the penetration angle approaches 45° which is the lower limit of validity for this method.

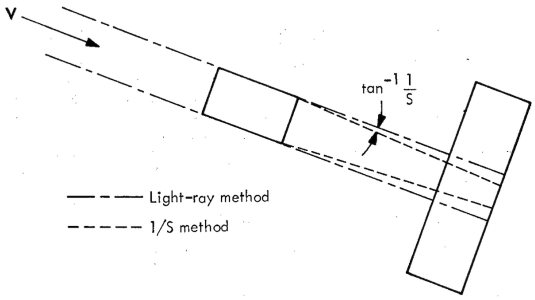

Figure 4.14: Light-ray and 1/S shadow lines [38].

Since the orbits considered in this study surely encounter a high level of drag force, an aerodynamically-efficient design should be taken into account to reduce the drag force, but also to minimise the aerodynamic torques acting on the S/C. During the orbit the drag force will vary depending on the attitude, even by a factor of 10 depending on the S/C's shape [33].
With a selected frontal reference area of 0.01 m^2 (Cubesat's size), in the Tab. 4.4 it is shown the effect of the attitude motion on the drag coefficient.
The attitude motion considered are shown in Fig. 4.15 and explained as following:

- Isotropic tumbling: worst case scenario, the S/C assumes each possible attitude with equal probabilities;
- Gravity gradient stabilization: the S/C flies with the long axis aligned to the local vertical direction;
- Passive magnetic field stabilization: the S/C is in fast rotation around the long axis which taxes 2 turns per orbit, remaining in the orbital plane.

- Velocity alignment: the S/C's long axis is aligned with the direction of the velocity.

Table 4.4: Drag coefficients of different attitude modes [39]

Attitude motion type	$\frac{A_{perp}}{A_{ref}}$	C_D
Isotropic tumbling	2.5	5.5
Gravity gradient stabilized	$\frac{8}{\pi}$	5.6
Magnetic field stabilized	$\frac{2}{\pi} + \frac{8}{\pi^2}$	5.0
Velocity aligned	1	2.2

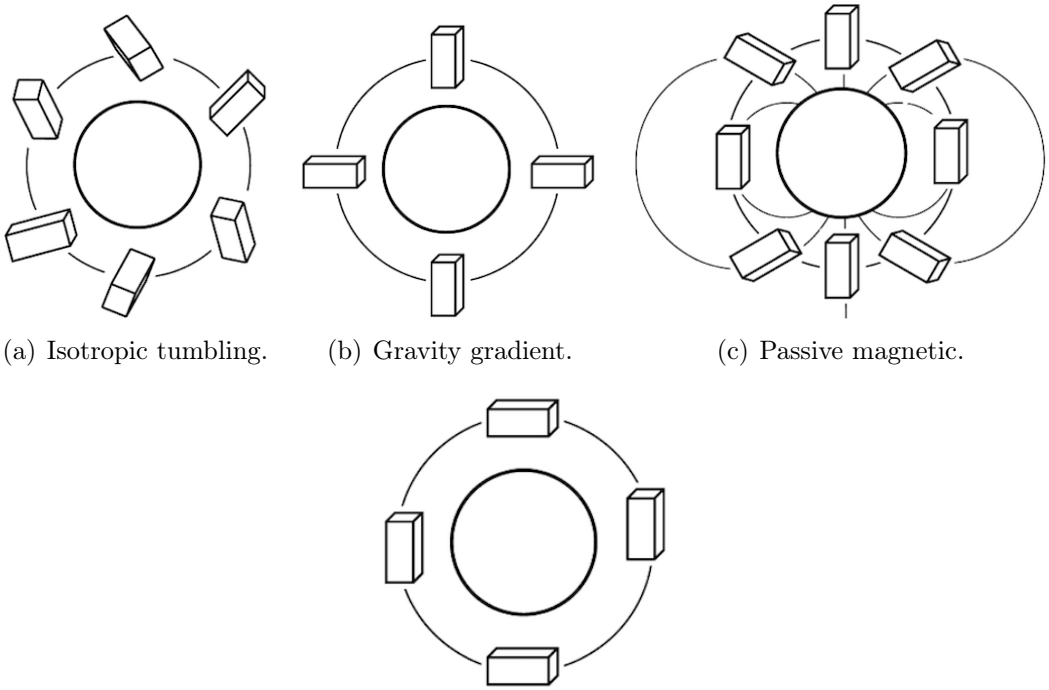

(a) Isotropic tumbling. (b) Gravity gradient. (c) Passive magnetic.

(d) Velocity aligned.

Figure 4.15: The investigated attitude motions [39].

According to [40] the drag coefficient can be defined in three distinct ways: (i) a physical drag coefficient, (ii) a fitted drag coefficient, and (iii) a fixed drag coefficient. Physical drag coefficients are determined by the energy and momentum exchange of the free stream atmospheric molecules with the spacecraft surface. Fitted drag coefficients are estimated as part of an orbit determination process

and fixed drag coefficients simply use a constant value of drag coefficient for every condition. Fitted drag coefficients are specific to the atmospheric model used and therefore they carry all the limitations of the used atmospheric model and consequently absorb other model errors.
Simulations with DMSC show that there is no linear correlation to the cross sectional area or to the square of the velocity, since density, Mach number and temperature cannot be strictly defined in such rarefied gas conditions [33].
According to [41, p. 84], particular attention should be kept to the fact that at lower altitudes λ, which is mean free path of the molecules, decreases and the flow might be defined as hypersonic continuum flow: in this regime the C_D coefficient reduces from 2.3 to about 1.0, since the re-emitted molecules partially shield the S/C from the incoming flow. From the same source, [41, p. 85], the precise determination of C_D in the project phase is generally not very good: the drag coefficient depends in a complex way of the combination of S/C surface materials, components of the atmosphere, molecular weight, and temperature of the impacting particles. A rough approximation is $C_D = 2$ in the case of a spherical body, typical values for non-spherical convex-shaped S/C have to be found in the range from 2.0 to 2.3.
In the Tab. 4.5 the investigated C_D for the different investigated cases are shown.

Table 4.5: C_D for the investigated studies.

Study	S/C	C_D
Vallado, Finkleman [33]	Compact shape	2.2
Pardini, Tobiska, Anselmo [25]	Compact shape	$2.2 \pm 5\%$
"	$D = 1.4\,\text{m}$, $L = 1\,\text{m}$	2.35
"	$L/D = 5$	3.30
Montenbruck, Gill [41]	Spherical shape	2
"	Non-spherical convex-shaped	$2.0 - 2.3$

Concluding this discussion, a drag coefficient of $C_D = 2.2$ is selected, in the case of a small S/C. In case of a long S/C, length-to-diameter ratio of 5, a drag coefficient of $C_D = 3.3$ will be selected. For further improvements DSMC simulation must be executed to achieve a better value of C_D suitable to the designed S/C.

4.5.3 Free Molecular Flow

Free molecular flow is the description of the flow when the mean free path of the molecules is larger than the size of the object flying in those conditions.

In this condition the particles are not enough near to be influenced by each other. The interaction between the molecules of the atmosphere and the S/C will be also different than in a continuum flow.
According to [34], it has been discovered that the surfaces of the S/C orbiting in those conditions are covered with adsorbed molecules and this affects the energy accommodation and angular distributions of the molecules which are re-emitted from the surfaces in the altitude range between $150 - 300\,\text{km}$.
Responsible of that is mostly the atomic oxygen, found in in low altitudes [37] which could adhere to the surface of the S/C or the surface might grow hot, and the material characteristics might change during S/C lifetime.
By analyzing data from orbiting pressure (density) gauges and mass spectrometers at altitudes between 150 and 300 km, it was found that S/C surfaces are coated with adsorbed atomic oxygen and its reaction products. The higher the altitude the lower the surface coverage. When an incoming molecule impacts on a clear surface, it is re-emitted with a near specular angle with a partial loss of kinetic energy. If the surface is heavily contaminated by adsorbed molecules, then the molecules are re-emitted in a diffuse distribution losing a large portion of their kinetic energy. This increases energy accommodation and makes the angular diffusion of the re-emitted molecules wider.
The accommodation coefficient is defined as following:

$$\alpha = \frac{E_i - E_r}{E_i - E_w} \tag{4.12}$$

where: E_i = energy of incident molecule; E_r = energy of re-emitted molecule; E_w = energy of the re-emitted molecule if it left the surface at the surface (wall) temperature.
The accommodation coefficient α shows how close the kinetic energy of the incoming molecule is fit to the thermal energy of the impacting surface. Gregory and Peters [42] found in a circular orbit of 225 km that 97% of the molecule distribution was diffuse and the rest specular.
The gas-surface interaction include different parameters in the analytical model which will be described in the following Sec. 4.5.4.

4.5.4 Drag Calculation

The calculation of the drag has been done with both continuum and free molecular flow model.
The analytical model for the drag in continuum is the one of Eq. 4.10. This uses the NRLMSISE-00 Model ($F10.7 = F10.7_{avg} = 140, Ap = 15$) for average solar activity. From the model the atmosphere density ρ is taken; the orbital velocity v and relative velocity v_{rel}, the latter calculated considering the Earth's atmosphere

rotating with the Earth itself. The drag coefficient, as a result presented before, has been set to $C_D = 2.2$. The result of this calculation is plotted in Fig. 4.16. The difference between the two is negligible, since in this case the difference is given by the velocity of the Earth which is of $v_{T_E} = \Omega_E R_E = 464.92\,\mathrm{m/s}$.

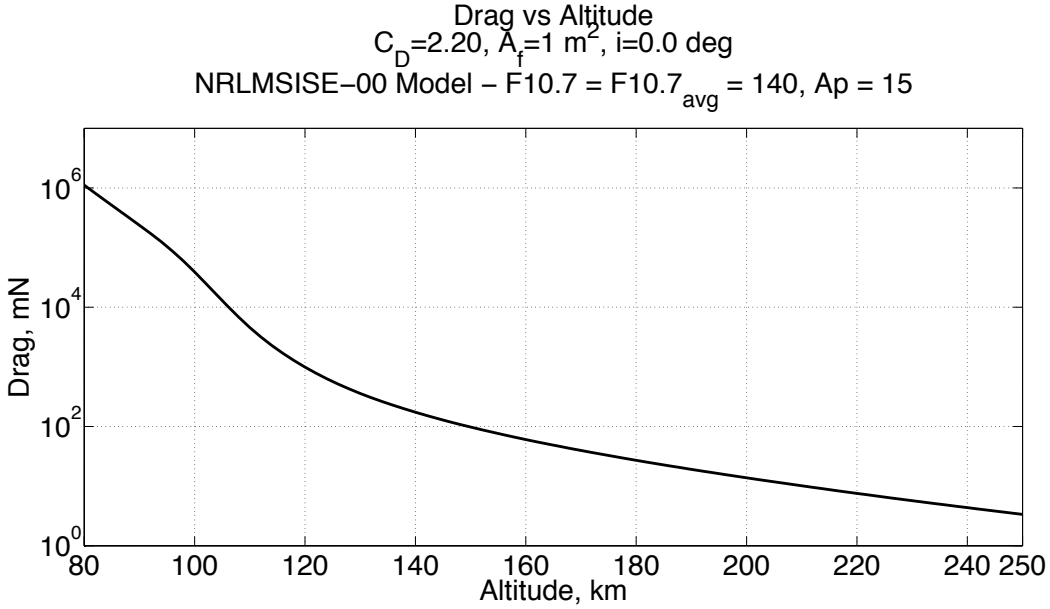

Figure 4.16: Drag in continuum flow vs Altitude.

For the calculation of the drag in free molecular flow, the analytical model used is the one provided by [43, pp. 104,105] and it is presented in Eq. 4.13, 4.14, and 4.15. The detailed Matlab script is described in Appendix B 8.4.

$$\vec{F}_D = A\left[-\hat{n}p + \left(\hat{n}\sin\zeta - \hat{v}_{rel}\right)\left(\frac{\tau}{\cos\zeta}\right)\right] \tag{4.13}$$

$$\begin{aligned}\frac{p}{q_\infty} =& \left\{\left[\frac{2-\sigma_n}{\sqrt{\pi}}\right]\sin\zeta + \frac{\sigma_n}{2s}\sqrt{\frac{T_s}{T_a}}\right\}\left\{\frac{1}{s}e^{-s^2\sin\zeta^2} + \sqrt{\pi}[1+\mathrm{erf}\,(s\sin\zeta)]\sin\zeta\right\}+ \\ &+ \left[\frac{2-\sigma_n}{2s^2}\right][1+\mathrm{erf}\,(s\sin\zeta)]\end{aligned} \tag{4.14}$$

$$\frac{\tau}{q_\infty} = \sigma_t\left\{\frac{1}{s\sqrt{\pi}}e^{-s^2\sin\zeta^2} + \mathrm{erf}\,(s\sin\zeta)]\sin\zeta\right\} \tag{4.15}$$

Where p is the total pressure, τ the shearing stress and q_∞ the dynamic pressure given by $q_\infty = \frac{1}{2}\rho_\infty v_{rel}^2$. $\hat{n}$ is the outward-pointing unit normal vector, σ_n and

σ_t are the normal and tangential accommodation coefficients, T_s is the absolute temperature of the surface, set to $T_s = 490\,\mathrm{K}$, as the average value in VLEO orbit calculated from the Matlab script presented in Sec. 4.3, and T_a is the atmospheric temperature, altitude dependent, taken from the model. An important component of the above equations is s the air speed, nondimensionalized by the mean molecular speed of the atmosphere as shown in Eq. 4.16:

$$s = \sqrt{\frac{M_a v_{rel}^2}{2R_{spec}T_a}} \tag{4.16}$$

M_a is the mean molar mass of the atmosphere which has been calculated from the atmospheric model through a Matlab script, as shown in Fig. 4.3, and R_{spec} is the universal gas constant. Here, all the parameters are altitude-dependent except for the universal gas constant.
In the calculation $\sigma_t = \sigma_n = 0.9$ are typical values, according to [43, p. 105], and the mentioned $\zeta = \hat{n}^T \hat{v_{rel}}$ is the pitch angle set to 0°, $\hat{n}$ and $\hat{v_{rel}}$ are the unit vectors of the normal vector and the relative velocity vector.
It is important to notice that calculation of the drag in free molecular flow does not depend from the drag coefficient C_D.
The Fig. 4.17 and Fig. 4.18 show the difference between the drag calculated in continuum and in free molecular flow. This shows that, in this particular range of altitudes, the drag calculated in free molecular flow is much lower than in continuum flow. In this case the S/C is considered to be a flat plate and to fly perpendicular to the direction of flight with a surface of $1\,\mathrm{m}^2$ and $0.3\,\mathrm{m}^2$ which is a simplified hypothesis.

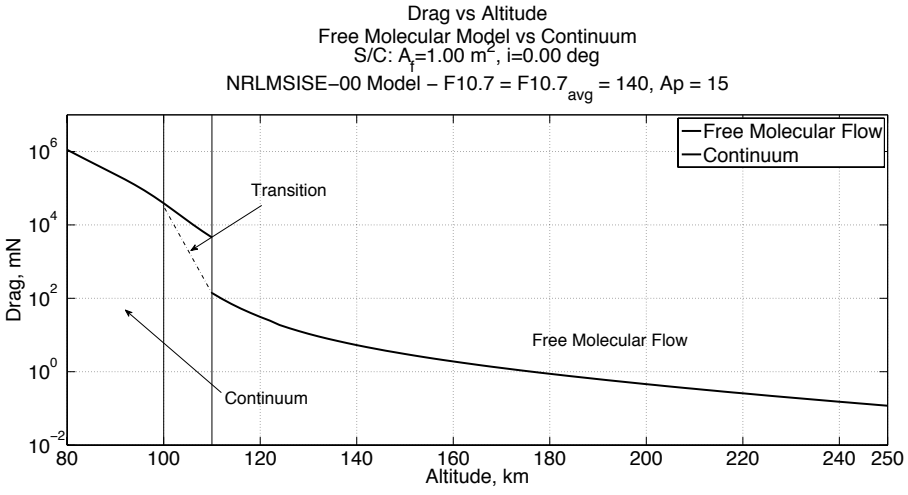

Figure 4.17: Drag vs Altitude, free flow and continuum, $A_f = 1\,\mathrm{m}^2$.

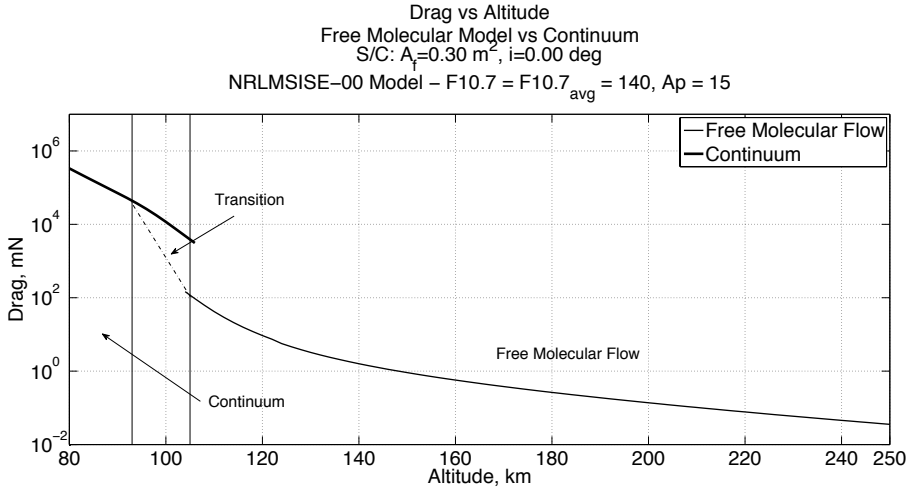

Figure 4.18: Drag vs Altitude, free flow and continuum, $A_f = 0.3\,\mathrm{m}^2$.

Other Parameters Affecting The Drag

When calculating the drag force, particular attention should be taken regarding the surfaces of the S/C encountering the flow.
As stated before the gas-surface interaction depends on the surface characteristics. The model previously used for the calculation took into account only the frontal surface of the S/C.
Solar arrays - SA - might provide the required electric power for the operation of the RAM-EP system and the other subsystems. They will represent probably the biggest surfaces of the S/C, this means they will affect the generated drag force. Considering the S/C flying on a Sun-Synchronous Dawn-Dusk orbit we shall consider keeping an aerodynamic-efficient S/C's shape configuration in order to reduce the area encountering the flow perpendicularly, for example assuming the S/A to be parallel to the direction of flight. As stated in Sec. 4.5.2 the surface which is parallel to the flow will also affect the generated drag since the particles in random motion will impact the surfaces that are parallel to the flow and will be reflected with a certain angle depending on the accommodation coefficient defined in Eq. 4.12, this means in an exchange of energy thus momentum.

DSMC simulations are therefore needed to estimate the effect of large surfaces, like S/A, as well as of other S/C's components in contact with the flow, first of all the Air Intake, to derive their effect on the generated drag force.

4.6 Power Supply

The power required for the RAM-EP system can be provided by several electric production and storage devices in different combinations.

The most common power supply for S/Cs orbiting planets near to the Sun, like Earth and Mars, might use the combination of S/A which converts the power of the Sun directly to electricity, and batteries which are recharged by the S/A and release electricity when the power required by the S/C's subsystems is more than the power generated by the S/A, or when the Sun is eclipsed by the planet around which the S/C is orbiting. A precise ACS will be required in order to keep the surfaces of the S/A nearly perpendicular to the Sun vector in order to maximize the efficiency and, depending on the power requirements and the S/A and batteries capabilities, only certain orbits might be suitable in order to fulfill the S/C's energy requirements.
One physical quantity which becomes important when reaching the lower altitudes in VLEO, as shown in Sec. 4.3, is heat. Heat might be converted directly into electricity by the use of a thermionic generator which works on the principle of the Seeback effect, which describes the phenomena of voltage generation in a conductor or semiconductor when subjected to a temperature gradient. Thermionic generators are not yet a mature technology for an application in space under these conditions, but a recent study, see [44], calculated that an efficiency of $\eta = 42\%$ might be achievable.
The use of this kind of generator might allow to reduce the requirement of the surface of the S/A, in a way to decrease the mechanical complexity and the surfaces generating drag, indeed a thermionic generator has no moving parts.
It has to be kept in mind that only 42% of the heat is converted in electrical energy and the other 56% of heat must be taken away from the S/C through the thermal subsystem.

Solar Arrays

Emcore ZTJ photovoltaic cells for space application, [45], with a minimum average efficiency in begin of life - BOL - of 29.5% have been selected. The Sun is assumed to be always perpendicular to the solar cell as in Sun-Synchronous orbit. The mission lifetime has been set to 7 years as in the ESA study [12].
A range of powers, according to the literature review, has been set and the required solar array surface has been calculated.
Degradation has been calculated according to the script in Appendix B 8.5 and produced the results of Tab. 4.6.

Furthermore a calculation of the cell number connected in series to produce

Table 4.6: Power vs. SA Area - EOL

P_{max} kW	A_{SA} m^2
0.5	1.98
1	3.96
1.5	5.93
3	11.87
3.5	13.84
5	19.6

certain voltages has been made, as well as the area required for the string.
Voltage values has been chosen by running the IPG6 facility as 1 kW of power produced by the anode was reached at 20 mg/s of air mass flow. Afterwards two more voltages has been sl according to [1] in order to being able to operate the facility without automatic shut-down due to power supply overload.
These has been calculated in EOL with the same parameters used for the SA area, the results are shown in Tab. 4.7.

Table 4.7: Voltage vs. Solar String Area - EOL

Voltage V	Number of Cells -	A_{string} m^2
550	319	0.85
850	493	1.30
1000	579	1.54

Concerning the geometry configuration, a good aerodynamic design should be chosen. That means in reducing at minimum the frontal area of the whole S/C by disposing the solar panels with the long side parallel to the direction of flight. Reduced frontal area will minimize the drag produced, however drag calculation due to side interaction should be made.
The thickness of the solar array for small spacecraft is 15 mm according to [46], this means that the increasing of the front surface can been neglected if the S/A are in parallel to flight direction.

Thermionic Generator

As stated before the use of thermionic generator to convert the heat in the lowest atmosphere levels might be in future a solution to reduce the solar array's surface. The technology is not yet mature and with a maximum theoretical efficiency of $\eta = 42\%$ [44], there is still a big amount of heat to be taken away through the thermal subsystem.
A thermionic generator is basically made up of a "hot" electrode and a "cold" electrode, the hot electrode is made of a material which can withstand high temperatures and, under these conditions, vaporize very slowly releasing electrons which then condensate on the "cold" electrode, the electrons flowing generate a voltage and thus a current which generates power.
Using the values of heat flux depending on altitude with an $A_f = 1\,\mathrm{m}^2$, a very rough calculation of the electrical power which might be obtained from heat through a thermionic generator is made as follows:

$$P = Q_{tot} A_f \eta \tag{4.17}$$

Which yields to the results shown in the table 4.8: the values are shown only for the altitude range of interest since the power heat flux which has more impact is generated by the particles impacting the front surface and an increment can be seen from altitudes below 120 km, as shown in Fig. 4.7.

Table 4.8: Power obtainable from a thermionic generator of efficiency $\eta = 42\%$ as a function of altitude for a surface of $A_f = 1\,\mathrm{m}^2$.

h km	P kW
120	2.85
130	1.99
140	1.73
150	1.62
160	1.57
180	1.52
200	1.45

4.7 Thrust Profile

A thrust profile for the mission must be chosen. This means to select the level of thrust needed in relation to the drag generated and the time, during the orbit, in which the propulsion system should be operational. The thrust generated can compensate completely or partially the drag, with a given T/D ratio. The thrust profile can be continuous or pulsed and this will influence directly the electrical power needed. If a pulsed thrust profile will be chosen, an investigation over the performance of a pulse propulsion thrust profile should be done.
As discussed in Sec 3.4, the IPG6-S has been chosen as a possible thruster for a RAM-EP application. The thrust of the S/C will be evaluated as a function of altitude and mass flow.
Since a design of a RAM Electric inductively heated thruster is not yet ready, the following diagrams have to be read as a first attempt to determine the best and the worse case scenarios using the IPG6-S as a possible thruster.
The total enthalpy of the IPG6-S, following the characterization of [1], has been extrapolated through a device designed to obtain the plasma power exiting the IPG6 [47], in order to derive the exhaust velocity for thrust calculation.
The first simplifying assumption, is that all the thermal energy of the plasma is converted to kinetic energy.
In the test from [1], the input mass flow rate was of $\dot{m} = 60\,\mathrm{mg/s}$ which is a high value compared to what is encountered by the S/C on orbit in RAM-EP range, as shown in Fig. 4.9.
The plasma generated under these conditions showed a total enthalpy measured of $h_{tot} = 7.5\,\mathrm{MJ/kg}$ [1].
The exhaust velocity has been calculated as in Eq. 4.18.

$$c_e = \sqrt{2h_{tot}} \tag{4.18}$$

This yields a results of $c_e = 3872.98\,\mathrm{m/s}$.
As a first step to calculate the thrust, the value of exhaust velocity has been assumed to remain constant with the altitude. The thrust has been calculated as a function of altitude and it is plotted in the following diagrams.
The thrust calculation is calculated as shown in Eq. 4.19.

$$T(h) = \dot{m}(h)c_e = \rho(h)v_{rel}(h)A_f\eta_c c_e \tag{4.19}$$

η_c is the collection efficiency, the values derived from the State-of-the-art are: 35% realistic case, 90% and 100% as ideal case.
A_f is the frontal area, the values of 0.3 and of $1\,\mathrm{m}^2$ has been taken.
v_{rel} is the relative velocity and ρ the air density taken from the NRLMSISE-00 atmospheric model in average solar and geomagnetic activities.

The result of the drag and thrust calculation on the base of these assumptions is plotted in the next diagrams.
The first plot, in Fig. 4.19, represents the T/D ratio considering the flow to be continuum for a frontal area of 0.3 and 1 m^2 for the three η_c considered.
In case of continuum the, for both A_f, as both equations depends directly on A_f, the best case, of $\eta_c = 1$ shows that a T/D ratio of 0.48 can be achieved, for $\eta_c = 0.9$ of ~ 0.42 and in the worst case, $\eta_c = 0.35$, 0.17 of T/D ratio can be achieved. However it has been calculated that the S/C will orbit into a

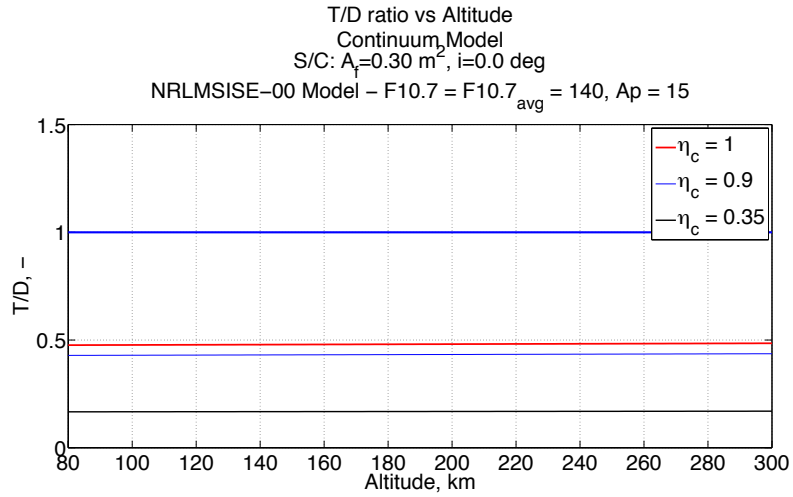

Figure 4.19: Thrust to Drag ratio vs altitude in continuum, $A_f = 1\,m^2$. $A_f = 0.3\,m^2$ shows the same values.

free molecular flow, therefore a plots for T/D ratio depending on altitude in free molecular is shown in Fig. 4.20 and Fig. 4.21.
The same consideration about the two different frontal area in continuum is still valid.
It shows that the thrust generated is up to 16 times the drag for a $\eta_c = 1$, 14 times for $\eta_c = 0.9$ and 6 times for $\eta_c = 0.35$ and in the worst case, for altitudes above 250 km respectively 13, 12 and 4 times the drag.
Therefore full thrust compensation is possible over all the RAM-EP range for every η_c considered.
The step visible in the plot is between an altitude of 120 and 122 km and it is due to a divergent trend of thrust and drag with altitude. However it is in an hypothesis that the exhaust velocity remains constant with the altitude.

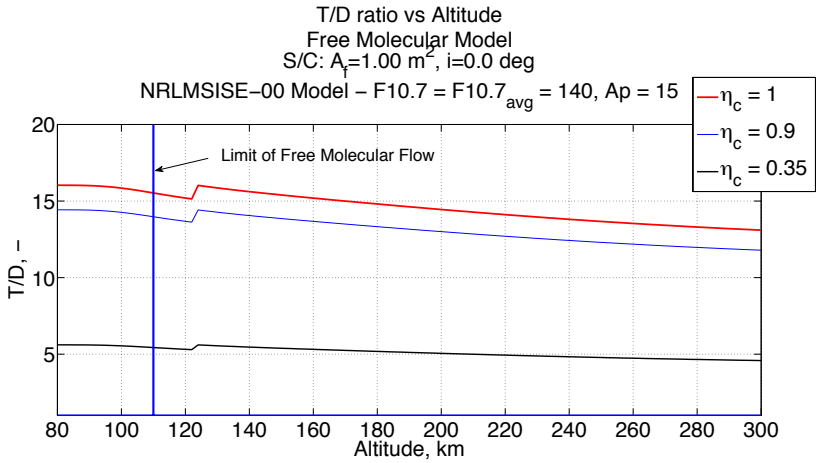

Figure 4.20: Thrust to Drag ratio vs altitude in FMF, $A_f = 1\,\mathrm{m}^2$.

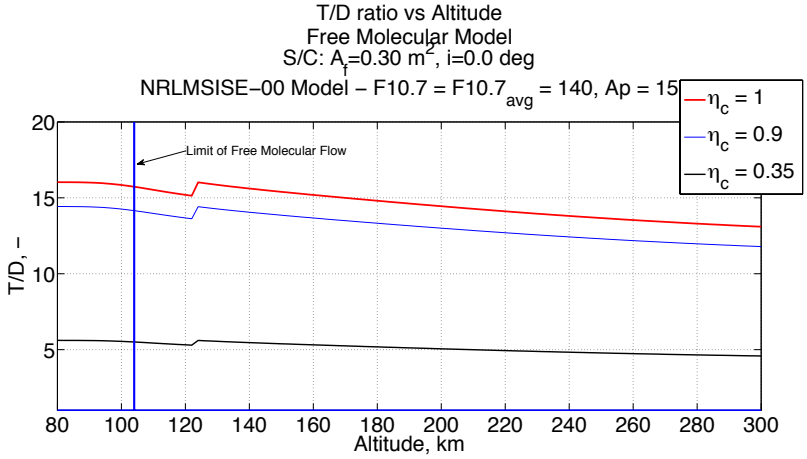

Figure 4.21: Thrust to Drag ratio vs altitude in FMF, $A_f = 0.3\,\mathrm{m}^2$.

A chart is shown in Tab. 4.9 shows the results of this first thrust calculation attempt.

Table 4.9: Drag compensation capability for IPG6-S, $c_e = 3872.98\,\mathrm{m/s}$.

η_c -	T/D Continuum	T/D FMF
1	~ 0.48	$\sim 16 - 13$
0.9	~ 0.42	$\sim 14 - 12$
0.35	~ 0.17	$\sim 6 - 4$

Chapter 5

Inductively Plasma Generation

In this chapter a brief review of the research on Inductively Coupled Plasma Generators, IPGs, will be described. Afterwards the definition of plasma will be given as well as the principle of operation of Inductive Plasma Generators. Afterwards the IPG6-S facility will be described.

5.1 Plasma

Plasma is commonly known to be the fourth state of matter, 99% of the Universe is in the plasma state: stars, gaseous nebulae, interplanetary medium, intergalactic medium and comet tails.
On Earth it is found naturally: lightnings, St. Elmo's fire, Aurora Borealis and Australis, and it is created artificially: neon signs, low-consumption fluorescent lights, plasma displays of wide flat televisions.
Plasma has different applications: illumination, precise cutting of materials (plasma torch), water treatment and research for future fusion reactors. In space applications it is generated on the surfaces of the S/Cs during reentry, Fig. 5.1, as well as in the rocket exhaust and in ion thrusters.

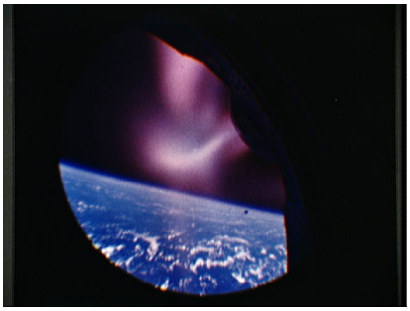

Figure 5.1: Reentry plasma from inside of Gemini 2, 19 January 1965 [48].

According to [49, p. 3], the definition of plasma is:

> *A plasma is a quasi-neutral gas of charged and neutral particles which exhibits a collective behaviour.*

"Collective behaviour" means that as the charged particles move around into the plasma, they can generate local concentrations of negative or positive charge which varies the electric fields. When the charged particles move, they generate currents and consequently magnetic fields. The moving charged particles of the plasma will effect, exerting a force, other charged particles also on large distances. Motions do not depend only on local conditions, but also on what happens at the remote regions of the plasma.
Quoting again [49, p. 4]:

> *Because of collective behaviour, a plasma does not tend to conform to external influences; rather, it often behaves as if it had a mind of its own.*

"Quasi-neutral" means that globally the plasma will keep its quasi-neutrality condition, given by $n_i \simeq n_e \simeq n$ namely that the numerical density of the ions n_i equals the one of the electrons n_e. If electric potentials are applied to the plasma, the plasma itself will shield out those fields to maintain its quasi-neutrality condition.

5.2 Inductively Coupled Plasma Generation

An Inductively Coupled Plasma Generator, IPG, is basically composed by a casing in which a quartz tube, the discharge channel, is inserted. The gas to be ionized, the medium, is injected inside the discharge channel. This is surrounded by a coil which is traversed by a current fed by an external RF source.
The RF source feeds the coil with an RF high electric alternate current inducing an oscillating magnetic field into the discharge channel. The generator works as a transformer where the first winding is the coil and the secondary is the plasma inside the discharge channel. The oscillating magnetic field generated by the coil in the discharge channel forces an azimuthal electric field that accelerates the charged particles in the gas toward a direction opposite to the electric current in the coil, Fig.5.2.
Free electrons impact the other particles ionizing them in a way that more free electrons are generated consequently ionizing more particles. The result of this process is a chain reaction that ignites and sustains the plasma increasing its electrical conductivity as the temperature increases.
Since the plasma has a dampening effect on the magnetic field, known as Skin

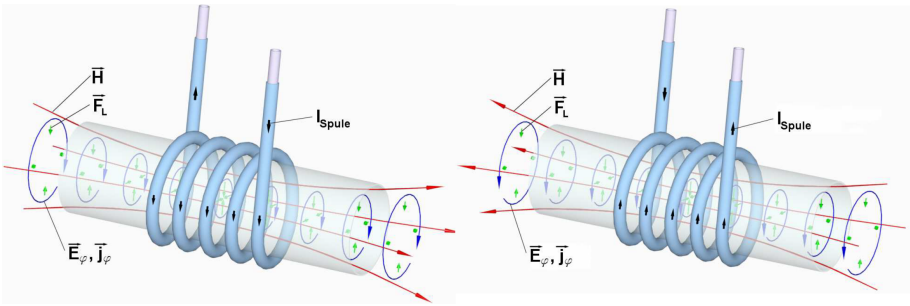

Figure 5.2: Electrodynamic relations in an IPG [50].

effect, the plasma is primarily heated in a ring-shaped zone, this means that there will be less power coupling in the center of the discharge channel than in the border region. The dampening of the magnetic fields increases with the operating frequency.
The generated plasma is afterwards ejected from the through the discharge channel by the same magnetic field created for plasma generation, that means Lorentz forces as well as thermal expansion.

5.3 Research on IPG

The first inductively coupled plasma generators - also called RF-plasmatrons - were developed at the Russian Institute for Problems in Mechanics in Moscow, Russia, from 1963.
IPGs were used for solving issues related to aerodynamic heating of hypersonic vehicles. In particular for investigating the physics of plasma/material interactions and to test different elements for thermal protection systems for re-entry vehicles. In France there are now two institutions researching on IPGs: the Complexe de Recherche Interprofessionnel en Aerothermochimie (CORIA) in Rouen, and the Laboratoire Arc Électrique et Plasmas Thermiques (LAEPT) in Clermont-Ferrand. The Von Karman Institute (VKI) in Rhode-Saint-Gense, Belgium operates the Plasmatron, a powerful plasma generator which reaches 1.2 MW of power.
Experience has been gained in IPGs during the years at the Institute of Space Systems, IRS, at Universität Stuttgart by the construction and operation of IPG3, 4, 5, and 7 [50]. The power supply is of 375 kW and they are used for re-entry test for materials and for propulsion systems.
For this thesis, the IPG6-S has been operated to obtain data for a RAM-EP system feasibility phase 0/A study.
IPG6-S is a small size IPG operating at low powers available at the laborato-

ries of the IRS at Universität Stuttgart, Germany. A twin model of the IPG6 is available at the Center for Astrophysics, Space Physics and Engineering Research (CASPER) at Baylor University, Texas, USA. Its denomination is IPG6-B and it is a collaboration with IRS: the main difference is the power supply.
For IPG6-B a maximum of 15 kW are provided at a frequency of 13.56 MHz due U.S. frequency regulations.
IPG6-S power supply delivers a maximum of 20 kW at a frequency between 3.5 and 4.5 MHz.

5.4 IPG6-S Facility

The facility of the IPG6-S in Stuttgart, shown in Fig. 5.3, is described in this section.
The generator is the main component, it is fed by the gas feed subsystem and it is connected to the vacuum subsystem, necessary to keep the low pressure conditions for simulating space environment. The power supply provides the required current, voltage and frequency to ignite the plasma. The cooling subsystem provides water cooling for the generator, the calorimeter, the power supply, and the vacuum subsystem. The data & diagnostic subsystem provides the visualisation and storage of the different parameters of the facility. It serves to control, keep the operational safety margins, and to characterize the performance of the facility.

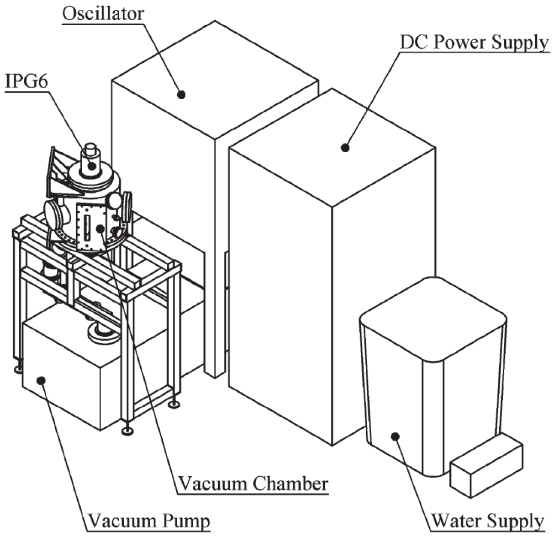

Figure 5.3: The IPG6-S facility [23].

5.4.1 Generator

The IPG6-S, Fig. 5.4, is a small size inductively plasma generator with a discharge channel made of quartz glass which measures 40 mm in diameter and 180 mm in length. The external dimensions of the generator are of circa 200 mm of length and a diameter of the case of 160 mm. The generator has been designed by Dropmann [51] and improved by Puckert [47] and Massutí [1]; the materials used for the generator components must have low permeability according to Herdrich [50], since the oscillating magnetic field of the generator produces azimuthal electric fields, thus Eddy currents, in all the components which have high permeability and are near enough to the generator itself, causing them to heat up and changing the magnetic field inside the discharge channel.
The generator is mounted on the top of the vacuum chamber, at the bottom of the generator there is a flange which connects it to the vacuum chamber and provides water cooling, on the top of the generator is the injector head, that delivers the gas into the discharge channel.
The components of the generator will now be introduced.

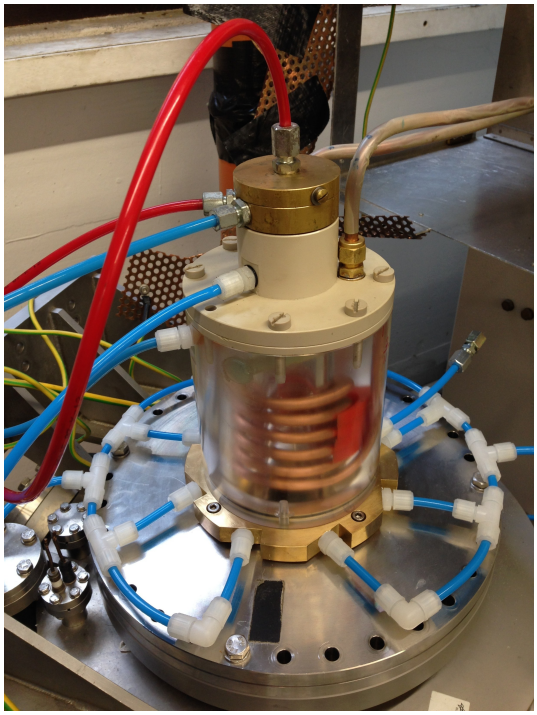

Figure 5.4: IPG6-S Generator mounted on the Vacuum Chamber

Casing

The main casing is a cylinder made of acrylic glass.
It is the main structural component, almost all the parts of the generator are attached to it: at the same time the casing provides limited optical access to the plasma. It has an aperture in the middle where the coil together with the quartz tube - the discharge channel - are inserted. During this work, the casing has been modified to adapt it to the new designed water-cooled bottom flange.
In the precedent design, water inlet and outlet were positioned in the casing: the water was injected through a pipe at the bottom, flowed around the discharge channel and the coil, and exited at the top of the casing for being directed to the injector head.
With the new design, the inlet at the bottom of the casing has been closed since the cooling is now provided by the bottom flange; the outlet was not changed and it operates as before.

Discharge Channel

The discharge channel is made up of a quartz glass tube. The choice of quartz glass as the material for the tube has been made since the inner wall of the tube is in direct contact with the plasma: this means it must withstand the high temperature gradients which are generated as well as it has to be chemically resistant to the attack of aggressive gases such as atomic oxygen which can be injected as working gas. The diameter of 40 mm has been chosen according to Herdrich [50] and to Dropmann [51] as to be both suitable for a frequency of 4 MHz and for the common available size in commerce. The length of the tube is given by the size of the generator, and this has been set to 180 mm. From a study conducted by Puckert [47] the wall thickness of 1.5 mm has been found as the minimum to allow maximum cooling for 4 kW of power before breaking due to thermal stresses.

Coil

The coil used for the IPG6-S is of 5.5 turns and serves to create the high frequency magnetic field that ignites the plasma, the external diameter of the copper pipe is of 8 mm.
The electric power is coupled into the plasma next to the coil where the magnetic field is more intense.
The coil is traversed by water in the inside, to provide the necessary cooling during operation; it is shown in Fig. 5.5 and its electromagnetic and geometric values are shown in Tab. 5.1.

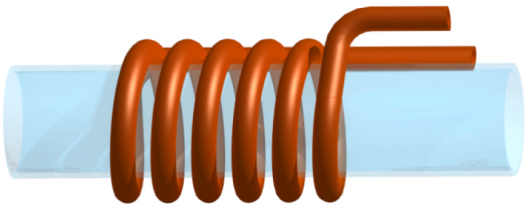

Figure 5.5: The 5.5 turns coil.

Table 5.1: Electromagnetic and Geometric values of IPG6-S Coil [1].

Turns -	Length mm	Internal Diameter mm	Inductance µH
5.5	80	40	0.489

Water-Cooled Bottom Flange

Part of the work of this thesis has been the design of a new water-cooled bottom flange to extend the duration of the experiments which, with the previous design, was limited in time because of high thermal gradients on the bottom flange which caused it to broke [1].
The flange is provided with 8 inlets with G 1/8" threads in which the water enters radially at the bottom of the generator and impacts tangentially the quartz tube wall. Subsequently the water raise upwards surrounding the quartz tube, the coil and the casing providing the necessary cooling. The new designed water-cooled bottom flange is composed by the the flange itself, a removable closure, and an adapter for the connection to the vacuum chamber. The flange has the 8 radial ducts for the water cooling, 4 holes for the connection of the generator to the vacuum chamber, 4 holes for the connection to the casing and 6 threads for the connection of the closure. The closure has been provided to enable access to the O-ring which creates the sealing between the flange, the quartz tube, and the vacuum side, creating the clearance for the sealing. Details of the water-cooled bottom flange are shown in Fig. 5.6 and later in Fig. 5.13(b). The technical drawings are in Appendix C. The design of a new bottom flange included also a modification of the casing. Its lower part has been removed and adapted for the connection of the the new bottom flange.
These modifications required also the design of an adapter between the bottom flange and the vacuum chamber. This has been realized with a 3 mm thick brass ring with a clearance for the O-ring which provides face sealing between the bottom flange and the ring itself. The vacuum chamber is provided with another O-ring which creates the face sealing between the vacuum chamber and the lower

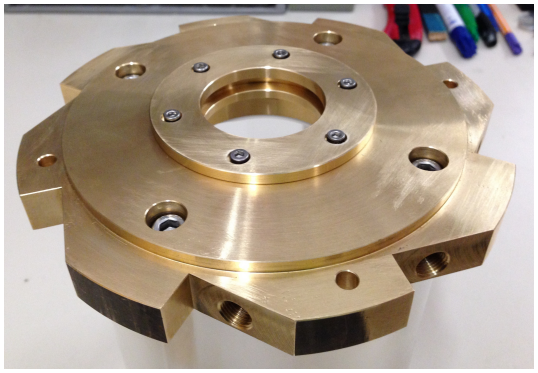

Figure 5.6: New water-cooled bottom flange.

surface of the brass ring adapter. The assembly is represented in Fig. 5.7.

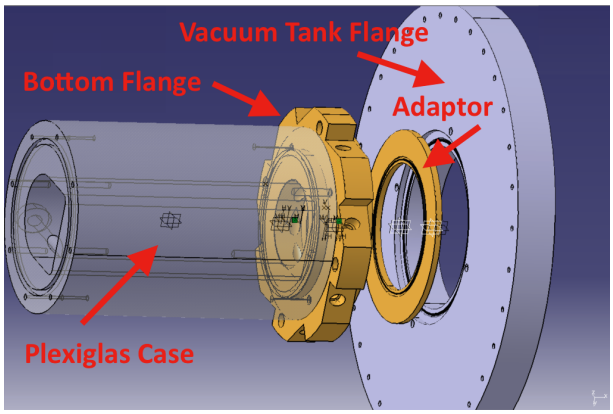

Figure 5.7: Assembly of bottom flange, adapter, and vacuum chamber.

5.4.2 Power Supply

The energy supply is provided by the RF generator HGL 20-4B produced by the Himmelwerk company which provides a maximum power $P_{max} = 20\,\text{kW}$ with a variable frequency between $f = 3.5 - 4.5\,\text{MHz}$, which depends on the impedance of the IPG [52]. It is composed by an energy supply unit together with an oscillator resonant circuit that uses the coil of the plasma generator as an inductance [1]. The capacitor is located in the box which contains the oscillator circuit and has a capacity $C = 1500\,\text{pF}$.
The energy supply unit uses a three-phase connection with a current of $3 \times 50\,\text{A}$ and a voltage of $3 \times 400\,\text{V}$ for a total input of $P = 34\,\text{kW}$: it converts the three-phase current to an high DV voltage up to $V = 8.5\,\text{kV}$, which is called the anode

voltage of the tetrode. This is the voltage used to feed the oscillator resonant circuit. An additional voltage of $V = 8.5\,\mathrm{kV}$ is produced for the screen grid of the tetrode, which is used to control the anode current.
The maximum voltage in the oscillator circuit is of 1.7 kV. The coil of the generator provides the required inductance for the oscillating circuit.

Power Supply Monitors

The control panel of the power supply is provided by three main analog indicators, which show the anode current, the screen voltage for the oscillator and the power consumption in the anode. The last parameter is important because it is useful to determine the generator efficiency for different plasma conditions. The anode current shows how much current is fed into the oscillator circuit. The resolution of these indicators is of 0.5 A, the screen voltage is of 25 V and the power of 250 W.

5.4.3 Vacuum Subsystem

The vacuum system is composed by mainly two components, the vacuum pump and the vacuum tank.
The vacuum tank has a diameter and a length of about 40 cm with multiple flanges which can be used for the vacuum pump connections, plasma diagnostics and optical windows.
The vacuum tank is shown in Fig. 5.8. The vacuum pump used for operation is

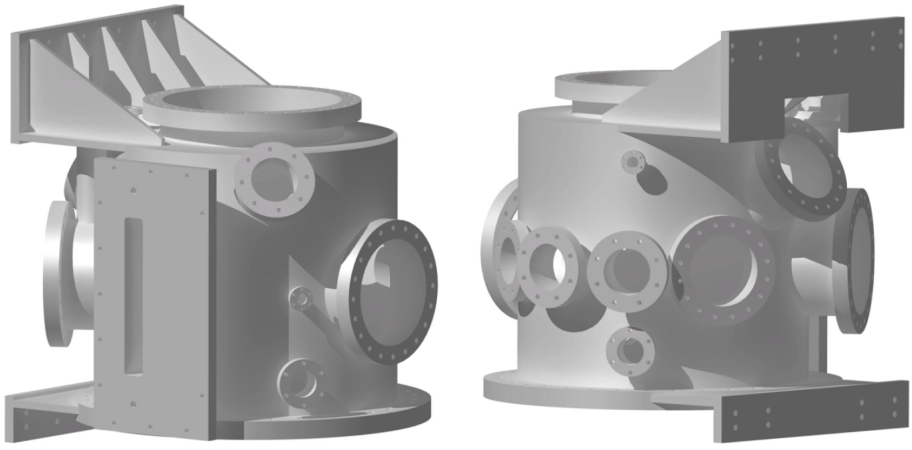

Figure 5.8: 3D model view of the vacuum tank.

a VAROVAC S 400 F, the main technical data given from the producer Leybold-Heraeus Gmbh are shown in Tab. 5.2. The vacuum pump requires water cooling

with a consumption and minimum pressure as shown in Tab. 5.2. In the Fig. 5.9

Table 5.2: VAROVAC S400F Vacuum pump specifications

Description	Value
Main Voltage	380/660 V
Motor power	11 kW
Rated rotational speed	1000 rpm
Nominal pumping speed	430 m^3/h
Average pumping speed	400 m^3/h
Approx. water consumption	200 L/h
Minimum water pressure	2 bar

the pressure of the tank in relation to the mass flow injected into the chamber through the generator according to [1] is shown.

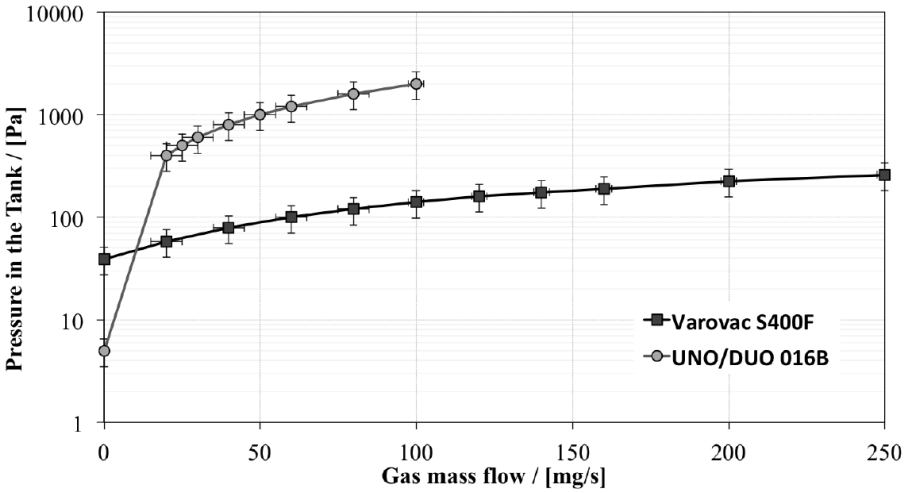

Figure 5.9: Pressure in the vacuum tank vs mass flow [1].

The pump was not operating for a long period of time, but after the first couple running tests the pressure achieved into the chamber without and with mass flow was according to the values presented in the thesis of Massuti [1], and the values shown in Fig. 5.9.

Improvement of Vacuum

In order to achieve more suction rate and lower pressure, hence better simulation conditions, a new pump has been introduced.

The new installed pump is a two-stage vane pump ALCATEL 2063, the main technical data from the producer are shown in Tab. 5.3.

Table 5.3: Alcatel 2063 Vacuum pump specifications

Description	Value
Main Voltage	200 V
Motor power	2.2 kW
Rated rotational speed	1500 rpm
Nominal pumping speed	65 m^3/h
Base pressure	2×10^{-2} Pa

Due to the power supply electrical connections, plasma can be ignited only if the VAROVAC vacuum pump is operating, for this reason the two pumps have been always operated together during plasma tests.
The pressure of the tank reached, with no mass flow, a pressure of $p_{tank} = 26$ Pa. With the old configuration, the pressure of the tank when injecting 60 mg/s was of $p_{tank} = 100 - 110$ Pa, with the new design lower pressures are achieved $p_{tank} = 86 - 88$ Pa.
In particular in Fig. 5.10 the pressures achieved in the tank for different mass flows are shown.

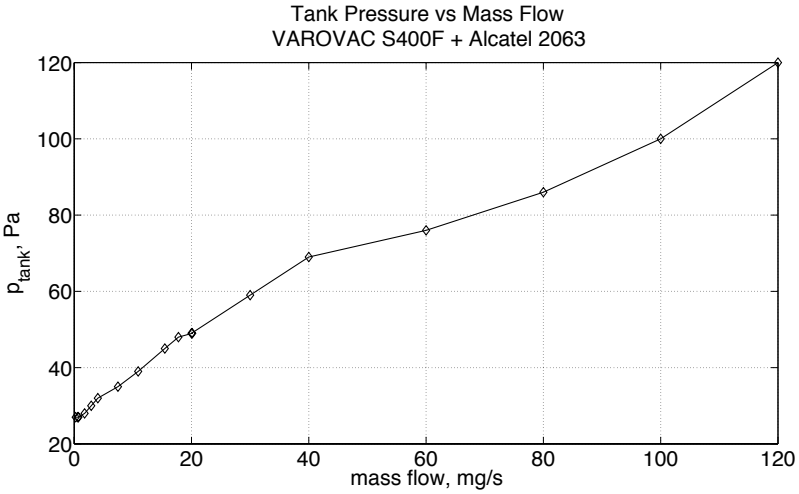

Figure 5.10: Pressure in the vacuum tank for different mass flows.

Pressure sensors

Two pressure gauges are connected to the facility to measure two pressures: the pressure in the injector head and the pressure of the tank.
The pressure gauges are PKR 251 from PFEIFFER-Vacuum manufacterer and operate in the range between 5×10^{-7} Pa and 100 kPa with an accuracy of ±30% in the range between 5×10^{-6} Pa and 10 kPa.
The pressure gauges for measuring the pressure inside the tank is directly connected to the vacuum tank with a flange. The pressure gauge for measuring the pressure in the injector head is connected through a DIN 04/06mm pipe which is screwed beneath the injector head.

Table 5.4: PFEIFFER-Vacuum PKR 251 Pressure Gauge specifications

Description	Value
Pressure Range (air,N_2)	5×10^{-7} Pa to 100 kPa
Accuracy[0]	±30%
Reproducibility[0]	±5%
Output Signal	0 to 10.5 V

5.4.4 Cooling Subsystem

The cooling system is needed to keep the temperatures low for all the subsystems of the facility during operation.
A scheme of the actual cooling system for the facility is shown in Fig. 5.11. Water cooling is necessary for the VAROVAC vacuum pump, for the generator, the calorimeter and the oscillator circuit, as well as for the power supply.
The water cooling circuit is divided into an open and a closed circuit. The open circuit involves the heat exchanger and the VAROVAC vacuum pump. The closed circuit is composed by a reservoir always filled with water, from which two water pumps of 90 L/min mass flow and 6 bar of inlet pressure, pump the water into the system. The outlet, with water at higher temperature since it absorbed heat from the facility, will flow into the heat exchanger to cool down and pumped back into the reservoir.

[0] 5×10^{-6} Pa and 10 kPa

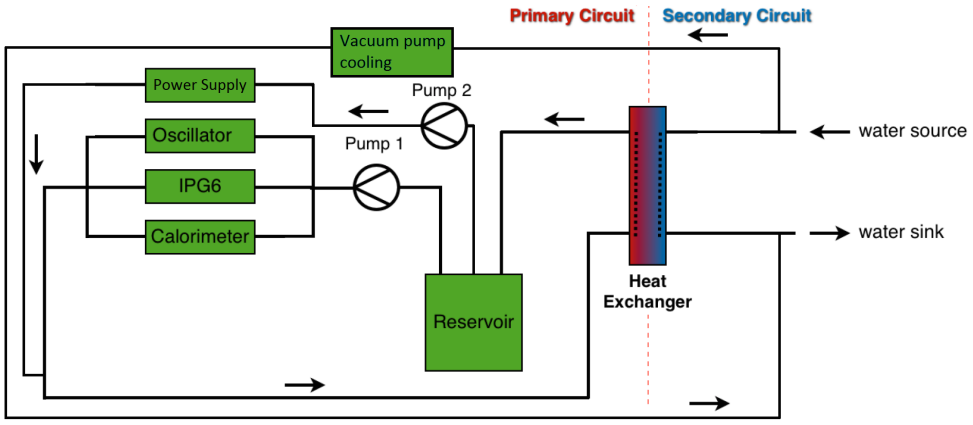

Figure 5.11: Facility cooling system [1].

Cooling Subsystem Improvement

A modification of the cooling system has been made. This was needed due first of all to adapt the system to the new water-cooled bottom flange, but also to enhance the accessibility to the control valves and to increase the overall security of the facility. First a rearrangement of the disposition of the pipes has been made in order to drastically separate them from the power cables to avoid danger of short circuits.
All the power cables are now on a higher level than the water pipes which are mostly laying on the ground. A main change of the facility has been made in the control valve assembly which has been compacted and hung onto a wood plate connected with screws to the frame which holds up the vacuum chamber as shown in Fig. 5.12.

Vacuum Pump

The vacuum pump requires its own cooling, achieved by two pipes of DIN 10/12mm. The inlet is connected from the inlet of the main water supply to the pump and the outlet pipe, of the same size, is connected from the pump to the outlet of the main water supply of the facility. The valve is kept fully open during operation.

Power Supply

The cooling of the power supply was a limitation with the introduction of the new bottom flange.
Due to lower water mass flow and pressure, the cooling of the power supply became critical since it yield to a sudden shutdown during tests. Indeed the power

supply is one of the greatest sources of heat for the facility.
Different combinations have been tested and the best was found to provide the cooling of the power supply with an own pump. Water is taken from the reservoir, pumped into the water supply with 13 mm internal diameter pipes and sent directly to the heat exchanger.

Oscillator Circuit

The pipes for the oscillator circuit have been lengthened, brought to the ground and connected to the valve assembly. The water flows first into the oscillator circuit, and afterwards into the coil providing the necessary cooling. The pipes has been lengthened with DIN 10/12mm and connected to the valve assembly. The valve for the water flow control for the oscillator circuit cooling are on the outlet side of the valve assembly.

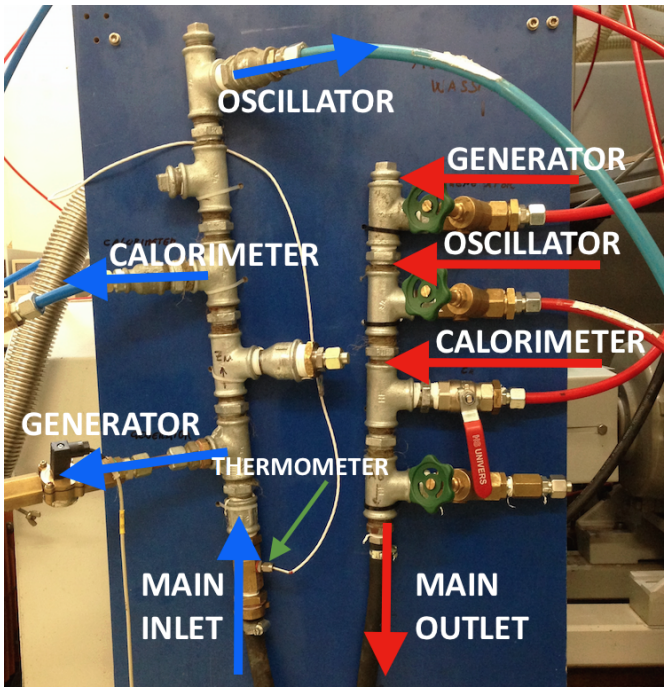

Figure 5.12: New valve assembly for the water cooling system.

Calorimeter

The calorimeter serves as plasma diagnostic device.
The use of thinner pipes to reduce the error on the evaluation of the enthalpy of the calorimeter has been selected and the larger pipes with the size of DIN

10/12 mm have been substituted with thinner pipes with the size of DIN 04/06mm. First water tests revealed that the mass flow measurement device on the inlet of the calorimeter was not able to show any value since the mass flow rate was too low for the device. Therefore, the outlet and the inlet pipes have been substituted again with a DIN 10/12 mm pipe and values of the water flow rate could have been read again from the device. In order to anyway reduce the error on the evaluation of the enthalpy, the last ca. 10 cm of the pipe reaching the calorimeter, has been kept with the thinner diameter of DIN 04/06mm. On the outlet pipe of the calorimeter is attached a thermocouple which measures the temperature of the water as it leaves the vacuum chamber; the outlet is attached to the valve assembly with a valve which commands the water flow rate to the calorimeter during the operation of the generator, in this way the calorimeter is always filled with water.

Generator

An important modification in the cooling of the generator has been made due to the introduction of a new designed water-cooled bottom flange. In the precedent design the water cooling had one inlet, with the size of DIN 04/06mm, at the bottom of the case. As mentioned before the new water-cooled bottom flange consists of 8 radial inlet ducts and therefore 8 pipes must connect to the bottom flange. Different designs have been evaluated and the chosen one is explained as following. From the water assembly a main pipe with the size of DIN 10/12 mm is attached, a manometer as shown in Fig. 5.12 is connected with a T-connection to measure the pressure at the generator inlet, and reaches a V-shape junction as seen in Fig. 5.13(a).

From this junction two pipes with the size of DIN 04/06mm are connected and reach the top of the vacuum chamber. Since, as stated before, near the plasma it preferable to not use metallic parts, plastic connection have been chosen for the water-cooled bottom flange. In the Fig. 5.13 it is shown how the two inlet pipes are connected and how the water is afterwards distributed to the 8 ducts with the use of T- and L-connections. The material of these connections is PVDF which has the characteristics represented in Tab. 5.5. In the figure Fig. 5.13(b) the new water-cooled bottom flange (without the closure) is shown with the PVDF's connections connected.
Adding the new bottom flange with 8 inlets required an higher water mass flow to the generator than in the precedent configuration. During the first water tests which were including also the power supply and oscillator circuit tests, opening the valve for the generator cooling caused the power supply to shut down due too low water flow for the cooling.

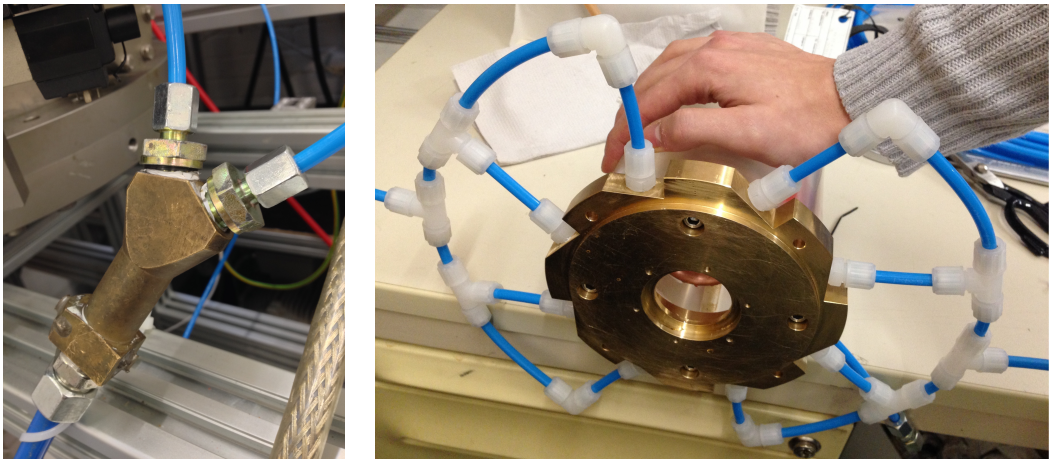

(a) (b)

Figure 5.13: New water connections for the bottom flange.

Table 5.5: PVDF characteristics [53].

Material	Operating Temperature °C	Density g/cm^3	Tensile Strength (at 23°C) N/mm^2	Melt index MFR $g/10min$
Polyvinyl--idene fluoride	$-40/+140$	1.75	38-50	6

Water Temperature

To have an indication of the temperature of the water in the cooling circuit, 4 thermocouple PT100 Class A are collocated into the circuit. These sensor are implemented into a Data-scan which converts the signal output to digital data visualized on the screen of a computer through a software. One thermocouple is mounted on the main inlet, see Fig. 5.12, of the water cooling circuit and provides information of the temperature of the water entering the cooling circuit, hence of the temperature of the water in the reservoir, see Fig. 5.11. This value will be used as the inlet temperature for all the components. Another thermocouple is placed between the outlet of the generator and the inlet of the injector head, the water heats up as it flows inside the casing of the generator and leaves the generator at a higher temperature, this to measure the power absorbed by the cooling of the quartz tube. Another thermocouple is then mounted at the outlet of the injector head in order to have information about the power absorbed by the injector. The last thermocouple is positioned at the outlet of the calorimeter,

close to the vacuum tank, this has been done in order to have the value of the temperature of the water after flowing in the calorimeter and being heated by the plasma exiting the generator, this will be used to determine the power absorbed from the plasma by the calorimeter.

Water Flow

Two flow controllers are FCH-C-Ms from the producer Bio-Tech, and are inserted into the cooling system in order to provide information about the mass flow rate of the water flowing into the circuit. The first measures the water flow directed to the generator and the second measures the water flow directed to the calorimeter. The operational range of the available water flow meters is between $0.50 - 30.0\,\mathrm{L/min}$ for water at a temperature of $22\,^{\circ}\mathrm{C}$ with an accuracy given by the producer of $\pm 2\%$. The signal produced by the device is sent to an electronic converter produced by Bio-Tech, which converts the AC signal of $50 - 130\,\mathrm{Hz}$ to a $0 - 10\,\mathrm{V}$ DC signal readable from the Data-scan. The flow meters operate at DC with voltage of $24\,\mathrm{V}$, an AC/DC transformer is needed and plugged to the a standard electric plug. Calibration is needed for the implementation of the flow meters into the Data-scan.

Water Pressure

The pressure of the water in the cooling system is measured by a manometer placed on the generator inlet. It is an analog device with a resolution of $1\,\mathrm{bar}$ over the range $0 - 20\,\mathrm{bar}$.

5.4.5 Gas Supply

Different gases are used for plasma generation in IPG6-S. Those are stored in pressurized vessels that are connected through a pressure reducer and a flow controller to the injector head of the IPG6-S. A secondary gas injection is available on the back of the vacuum tank to regulate the pressure of the tank.
The mass flow controllers installed are F-201AV-50K models from the producer Bronkhorst. They operate between a mass flow of $20\,\mathrm{mg/s}$ and of $230 - 250\,\mathrm{mg/s}$ with steps of $1\,\mathrm{mg/s}$ depending on the gas. According to the producer, the accuracy of these mass flow controllers is of $\pm 1\%$ for volume flows between $5 - 10\,\mathrm{mL/min}$ and of $\pm 2\%$ for volume flows between $0 - 5\,\mathrm{mL/min}$.
The Tylan FC-2900 has been introduced to reach lower mass flows. The performance from the manufacturer is of a full range between 10 sccm and 10 slpm with an accuracy of $\pm 1\%$ and a linearity of $\pm 0.5\%$ both in full range. That means in a mass flow from about $20\,\mathrm{mg/s}$ down to about $0.2\,\mathrm{mg/s}$ depending on the gas.

The output is a voltage between 0 and 5 V which is directly related with a factor 100 to the mass flow in mg/s.
Gas, in this case oxygen, is provided by a pressure vessel. The gas is brought to the mass flow controller through a pipe at a pressure of 5 bar, given by a reducer valve mounted on the pressure vessel.

5.4.6 Cavity Calorimeter

The cavity calorimeter, developed by [47] is installed into the vacuum tank to determine the plasma power.

It is a cone made of copper, see Fig. 5.14, inside the cone a copper pipe traversed by water is attached as a spiral, copper pipes are also attached on the outside wall of the cone.
Its working principle is similar to an heat exchanger.
Hot plasma enters the cavity calorimeter, that has the shape of a cone, through an entrance hole that is 50% larger than the diameter of the quartz tube of IPG6-S.
The plasma inside the calorimeter transfers the majority of its power to the calorimeter's walls and inner pipes through convection, radiation and recombination.

Figure 5.14: IPG6-S Calorimeter [47].

The transfer of power results in a temperature increase of the water flowing in the pipes of the calorimeter.
The difference of temperature between the water entering and leaving the calorimeter is read by two thermocouples and used to calculate the power as in Eq. 5.1 and subsequently the enthalpy as in Eq. 5.2.
For the experiment the calorimeter has been placed to the nearest position to the exit of the generator, 2.5 cm.

$$P_{cal} = \dot{m}_{water} C_{p,water} (T_{cal,out} - T_{cal,in}) \tag{5.1}$$

Where $\dot{m}_{water}$ is the water flow into the calorimeter, $C_{p,water}$ is the specific heat capacity of the water and T is the temperature of the water at the outlet and at the inlet of the calorimeter.

$$h_{cal} = \frac{P_{cal}}{\dot{m}} \tag{5.2}$$

Where $\dot{m}$ is the air mass flow to the generator.

5.4.7 Plasma Jet Condition

In the precedent design, according to [1], there were interactions between the plasma leaving the generator and the chamber walls.
This was determined by the size of the vacuum chamber, which is small, but also by the fact that the plasma leaving the generator was not concentrated, but the plume had a large angle of diffusion as shown in Fig. 5.15(a).
With the introduction of the new brass water cooled bottom flange it has been noted, as can be seen in Fig. 5.15(b), that the plasma leaving the generator is now concentrated to the center.
That is due to Eddie currents that are induced by the generator on the bottom flange. These currents induce a magnetic field which chokes the plasma at the exit directing it into the center.

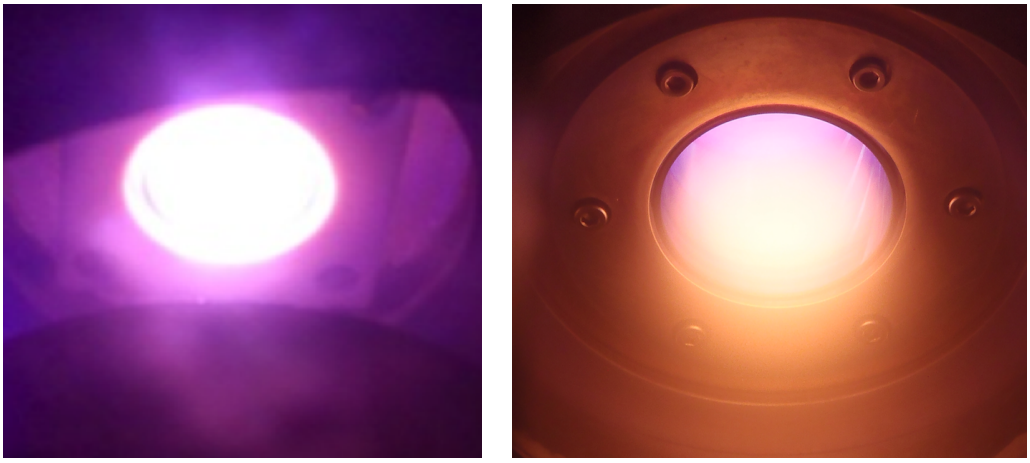

(a) Old Condition. (b) New Condition.

Figure 5.15: Plasma leaving the generator.

Chapter 6

Experimental Set-Up and Results

In this Chapter the test methodology is described and the result are presented. At first, the experimental set-up it is described and the test condition are explained, information about gas type, mass flow and screen voltage are given. Subsequently the test procedure is detailed explained in Sec. 6.2.
The results of the tests are plotted in terms of anode power and current, pressure at the injector head and in the tank. The final results of calculated exhaust velocity, thrust and thrust to drag ratio are plotted as function of altitude and screen voltage.

6.1 Experimental Set-Up

The Experimental Set-Up has been discussed in the precedent Chapter and it is shown, in the last configuration, in Fig. 6.1.

6.1.1 Gas Input

As result of the System Analysis in Chapter 4, the dominant components in the VLEO and LEO altitudes ranges are N_2 and O.
For the tests, air from the ambient and O_2 are used.
Concerning N_2, its presence in the air is of $\sim 78\%$ at ground. From the NRLMSISE-00 model N_2 is always in combination with other elements, therefore choosing to inject air from the ambient is a good approximation.
Atomic oxygen, O, cannot be injected by the gas supply as it recombines into molecular oxygen while storing it at low temperatures and high pressures, therefore O_2 is used as operating gas.
Using O_2 as working gas, requires extra energy for dissociating the oxygen molecules. The simulated environment is therefore a worst case scenario for a RAM-EP application in LEO, where oxygen will be partially or fully dissociated before entering

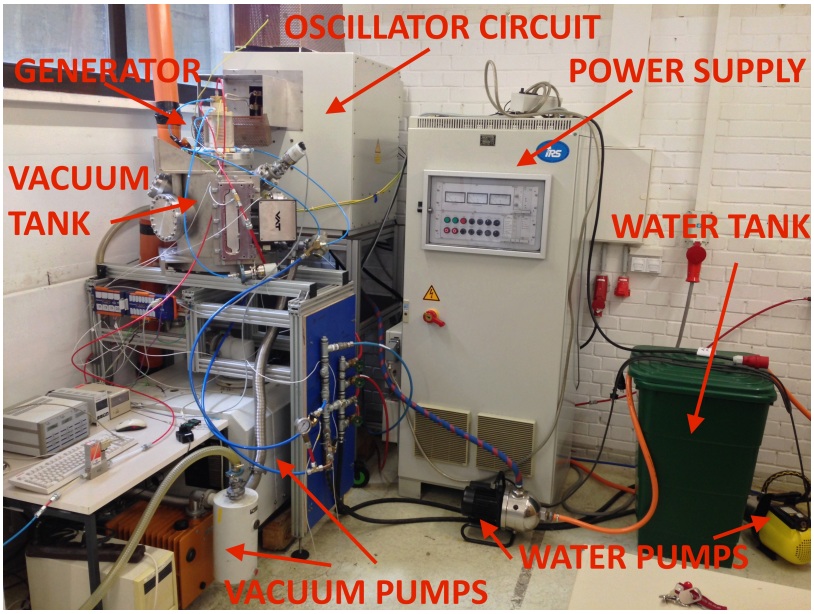

Figure 6.1: Experimental Set-Up.

the thruster.
Air is taken directly from the atmosphere inside the laboratory, oxygen is stored into a pressure vessel and provided to the mass flow controller at a pressure of 5 bar through a pipe and controlled by a reducer valve.

6.1.2 Mass Flow

Mass flow is variated, according to the results of the System Analysis in Chapter 4 and the limitations of the mass flow controller, from a maximum of 120 mg/s to a minimum, depending on the gas, of ~ 0.24 mg/s.
Two kind mass flow controllers are used, the Bronkhorst F-201AV-50K for high mass flows, 120 to 20 mg/s, one calibrated for O_2 and one for N_2; the Tylan FC-2900 has been operated from 90% to 2% for both gases, yielding to a mass flow, depending on the gas, between ~ 20 and ~ 0.24 mg/s.
The tested mass flows are shown in Tab. 6.1.

6.1.3 Screen Voltage

The screen voltages applied from the Power Supply has been chosen to be:

- 0.550 kV;
- 0.850 kV;
- 1.000 kV.

Table 6.1: Mass Flow for Tests.

Flow Controller, FC	O_2 mg/s	N_2, Air mg/s
Bronkhorst F-201AV-50K for O_2 and N_2	120	120
	100	100
	80	80
	60	60
	40	40
	20	20
Tylan FC-2900	20.272	20.130
	17.893	17.767
	15.559	15.450
	10.975	10.898
	6.011	7.458
	4.052	4.023
	2.915	2.895
	1.778	1.766
	0.711	0.706
	0.617	0.613
	0.247	0.245

6.2 Experiment Procedure

Every experiment begins by following the Checklist presented in Appendix CHECK-LIST.
The starting point is of running safely all the subsystems without applying any voltage and current to the generator.
At this conditions it is important that the cooling water temperature is stable for all the thermocouples. The temperature of the thermocouples of the cooling circuit are displayed on the computer of the facility.
When stability condition is achieved for more than one minute, the temperatures are noted down and plasma can be ignited.
The experiments have been divided between those made with oxygen and those made with air, and between high mass flows, 20 to 120 mg/s, and low mass flows, $\sim$ 0.24 to $\sim$20 mg/s.
In each experiments, the three different screen voltages of 0.550 kV, 0.850 kV, and 1.000 kV have been applied.
Each experiments started with the lowest mass flow and the lowest voltage at first.

Once the first mass flow and voltage are set, plasma ignites. In this condition it is waited until the cooling system achieve its steady state condition in particular the temperatures of the water main inlet and the temperature of the calorimeter outlet must be stable. After this condition is achieved for more than 60 s, the plasma is visually checked (color and intensity variations, plasma flickering), tank pressure, p_{tank}, injector head pressure, p_{inj}, anode power, P_{an}, and anode current, I_{an}, are read and noted down on the experiment sheet.
Maintaining the voltage constant, the mass flow is increased to the next value set, again the cooling system must achieve the steady state condition, plasma is visually checked, and the values noted down; the experiment proceeds further until the maximum value for the mass flow is selected.
When the maximum mass flow is reached, the plasma is switched off, the lowest value for the mass flow set is selected and the plasma re-ignited with the new screen voltage value.
The cooling system must again achieve its steady state condition and the experiment proceeds further as explained above.

6.3 Experimental Results

In this Section the results of the experiments are presented in terms of Anode Power, Anode Current, Tank and Injector Head Pressure.
Afterwards the results in terms of Exhaust Velocity, Thrust and Thrust to Drag ratio are presented.

6.3.1 Anode Power

The anode powers read from the analog displays of the power supply are shown in Fig. 6.2 for air, and in Fig. 6.3 for oxygen.
Anode power increases with the increment in mass flow for both gases. For low mass flows the anode power behavior is similar for both gases and for the different voltages.
For mass flows greater than 10 mg/s the anode power increases more for higher than for lower voltages.
A power drop is observed for $V = 0.55$ kV between 10 and 20 mg/s, but this is however inside the uncertainties due to the resolution of the analog instrument which shows the power value.
Double values of anode power are shown at about 20 mg/s of mass flow, this is due to the use of two different mass flow controllers at very close values of mass flows.

The anode power values for the mass flow of 100 and 120 mg/s at $V = 1.00\,\mathrm{kV}$ are not shown due to overload of the facility, thus, no value could be read.

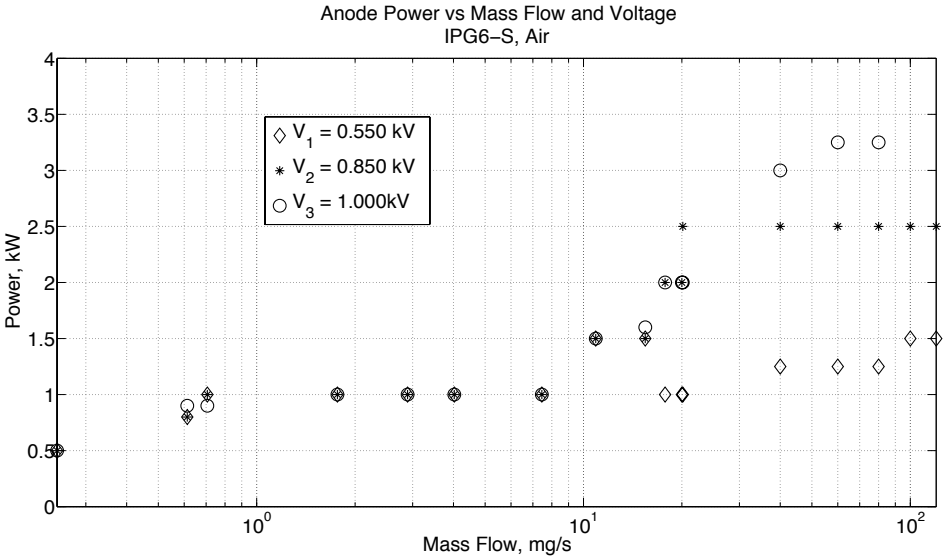

Figure 6.2: Anode Power vs Mass Flow, Air.

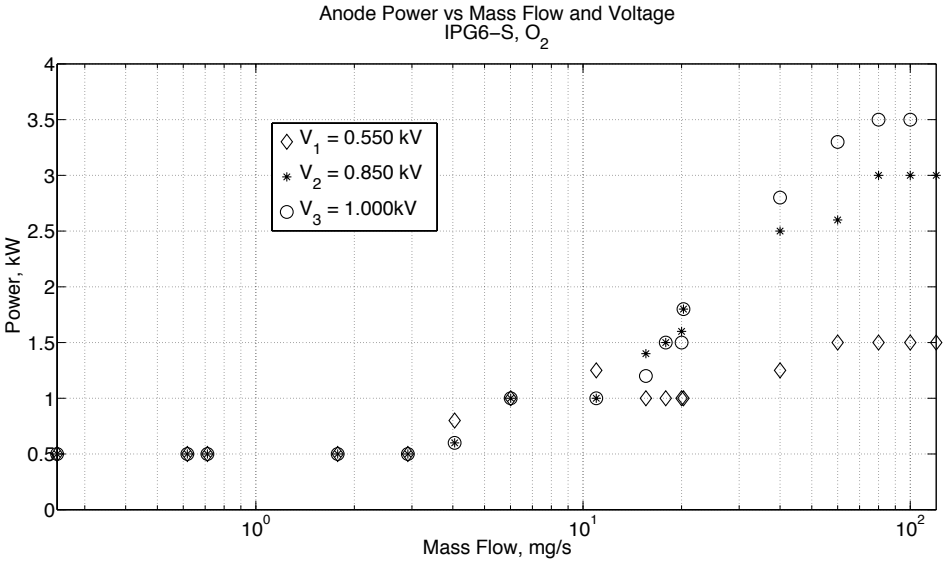

Figure 6.3: Anode Power vs Mass Flow, Oxygen.

6.3.2 Anode Current

The anode currents read from the analog displays of the power supply are shown in Fig. 6.4 for air, and in Fig. 6.5 for oxygen.
Higher voltage implies higher current. For low mass flows, those below $10 - 20\,\mathrm{mg/s}$, the current remains constant but already differentiated for the three different voltages.
The anode current increases for mass flows higher than $20\,\mathrm{mg/s}$.
Double values of anode current are present at a mass flow of about $20\,\mathrm{mg/s}$ due to mass controller switch, as for the anode power.
The anode current values for the mass flow of 100 and $120\,\mathrm{mg/s}$ at $V = 1.00\,\mathrm{kV}$ are not shown due to overload of the facility, thus, no value could be read.

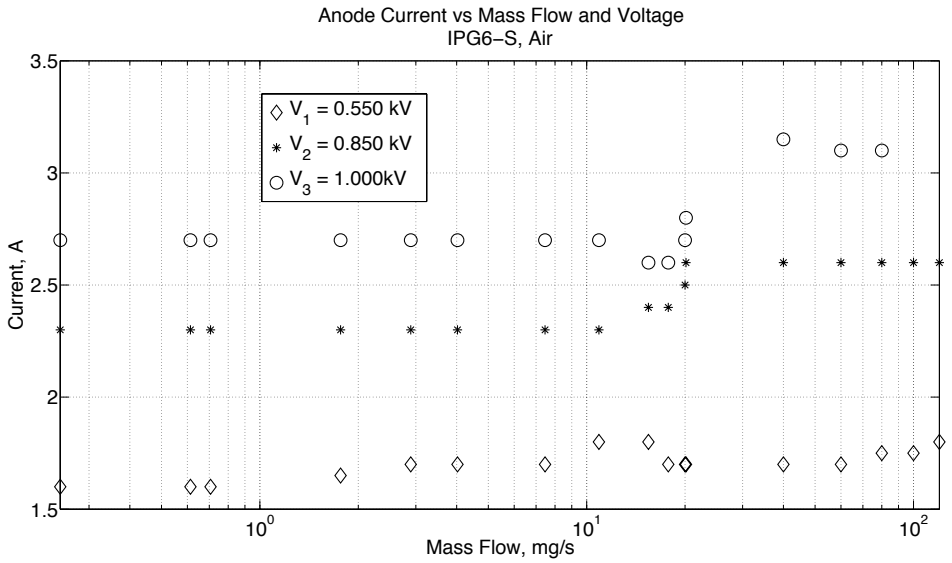

Figure 6.4: Anode Current vs Mass Flow.

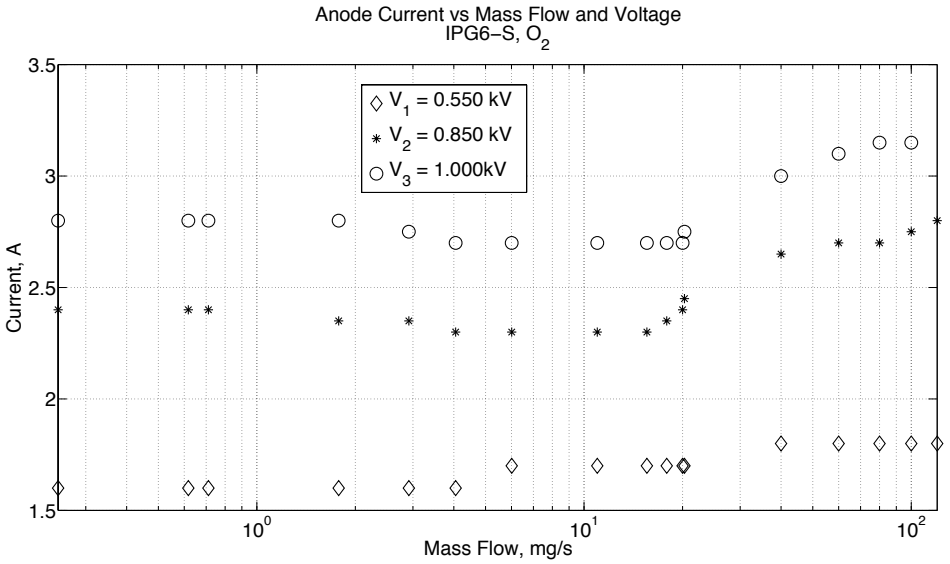

Figure 6.5: Anode Current vs Mass Flow.

6.3.3 Tank and Injector Pressure

The pressure ratio, p_{inj}/p_{tank} is plotted for different mass flows.
The plots show that the pressure ratio is low for low mass flows, as the mass flow increases, the pressure ratio increases and it drops again.
This can be explained as, for very low mass flows, the pressure increment in the tank due to gas injection is very low, thus the pressure in the tank is comparable to the pressure in the injector which makes the ratio close to 1.
As the mass flow is increased, the pressure in the tank increases as the pumps keep sucking the gas from the tank, until a maximum. For higher mass flows the pressure ratio decreases because the suction rate of the pumps is not enough to keep pressure low into the tank.
The results show that with oxygen as injected gas, the pressure ratio does not decrease for high mass flows as much as with air.
Moreover the pressure ratio for higher voltages is higher than with lower voltages.
The values of the pressure ratio for high mass flows, $100 - 120\,\mathrm{mg/s}$ with the applied voltage of 1.00 kV are not plotted as the facility shut down due to overload.

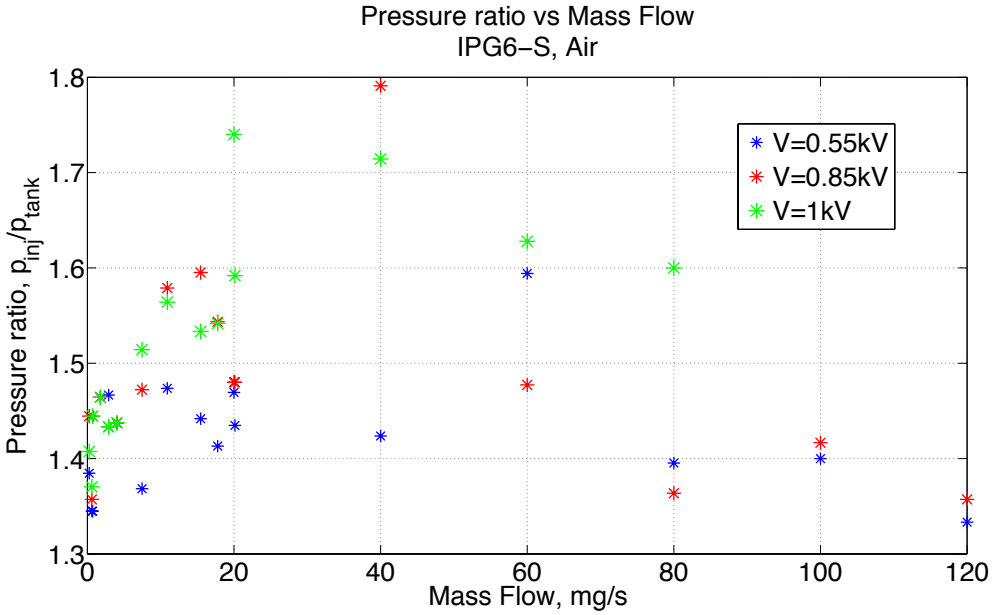

Figure 6.6: Pressure ratio p_{inj}/p_{tank} vs Mass Flow, Air.

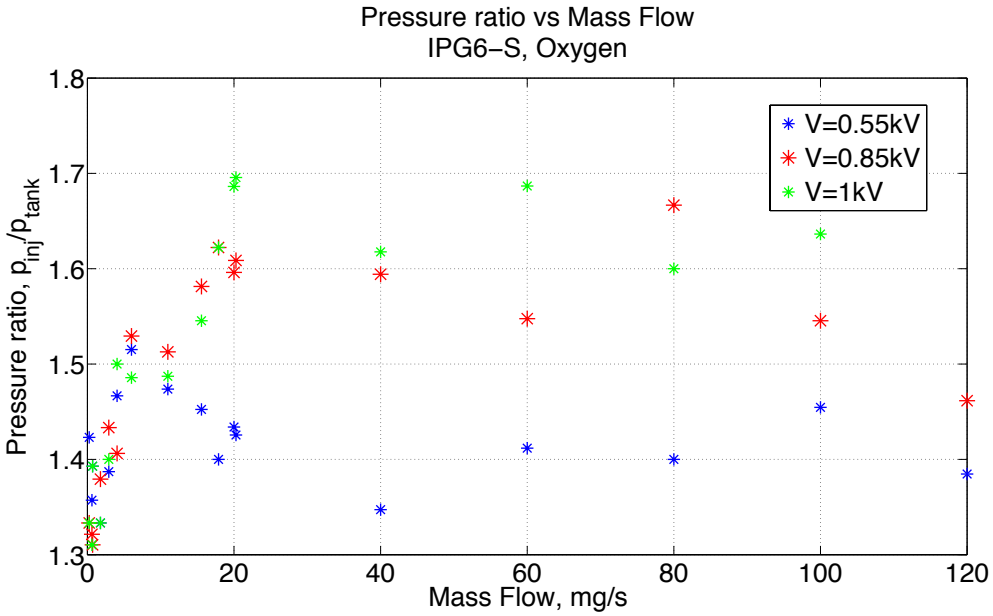

Figure 6.7: Pressure ratio p_{inj}/p_{tank} vs Mass Flow, Oxygen.

6.3.4 Calorimeter Power

The calorimeter power has been calculated with Eq. 5.1.
In order to extract a good value for the calorimeter power in the post processing the first step was to determine the temperature offset between the outlet of the calorimeter and the main inlet, the value has been taken right before the ignition of the first plasma, after reaching the steady state for the cooling system, and introduced in the equation for the calorimeter power calculation as shown in Eq. 6.1. The offset value remained in the range between 0.8 and 1.1 °C.

$$P_{cal} = \dot{m}_{water} C_{p,water} [(T_{cal,out} - T_{main,in}) - \left|\Delta T_{off}\right|] \tag{6.1}$$

As the mass flow increases with a fixed voltage, the power of the plasma increases, as well as the temperatures of the water.
The calorimeter power, P_{cal}, must be read when both the main inlet temperature, $T_{main,in}$, and the calorimeter outlet temperature, $T_{cal,out}$, are steady.
In particular, as shown in Fig. 6.8(a) , the generator outlet temperature, $T_{gen,out}$, shows a clear and fast step as the mass flow is increased. As the increase of mass flow during the experiment has been done every time after reaching the steady state, the time before the step of $T_{gen,out}$ has been taken and used as an input for the P_{cal} diagram, see Fig. 6.8(b), to extract the correct value of P_{cal}. Particular attention has been taken that $T_{main,in}$ and $T_{cal,out}$ were stable at that point for at least 30 s.
The specific heat capacity of the water is of $C_{p,water} = 4.1813 \times 10^3$ J/kgK at 25 °C, as the water temperature at the outlet of the calorimeter during operation remained in the range between 10 and 35 °C.

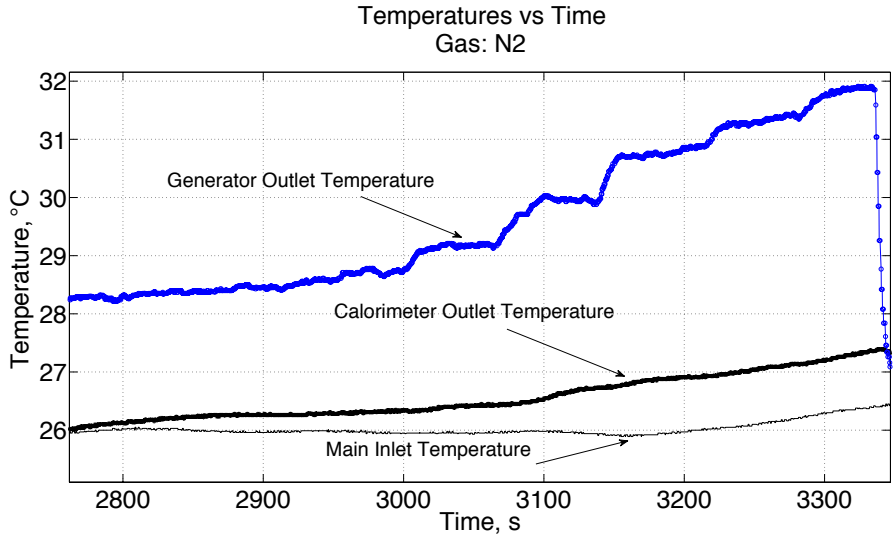

(a) Water Temperatures.

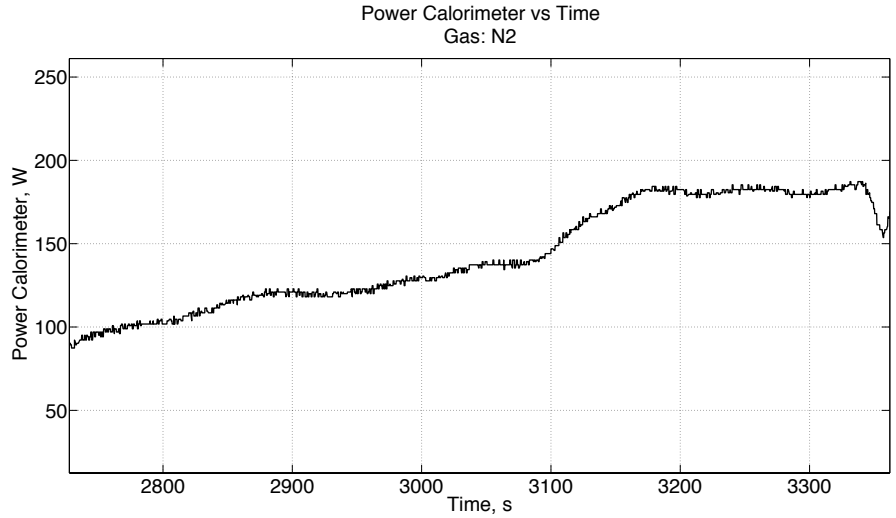

(b) Calorimeter Power.

Figure 6.8: Example of temperature and P_{cal} plots for IPG6-S operating with Air at low mass flows.

6.3.5 Total Efficiency

The total efficiency, η_{tot}, represents the overall performance of the facility.
It is calculated as $\eta_{tot} = \frac{P_{cal}}{P_{anode}}$ and defines how much of the power provided by the power supply remains in the plasma exiting the generator.
The maximum η_{tot} is of 0.306 with O_2 at 2.915 and 0.617 mg/s at a voltage of

0.550 kV and reaches a minimum of 0.072 for a mass flows of 100 mg/s at a voltage of 1.000 kV.
With air, the maximum η_{tot} is of 0.252 at 0.245 mg/s at a voltage of 0.550 kV and reaches a minimum of 0.080 for the mass flow of 80 mg/s at a voltage of 1.000 kV. At low mass flows and voltages the efficiency is higher than at high mass flows and voltages.

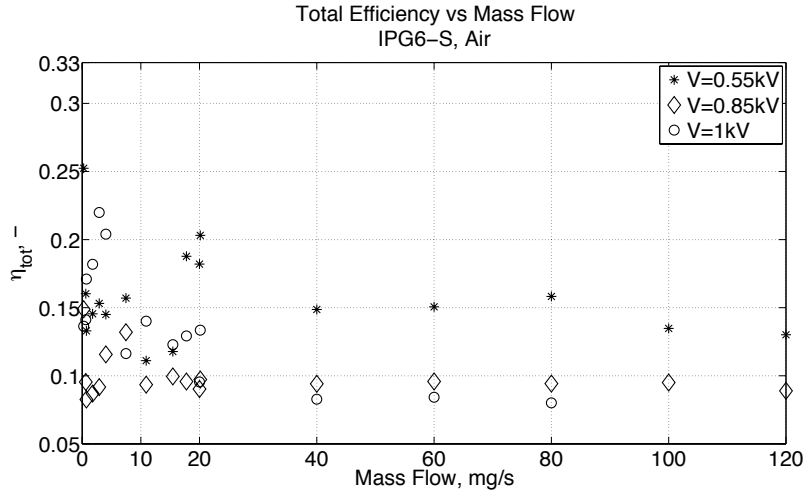

(a) Air.

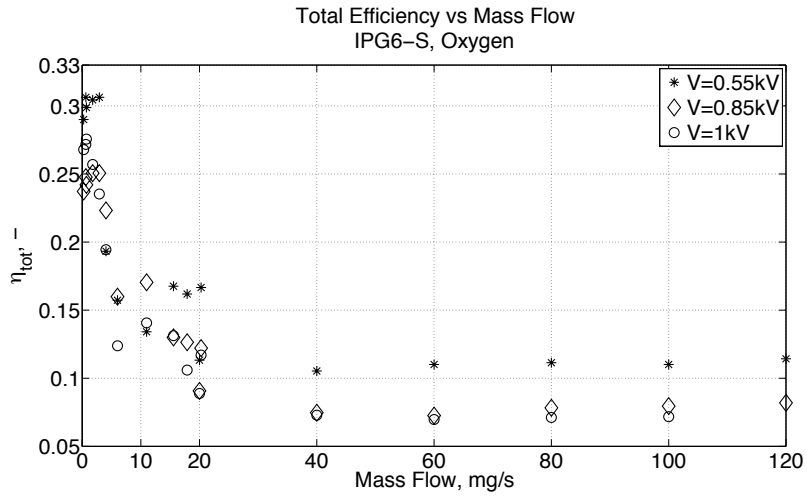

(b) Oxygen.

Figure 6.9: Total Efficiency for IPG6-S operating with Air at low mass flows.

6.3.6 Exhaust Velocity

In the following diagrams the exhaust velocity c_e, derived from the enthalpy as $c_e = \sqrt{2h_{tot}}$, thus from the calorimeter power $h_{tot} = h_{cal} = \frac{P_{cal}}{\dot{m}}$, is plotted as a function of the altitude for different voltages and collection efficiencies, as well as for the two considered inlet areas of 0.3 and 1 m^2. c_e is greater at higher altitudes. Lower voltages yield greater c_e as the altitude increase. Oxygen shows greater exhaust velocities at higher altitudes, exactly where its presence is higher. The highest c_e calculated is of 34 270 m/s with IPG6 operating with O_2 at 0.247 mg/s and a voltage of 0.550 kV. The lowest c_e is of 1690 m/s simulated with IPG6 operating with O_2 at 120 mg/s and a voltage of 0.550 kV.

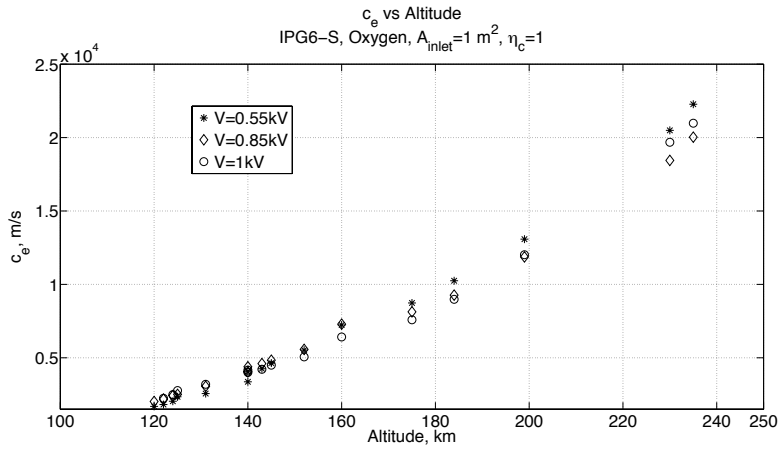

(a)

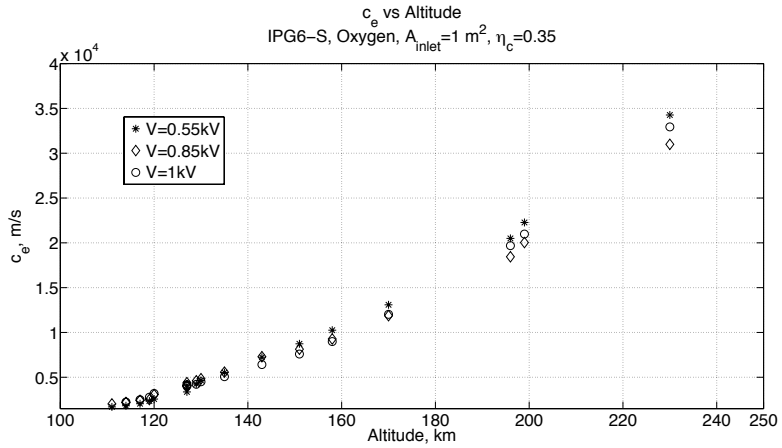

(b)

Figure 6.10: Exhaust Velocity $A_{inlet} = 1\,m^2$, Oxygen.

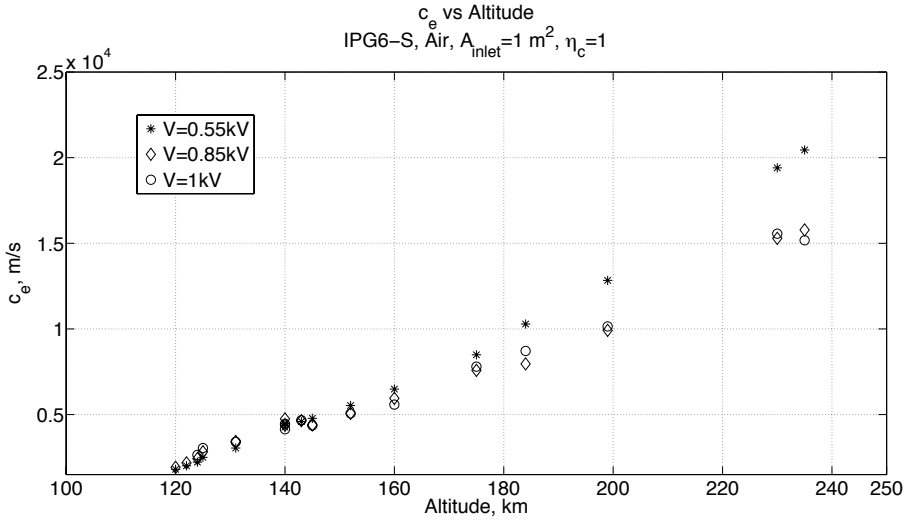

(a)

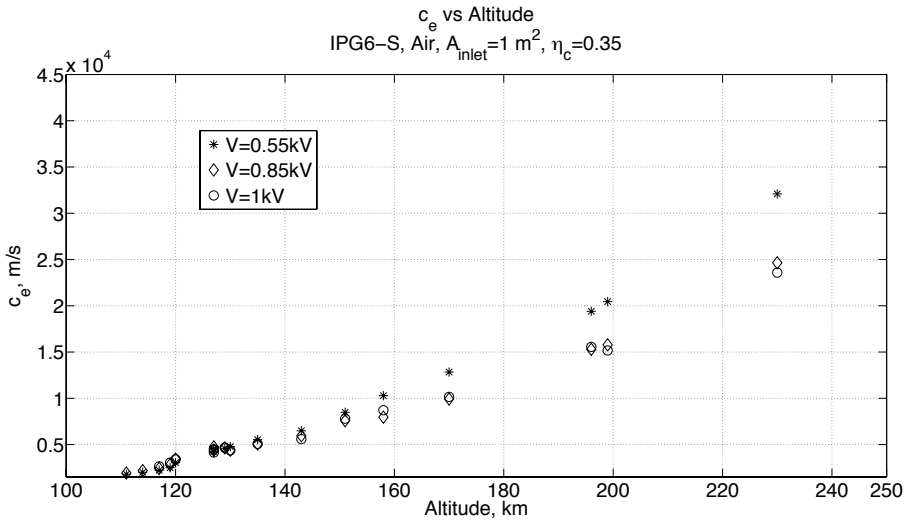

(b)

Figure 6.11: Exhaust Velocity $A_{inlet} = 1\,\mathrm{m}^2$, Air.

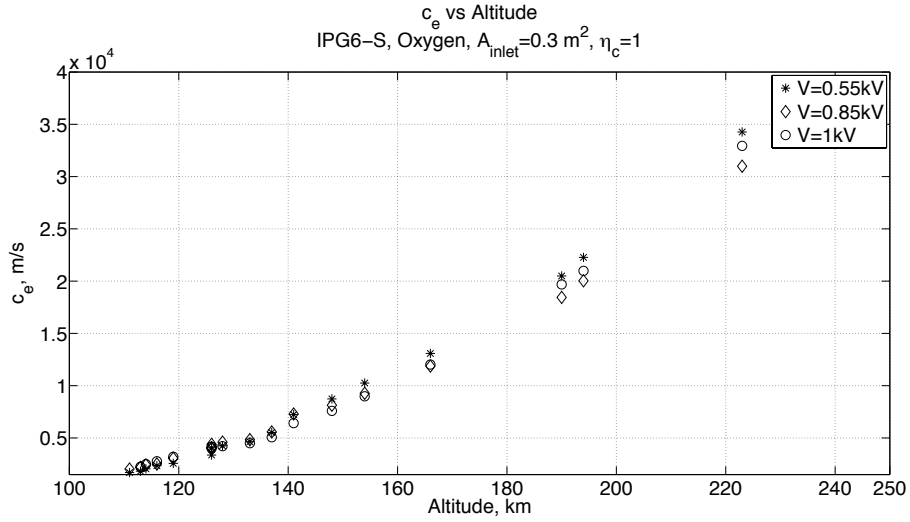

(a)

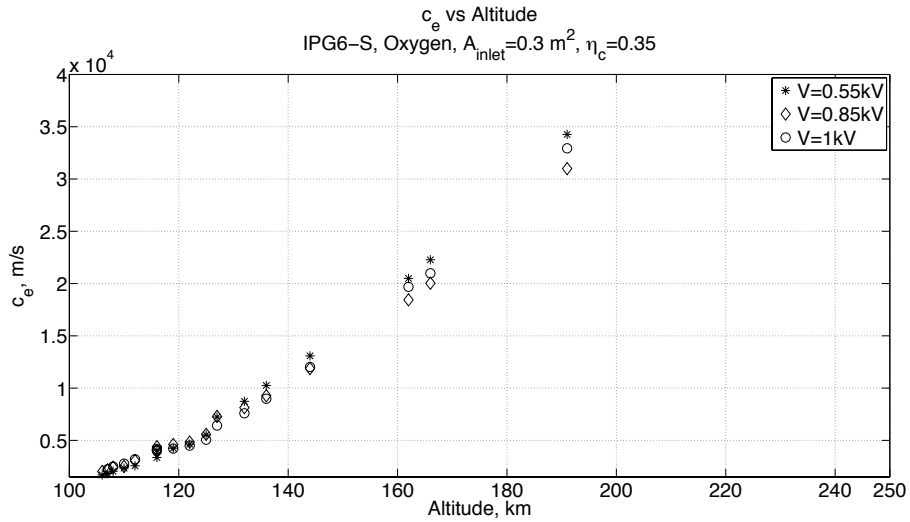

(b)

Figure 6.12: Exhaust Velocity $A_{inlet} = 0.3\,\mathrm{m}^2$, Oxygen.

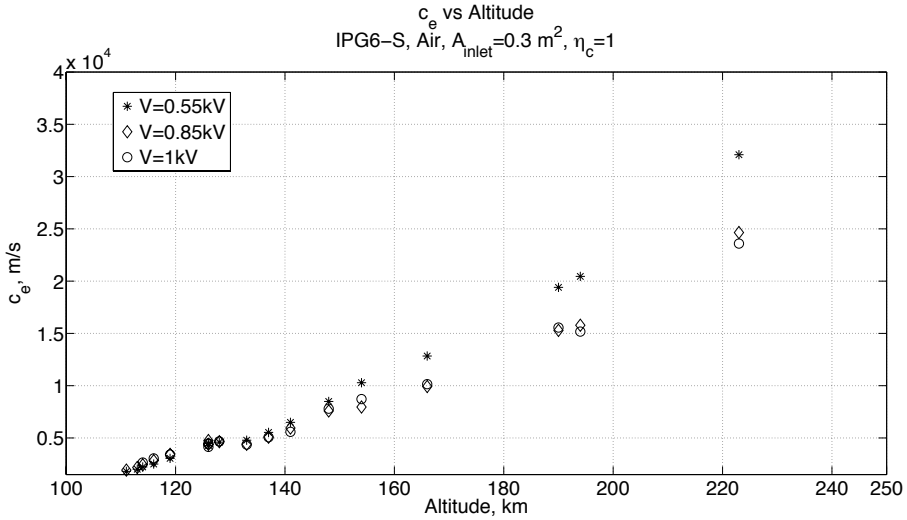

(a)

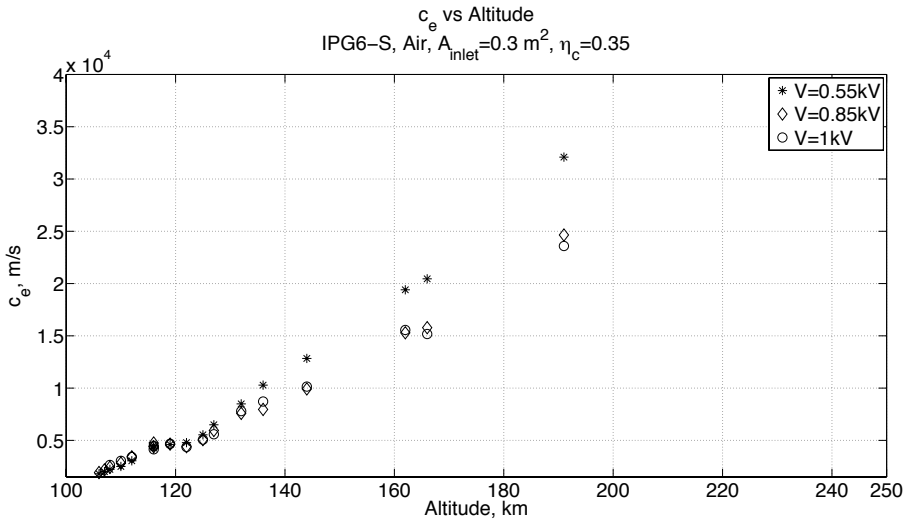

(b)

Figure 6.13: Exhaust Velocity $A_{inlet} = 0.3\,\mathrm{m}^2$, Air.

6.3.7 Thrust

The theoretical thrust generated by IPG6-S operating with different gas, voltages and mass flows is calculated as $T = \dot{m}c_e$ and plotted as a function of the altitude. Thrust reaches a maximum of 250 mN at low altitudes with oxygen, slightly less with Air and a minimum of 5 mN at high altitudes for both gases.

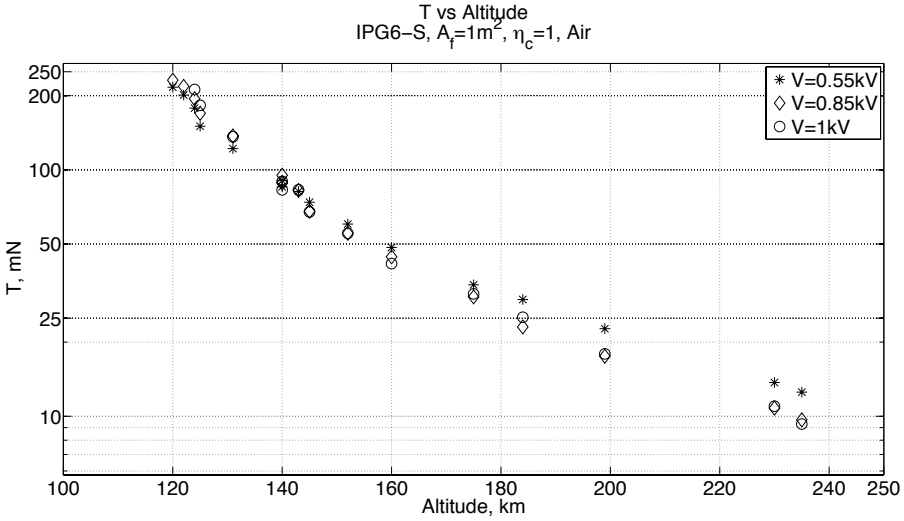

(a)

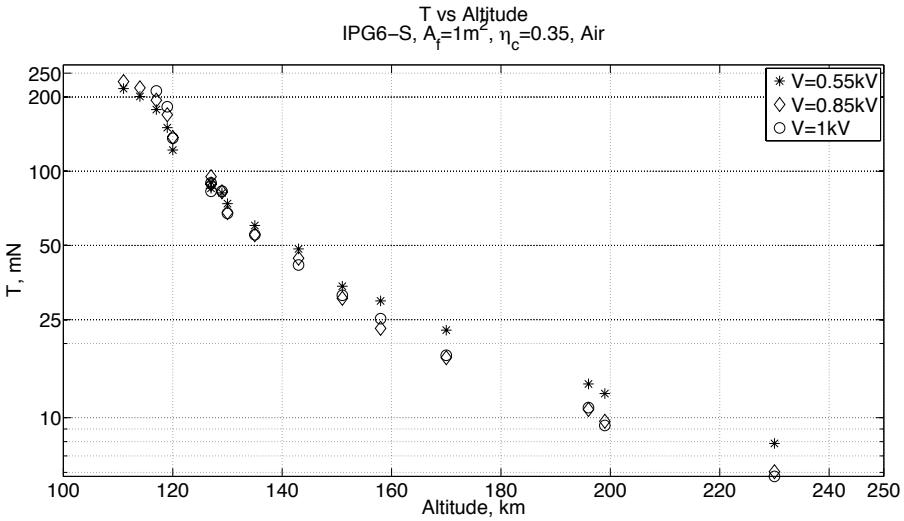

(b)

Figure 6.14: Thrust, $A_{inlet} = 1\,\mathrm{m}^2$, Air.

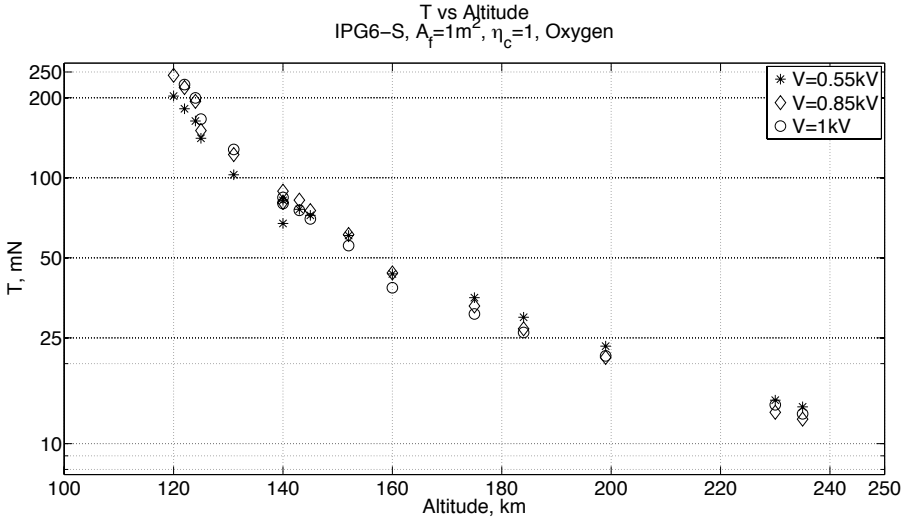

(a)

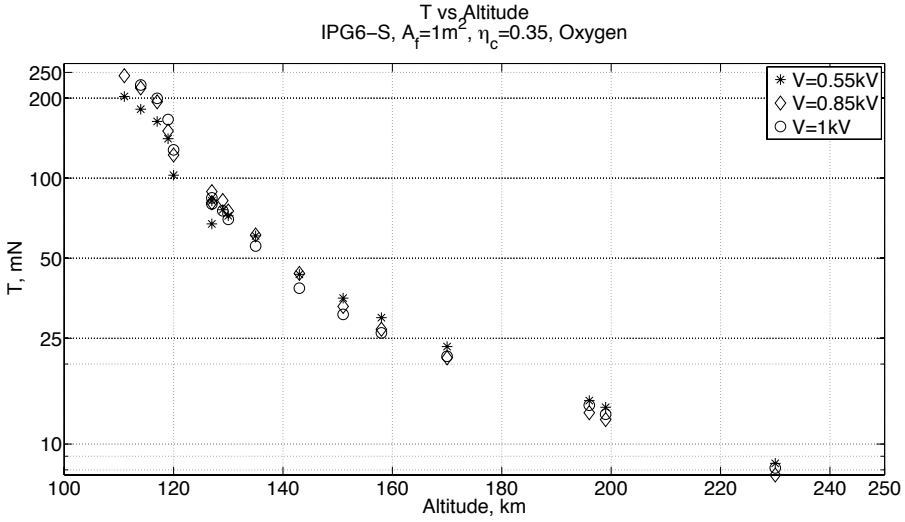

(b)

Figure 6.15: Thrust, $A_{inlet} = 1\,\mathrm{m}^2$, Oxygen.

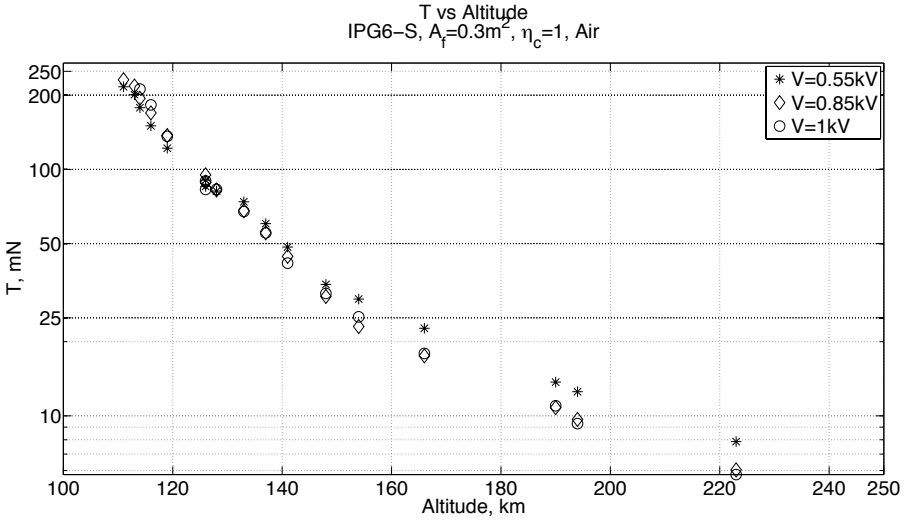

(a)

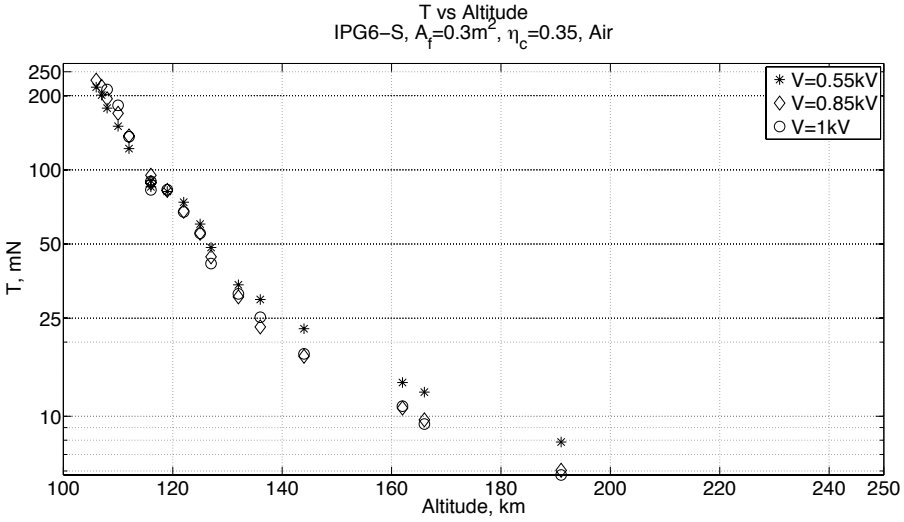

(b)

Figure 6.16: Thrust, $A_{inlet} = 0.3\,\mathrm{m}^2$, Air.

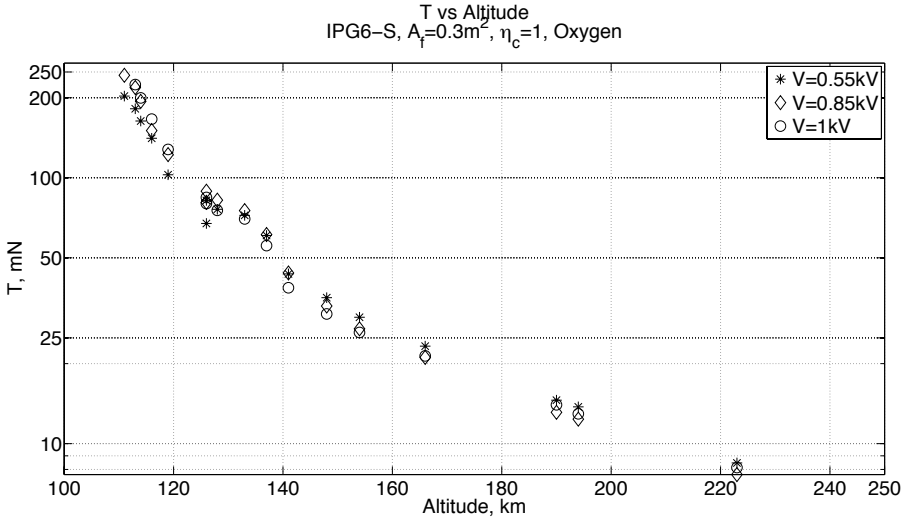

(a)

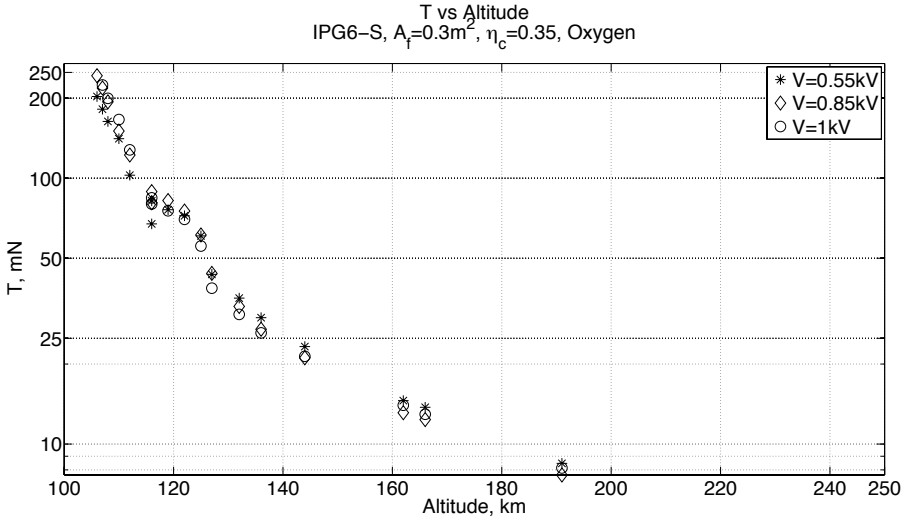

(b)

Figure 6.17: Thrust, $A_{inlet} = 0.3\,\mathrm{m}^2$, Oxygen.

6.3.8 Thrust Density

The thrust density is obtained dividing the thrust by the anode power. A thrust density between 11.56 and 144.43 mN/kW is calculated for air, and between 15.31 and 135.20 mN/kW for Oxygen. It is higher for higher mass flows with air and for low mass flows with oxygen, both with the lowest voltage of 0.55 kV, as shown in Fig. 6.18(b) and Fig. 6.18(a).

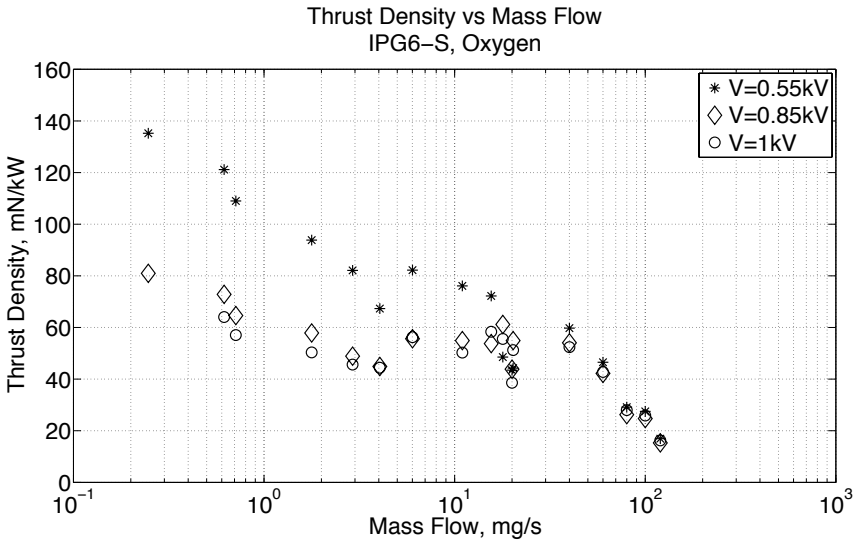

(a) Oxygen.

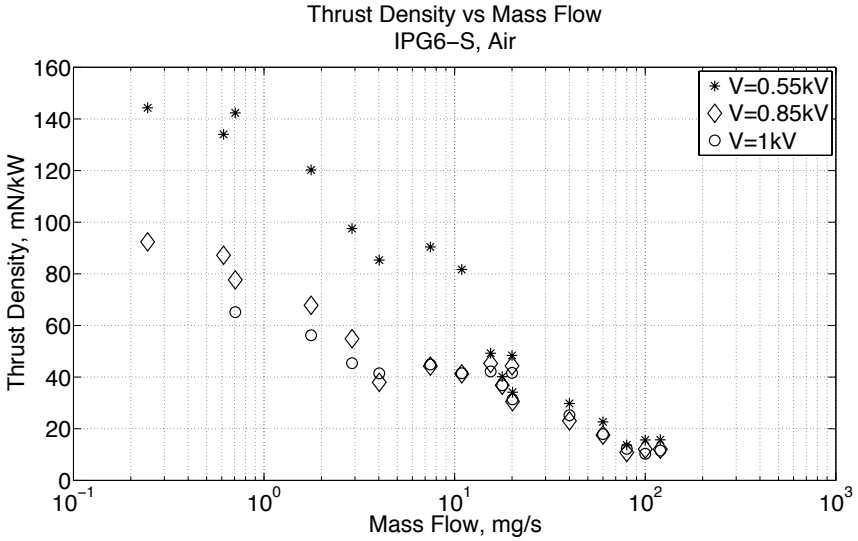

(b) Air.

Figure 6.18: Thrust density.

6.3.9 Thrust to Drag Ratio

Thrust to Drag ratio is plotted as a function of the altitude, of the gas used for test and of the inlet area A_{inlet}.
Each mass flow used in the test corresponds to a certain altitude defined by the model and the collection efficiencies η_c.
The thrust value is divided by the drag value at the corresponding extracted altitude.
In particular it is shown that under these conditions the use of IPG6 as plasma generator for an Air-Breathing Electric Propulsion, full drag compensation is always possible for the different collection efficiencies.

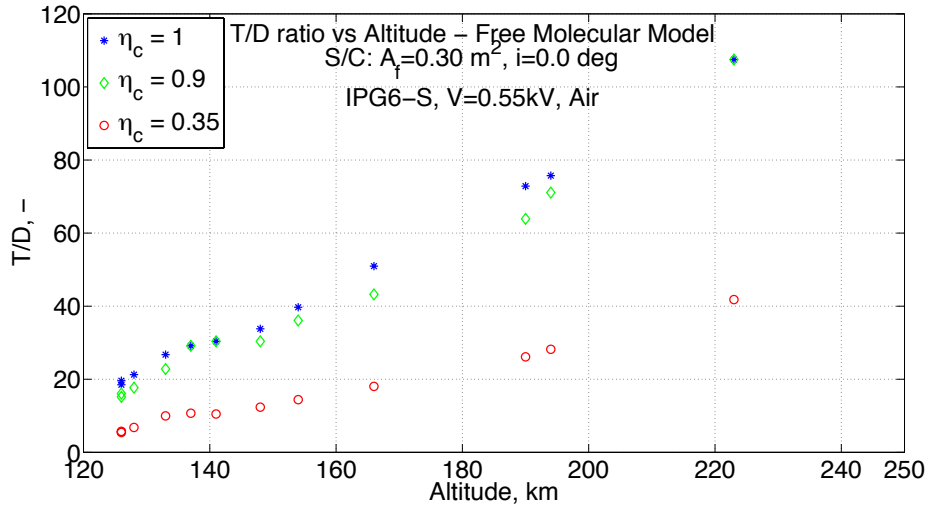

(a) 0.550 kV.

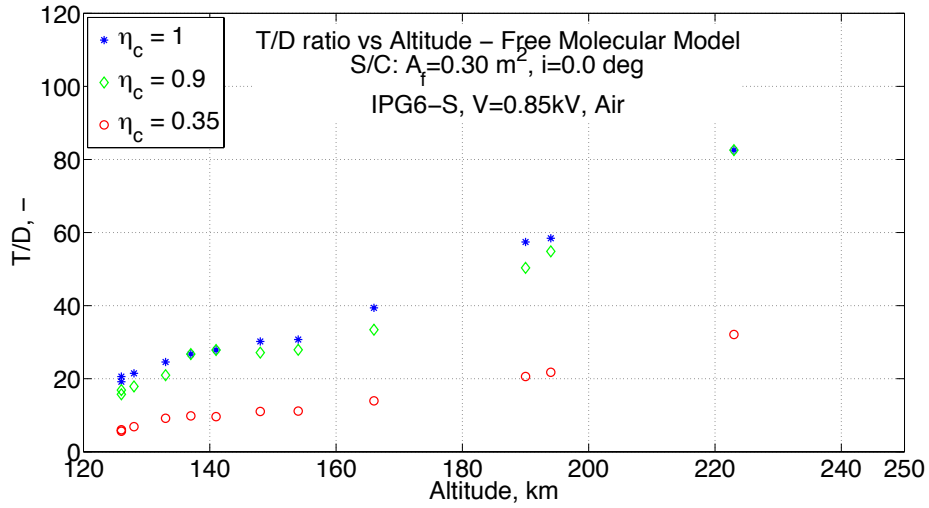

(b) 0.850 kV.

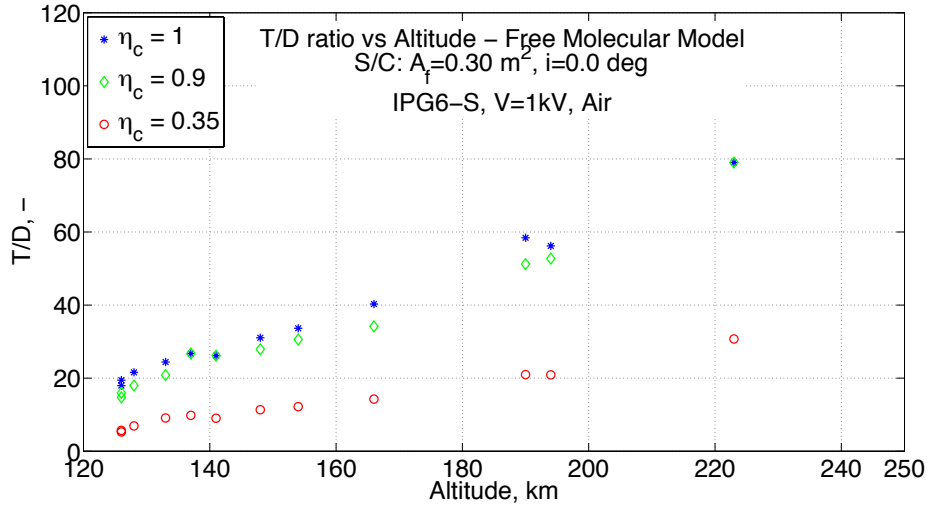

(c) 1.000 kV.

Figure 6.19: Thrust to Drag Ratio $A_{inlet} = 0.3\,\mathrm{m}^2$, Air .

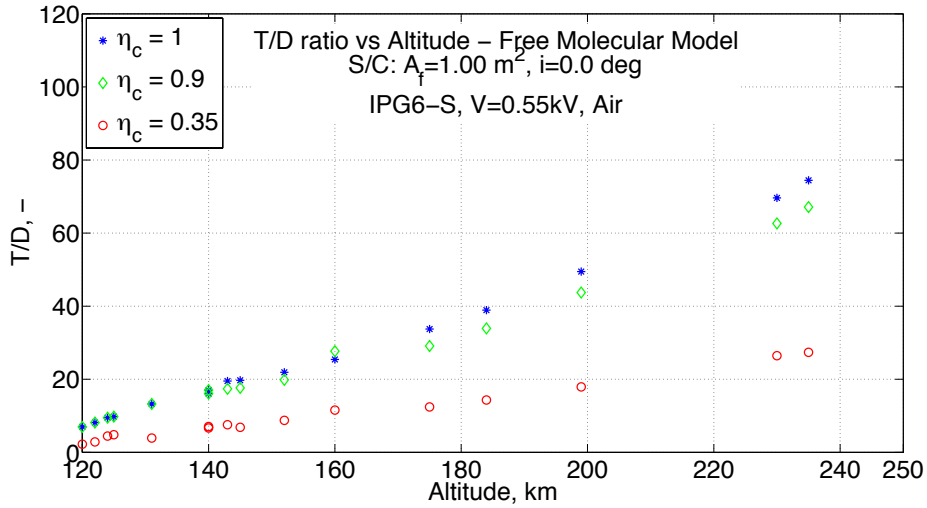

(a) 0.550 kV.

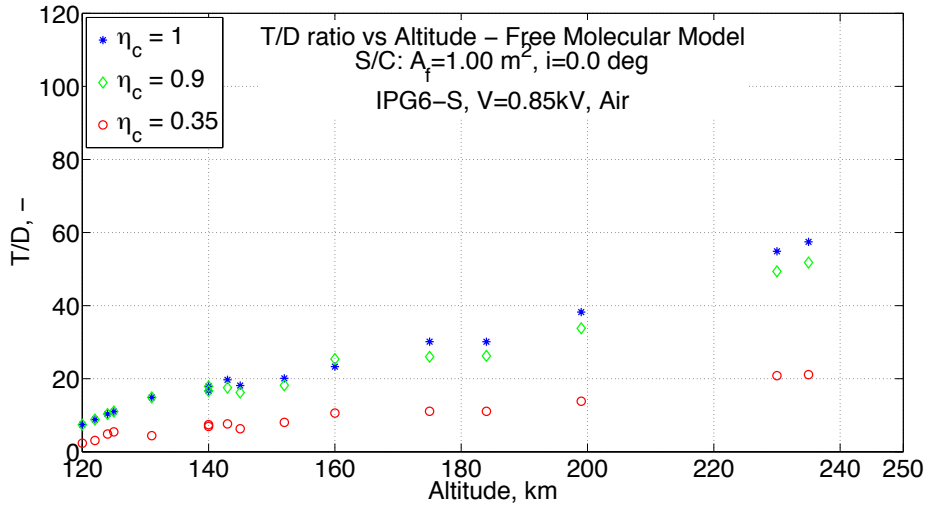

(b) 0.850 kV.

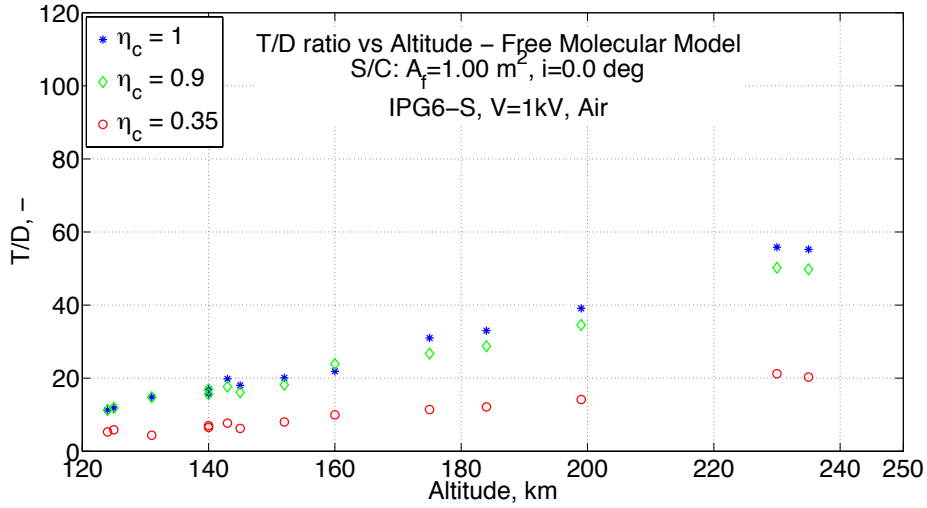

(c) 1.000 kV.

Figure 6.20: Thrust to Drag Ratio $A_{inlet} = 1\,\mathrm{m}^2$, Air .

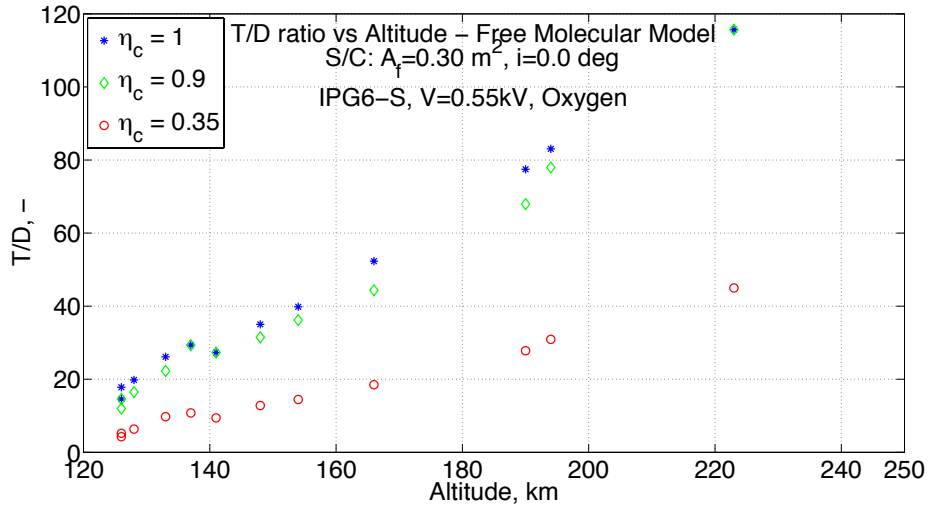

(a) 0.550 kV.

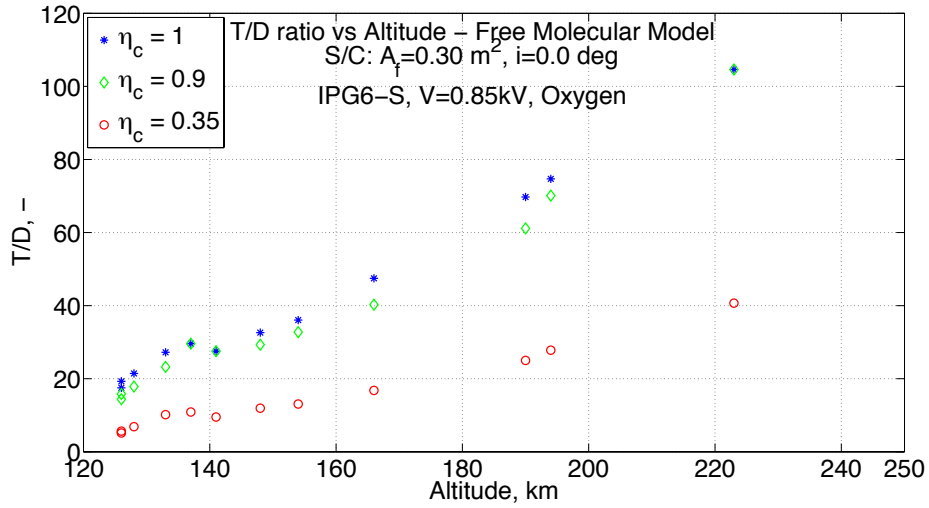

(b) 0.850 kV.

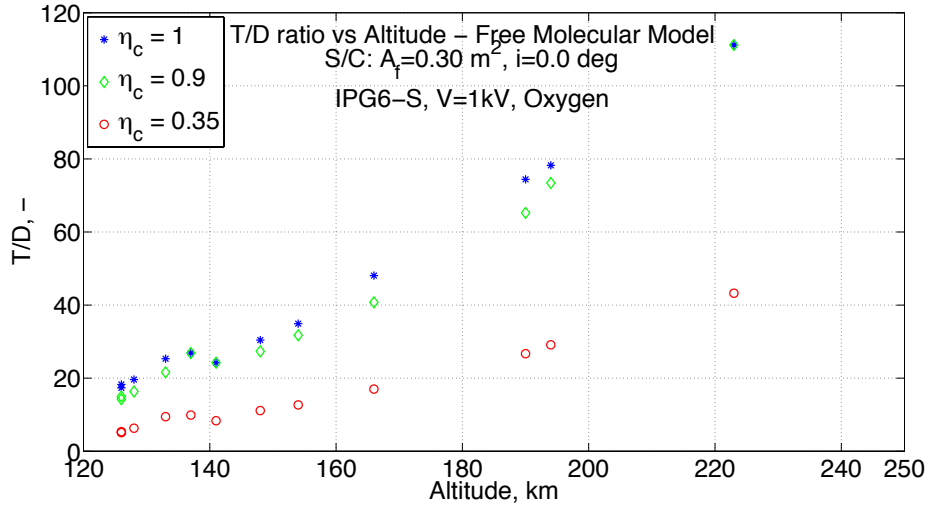

(c) 1.000 kV.

Figure 6.21: Thrust to Drag Ratio $A_{inlet} = 0.3\,\mathrm{m}^2$, Oxygen .

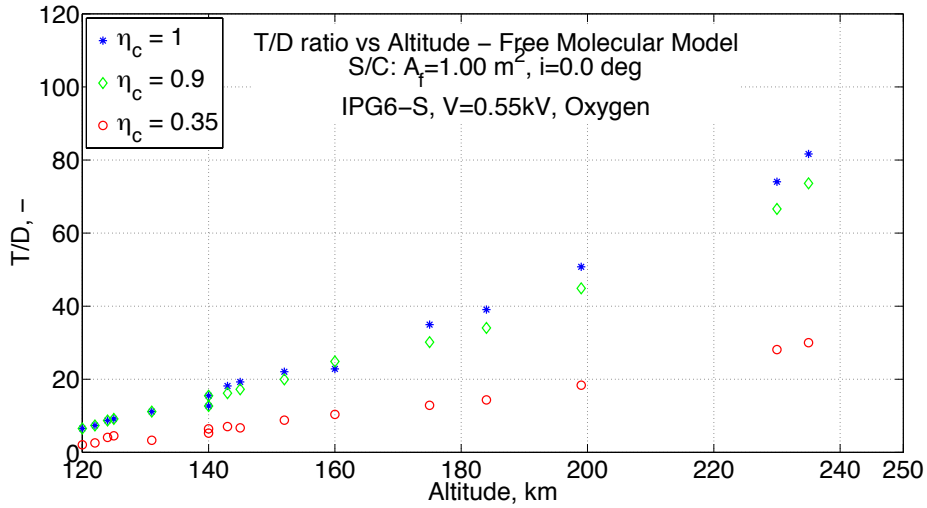

(a) 0.550 kV.

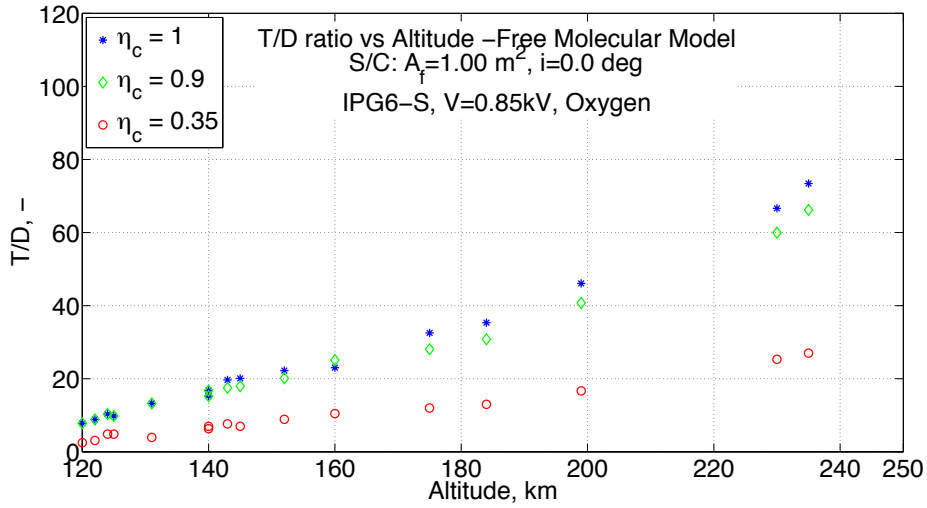

(b) 0.850 kV.

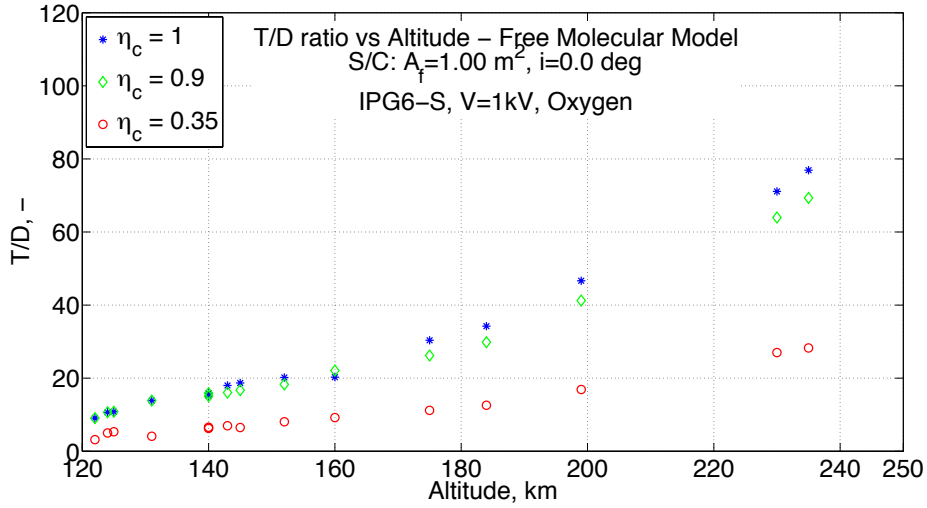

(c) 1.000 kV.

Figure 6.22: Thrust to Drag Ratio $A_{inlet} = 1\,\mathrm{m}^2$, Oxygen .

Chapter 7

Summary

Within this work, a system analysis has been developed to determine the main parameters affecting the design of a mission for a RAM-EP application.
The investigation of these parameters set orbit and altitude ranges, collection efficiencies, input gases, drag to compensate and power available.
IPG6-S has been selected and investigated as a plasma generator for an Air-Breathing Electric Propulsion System application.
The facility has been improved and the generator tested with Oxygen and Air, for mass flows representing different altitude ranges for different intake efficiencies and inlet areas.
The enthalpy of the plasma produced by IPG6 has been evaluated by the use of a calorimeter. Subsequently, the exhaust velocity has been calculated by considering a total conversion of the all the plasma energy at the calorimeter to kinetic energy.
From the exhaust velocity, the thrust has been calculated, as well as the thrust density and the thrust to drag ratio.
Concerning the power, the experiments show that the anode power reaches a minimum of 0.5 kW and a maximum of 3.5 kW which is an acceptable power level for a small S/C, however the power absorbed by the plasma is expected to be even lower as the cooling system absorbs most of the power, as it is shown by the calculation of the total efficiency η_{tot} which is between 0.0697 and 0.3063 for Oxygen and between 0.08259 and 0.2524 for Air.
The difference of pressure is not enough to achieve supersonic discharge, hence a pump with greater suction capabilities is required to increase this pressure difference and obtain better simulation conditions.
Three screen voltages have been applied for the test, 0.55, 0.85 and 1.00 kV.
Low voltages yield higher enthalpies for low mass flows. Vice-versa high voltages yields to higher enthalpies for high mass flows.
Concerning the input gas, air showed better results for high mass flows, when

oxygen showed better results for low mass flows. Low mass flows means higher altitudes. At high altitudes the predominant component is oxygen, that means the performance of the thruster will increase by the altitude as the amount of oxygen will increase.
The thrust to drag ratio has been calculated for the three selected voltages and collection efficiencies, for both Oxygen and Air, as well as for the two different inlet areas in the whole RAM-EP altitude range.
The results have shown that the thrust to drag ratio is always greater than one and full drag compensation might be achieved in all the test conditions.

Chapter 8

Acceleration Strategies

This Section describes potential acceleration strategies for an application to a RAM-EP system with an IPC source.

To convert plasma energy into kinetic energy and maximise the production of thrust, an acceleration strategy is needed.
Some acceleration strategies have been introduced in Sec. 3, however in this section focus on electrodeless acceleration strategies will be made, as the presence of electrodes is a limiting factor on thruster and mission lifetime.
The basic idea is to use electric and magnetic fields to direct and accelerate the ionized particles of the plasma without direct contact between nozzle and particles.
The study from [54] has been investigating different electrodeless acceleration strategies by using an helicon plasma source.

The study included the following acceleration strategies, see Fig. 8.1:

- rotating magnetic field (RMF) acceleration;
- rotating electric field (REF) or Lissajous acceleration;
- ponderomotive acceleration (PA) with ion cyclotron resonance (ICR) acceleration - PA/ICR.

In these concepts the accelerations electrodes are production antennas and are indirect contact with the plasma.

The RMF acceleration device, see Fig. 8.1(a), is a coil wrapped around a quartz glass tube after the plasma source, the induced electron current on the coil, regardless how is it produced, in presence of a flaring magnetic field creates

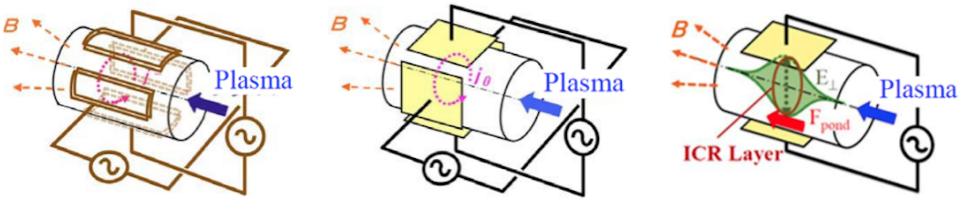

(a) RMF (b) REF (c) PA/ICR

Figure 8.1: Acceleration Strategies, [54].

the axial component of the electromagnetic force which accelerates the ions to generate thrust.

An REF acceleration device, see Fig. 8.1(b), in the presence of a diverging static magnetic field realize what is called Lissajous acceleration concept.
A rotating electric field is applied by two pairs of electrodes in order to induce an azimuthal electron current.
The Lorentz force given by the product of the azimuthal electron current and the radial magnetic field accelerates the plasma in the axial direction.

In the PA/ICR acceleration strategy, see Fig. 8.1(c), ions are first heated perpendicularly by ICR, afterwards RF waves are applied in such a way that the resonance point coincides with the peak of the wave energy density, in this way ions gain parallel acceleration due to ponderomotive force. By the use of the magnetic mirror, their perpendicular energy is converted into parallel energy producing thrust.

Other suitable acceleration strategies involve the VASIMR propulsion system. VASIMR uses an electro-thermal plasma acceleration strategy in which the plasma is first heated by ion cyclotron resonance and subsequently accelerated by a magnetic nozzle.
Electro-static plasma acceleration based on Helicon Double Layer Thruster, HDLT, is where plasma is accelerated by the electrical potential gap between high density plasma inside the source region and the low density plasma in the exhaust.

Proceeding further, an acceleration strategy which can be used is the Field Reversed Configuration - FRC. An FRC, according to the paper from [55], is a self-contained, stable plasma structure that can be accelerated by the use of the Lorentz force, see Fig. 8.2. To obtain this plasma structure a RMF is applied, this ionizes the injected gas by inducing a strong azimuthal current. A magnetic

field that results from this current helps to form and confine the plasma. Gas must be injected, ionized, and then formed into an FRC before being accelerated. The final acceleration is given by a combination of the electromagnetic Lorentz force caused by the cross product between the azimuthal plasma current and the radial component of the bias field, and the gradient magnetic field force given by the conical shape of the thruster.

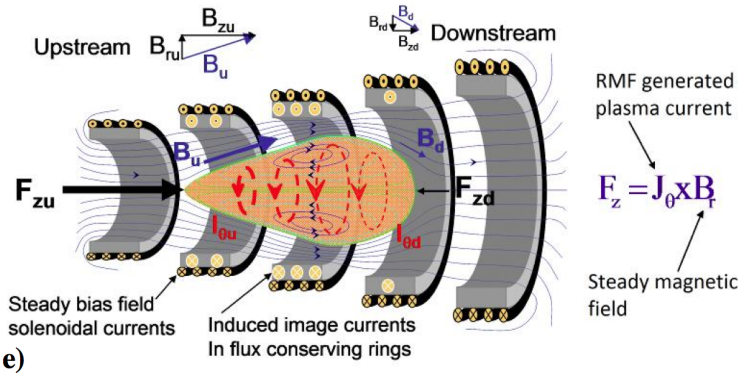

Figure 8.2: FRC Acceleration, [55].

In further works on RAM-EP, in particular with IPG6, a choice of an acceleration strategy should be assessed to determine a more realistic value of thrust.

Prospect and Improvements

To proceed further in the investigation of a RAM-EP system with the use of IPG6, improvements of the facility still have to be made, to achieve more precise results and better ambient conditions. At the same time improvement of the model for the S/C parameters must be calculated.

Simulation Improvements

S/C Computer 3D Model

The development of a 3D S/C model for computer simulation, will allow a better estimation of the parameters.
The use of the 3D model in the thermal analysis will improve the calculation of the heat loads, hence the S/C temperature and the heat fluxes for electric power generation.
A 3D model of the air intake will be used in DSMC and will help in the design and in the estimation of the collection efficiency.

Acceleration Strategy

The investigation of the acceleration strategies will lead to determine first the strategies which best fit to an inductive plasma source, afterwards values of conversion efficiencies from plasma energy to kinetic energy will be used in the simulations to determine a more realistic value of the generated thrust for a concept of S/C equipped with RAM-EP.

REENT Model

A S/C model for the software REENT developed at Universität Stuttgart, in particular including a thrust over altitude profile, will allow determination of the S/C lifetime as a function of the different parameter influencing the T/D ratio.

Facility Improvements

Multi-Stage Vacuum Pump

In particular the introduction of a multi-stage vacuum pump with higher suction rate, will provide lower pressure and better simulation conditions, as the pressure difference between injector head and tank will increase. With the right suction rate, supersonic discharges can be realised and better simulation conditions achieved.

Vacuum Tank

After the installation of a window on the vacuum tank and by removing the calorimeter it has been observed that there is interaction between the plasma and the walls of the chamber. This changes the magnetic and electric fields altering the results.
This issue can be reduced by the introduction of a bigger vacuum tank.

Measurement Devices

The introduction of better measurement devices, in particular water flow meter, thermometers and pressure gauges, will decrease the uncertainty of the measures and will yield preciser and better results.
In particular the lowest measurable water flow from the water flow meters is very close to the water flow of the calorimeter.
Pressure gauges have an uncertainty of the 30%, more precise devices will yield to a better knowledge of the pressures.
Introducing more precise thermometers, in particular for the water main inlet and the calorimeter outlet will yield to preciser values of the water temperatures needed for the calculation of the plasma enthalpy. Moreover the plot of the temperatures during the experiment will facilitate the operation of the facility as the steady state condition can be graphically seen.

Acceleration Device

The introduction of an acceleration device as those explained in Chapter 8, would increase the usability of the results.
However the introduction of an acceleration device might require major modifications of the whole facility, starting from a modified IPG design, ending to modifications of the power supply.

Bibliography

[1] B. Massutí, "Characterization of a miniaturized plasma simulation facility", Master's thesis, Institut für Raumfahrtsysteme, Universität Stuttgart, Sep. 2012.

[2] Expedition7, *Earth seen from ISS*, Apr. 2012. [Online]. Available: http://apod.nasa.gov/apod/ap110412.html.

[3] "System critical design review gravity field and steady-state ocean circulation explorer", Alenia Spazio et al., Tech. Rep., 2005.

[4] Unknown, *Wernher von braun and the F-1*, 1969. [Online]. Available: http://history.nasa.gov/SP-350/ch-3-2.html.

[5] NASA, *Nasa - bimodal nuclear thermal rocket*, May 2008. [Online]. Available: http://www.nasa.gov/centers/glenn/multimedia/artgallery/art_feature_002_BNTR.html.

[6] I. U. Stuttgart, *Elektrische raumfahrtantriebe - universität stuttgart*, Aug. 2012. [Online]. Available: http://www.irs.uni-stuttgart.de/forschung/elektrische_raumfahrtantriebe/index-alt.en.html.

[7] M. Tajmar, *Advanced space propulsion systems*, ser. SpringerEngineering ISBN 3-211-83862-7. Springer-Verlag/Wien, 2003.

[8] I. U. Stuttgart, *Elektrische raumfahrtantriebe - universität stuttgart*, Aug. 2012. [Online]. Available: http://www.irs.uni-stuttgart.de/forschung/elektrische_raumfahrtantriebe/index-alt.en.html.

[9] Arakawa and K. Lab., *Hall thruster research group, university of tokyo*, 2007. [Online]. Available: http://www.al.t.u-tokyo.ac.jp/hall/jp/facility.html.

[10] H. Koizumi, A. Kakami, Y. Furuta, K. Komurasaki, and Y. Arakawa, "Liquid propellant pulsed plasma thruster", *28th Internetional Electric Propulsion Conference*, Mar. 2003.

[11] A. Boxberger, *Magnetoplasmadynamische Triebwerke*, Aug. 2012. [Online]. Available: http://www.irs.uni-stuttgart.de/forschung/elektrische_raumfahrtantriebe/triebwerke/mpd-tw/fremdfeldbeschl-tw/mpd-afmpd.html.

[12] D. DiCara, J. G. del Amo, A. Santovincenzo, B. C. Dominguez, M. Arcioni, A. Caldwell, and I. Roma, "RAM electric propulsion for low earth orbit operation: an ESA study", *30th IEPC, IEPC-2007-162*, 2007.

[13] K. Fujita, "Air intake performance of air breathing ion engines", *Journal of the Japan Society for Aeronautical and Space Sciences*, vol. 52, no. 610, pp. 514–521, 2004.

[14] K. Hohman, "Atmospheric breathing electric thruster for planetary exploration", Busek Co. Inc., 11 Tech Circle; Natick, MA 01760-1023, Final Report, Oct. 2012.

[15] K. D. Diamant, "A 2-stage cylindrical hall thruster for air breathing electric propulsion", *46th AIAA/ASME/SAE/ASEE Joint Propulsion Conference and Exhibit*, no. 6522, Jul. 2010.

[16] ——, "Microwave cathode for air breathing electric propulsion", *31st International Electric Propulsion Conference*, Sep. IEPC-2009-015.

[17] F. Ceccanti and S. Marcuccio, "Earth observation from elliptical orbits with very low altitude perigee", *Conference IAA-B4-0805P*, 2003.

[18] A. Shabshelowitz, "Study of RF plasma technology applied to air-breathing electric propulsion", PhD thesis, University of Michigan, 2013.

[19] L. Pekker and M. Keidar, "Analysis of airbreathing hall effect thrusters", *Journal of Propulsion and Power*, vol. 28, no. 6, 2012.

[20] K. Nishiyama, "Air breathing ion engine", *24th International Symposium on Space Technology and Science*, May ISTS 2004-o-3-05v.

[21] Y. Hisamoto, K. Nishiyama, and H. Kuninaka, "Design of air intake for air breathing ion engine", *63rd International Astronautical Congress, Naples, Italy.*, 2012.

[22] T. Schönherr, K. Komurasaki, F. Romano, B. Massutí, and G. Herdrich, "Analysis of atmosphere-breathing electric propulsion", 2014.

[23] M. Dropmann, G. Herdrich, R. Laufer, D. Puckert, H. Fulge, S. Fasoulas, J. Schmoke, M. Cook, and T. W. Hyde, "A new inductively driven plasma generator (IPG6) - steup and inital experiments", *IEEE Transactions on Plasma Science*, vol. 41, no. 4, Apr. 2013.

[24] J. Picone, A. Hedin, D. Drob, and A. Aikin, "NRLMSISE-00 empirical model of the atmosphere: statistical comparisons and scientific issues", *Journal of geophysical research*, vol. 107, no. A12, 2002.

[25] C. Pardini, W. K. Tobiska, and L. Anselmo, "Analysis of the orbital decay of spherical satellites using different solar flux proxies and atmospheric density models", *Advances in Space Research*, vol. 37, pp. 392–400, 2006.

[26] C. Bizouard, *International earth rotation and reference systems service: useful constant*, Feb. 2014. [Online]. Available: http://hpiers.obspm.fr/eop-pc/models/constants.html.

[27] M. Young, E. Muntz, and J. Wang, "Maintaining continuous low orbit flight by using in-situ atmospheric gases for propellant", *Rarefied Gas Dynamics: 22nd international symposium*, vol. ADA409086, 2001.

[28] NASA, *Estimating the temperature of a flat plate in low earth orbit*, 2000. [Online]. Available: https://www.grc.nasa.gov/www/k-12/Numbers/Math/Mathematical_Thinking/estimating_the_temperature.htm.

[29] J. Wertz and W. Larson, *Space Mission Analysis and Design*, ser. Space Technology Library. Springer Netherlands, 1999, ISBN: 9780792359012.

[30] K. Maeda, N. Kurahara, and S. Nakasuka, "Outline of mission and development of hodoyoshi micro satellites", *Proceedings of ICSANE*, vol. IEPC-2013-287, 2013.

[31] T. Niimi, *High knudsen number flows*, Presentation, Nagoya Univeristy. [Online]. Available: http://gcoe.mech.nagoya-u.ac.jp/basic/pdf/basic-11.pdf.

[32] J. N. Moss, K. A. Boyles, and F. A. Greene, "Orion aerodynamics for hypersonic free molecular to continuum conditions", *14th AIAA/AHI International Space Planes and Hypersonic Systems and Technologies Conference*, Nov. 2006.

[33] D. A. Vallado and D. Finkleman, "A critical assessment of satellite drag and atmospheric density modeling", *Acta Astronautica*, vol. 95, pp. 141–165, 2014.

[34] K. Moe and M. M. Moe, "Gas–surface interactions and satellite drag coefficients", *Planetary and Space Science*, vol. 53, no. 8, pp. 793–801, 2005.

[35] G. Cook, "Satellite drag coefficients", *Planetary and Space Science*, vol. 13, no. 10, pp. 929–946, 1965, ISSN: 0032-0633.

[36] ——, "Drag coefficients of spherical satellites", *Ann. Geophys.*, vol. 22, pp. 53–64, 1966.

[37] M. Moe, S. D. Wallace, and K. Moe, "Refinements in the determination of satellite drag coefficients: method for resolving density discrepancies", *J. of Guidance, Control, and Dynamics*, vol. 16, pp. 441–445, 1993.

[38] NASA, "Spacecraft aerodynamic torques", *NASA/SP-8058*, vol. NASA Space Vehicle Design Criteria (Guidance and Control), p. 37, Jan. 1971.

[39] Z. Várhegyi, "Trajectory analysis and preliminary mission design for QB50", Master's thesis, von Karman Institute for Fluid Dynamics, Jun. 2011.

[40] P. M. Mehta, C. A. McLaughlin, and E. K. Sutton, "Drag coefficient modeling for GRACE using Direct simulation Monte Carlo", *Advances in Space Research*, vol. 52, no. 12, pp. 2035–2051, 2013, ISSN: 0273-1177.

[41] O. Montenbruck and E. Gill, *Satellite Orbits Models, Methods, and Applications*, First Edition, Springer, Ed. Springer, 2000.

[42] J. Gregory and P. Peters, "A measurement of the angular distribution of 5 ev atomic oxygen scattered off a solid surface in earth orbit", *Rarefied Gas Dynamics, Proc. Intl. Symposium*, vol. 15, 1987.

[43] S. Varma, "Control of satellites using environmental forces : aerodynamic drag / solar radiation pressure", PhD thesis, Ryerson University, 2011.

[44] S. Meir, C. Stephanos, T. Geballe, and J. Mannhart, "Higly-efficient thermoelectronic conversion of solar energy and heat into electric power", *Journal of Renewable and Sustainable Energy*, vol. 5, no. 4, 2013.

[45] *Ztj photovoltaic cell, emcore*, Sep. 2012. [Online]. Available: http://www.emcore.com/space-photovoltaics/space-solar-cells/.

[46] D. Schultheiß, "Gravity compensation of deployable solar arrays for small spacecraft", Master's thesis, Universität Stuttgart, Nov. 2003.

[47] D. Puckert, G. Herdrich, and S. Fasoulas, "Development of a cavity calorimeter for the inductively heated plasma generator IPG6-S", *AIAA-Pegasus Student Conference, Portiers, France*, 2012.

[48] NASA, *Gemini 2 reentry*, Jan. 1965. [Online]. Available: http://www.spacemedicineassociation.org/timeline/1965/1965/Gemini%202%20Reentry.jpg.

[49] F. F. Chen, *Introduction to Plasma Physics and Controlled Fusion*, Second Edition. Springer, Jun. 2006, vol. 1. Plasma Physics.

[50] G. Herdrich, "Aufbau, Qualifikation und Charakterisiserung einer induktiv beheizten Plasmawindkanalanlage zur Simulation atmosphärischer Eintrittsmanüver", Dissertation, Institut für Raumfahrtsysteme, Universität Stuttgart, 2004.

[51] M. Dropmann, "Development and set-up of an inductively heated plasma source for basic investigations", *Internal document, Institute for space systems, Universität Stuttgart*, vol. IRS 11-S10, 2011.

[52] G. Herdrich, R. Laufer, M. Dropmann, R. A. Gabrielli, T. W. Hyde, and H.-P. Roeser, "Establishing a hybrid plamsa environment simulation facility", *Frontiers in Aerospace Engineering*, vol. 1, no. 1, Nov. 2012.

[53] EM-Technik, *Em materials*, 2014. [Online]. Available: http://www.em-technik.com/products/technical-information/materials.html.

[54] S. Shinohara, H. Nishida, T. Tanikawa, T. Hada, I. Funaki, and K. P. Shamrai, "Development of electrodeless plasma thrusters with high-density helicon plasma sources", *IEEE Transactions on Plasma Science*, vol. 42, no. 5, pp. 1245–1254, May 2014.

[55] J. Waldock, D. Kirtley, and J. Slough, "Electromagnetic optimization of frc-based pulsed plasma", *33rd International International Electric Propulsion Conference, The George Washington University, USA*, Oct. IEPC-2013-376.

Acknowledgements

The biggest thank is to my dad, my mum and my brothers and sister, because they always have been supporting me with love and trust in every step of my life.

Thank to my friends, whom are now mostly spread all over the world, but I can annoy them, as always, like they would be right here. Thank you.

I want to thank Georg Herdrich for the opportunity and the trust he gave me, to develop my thesis at the IRS. A big thank to Tomeu, for his help and really great patience with me during this work, he worked very hard together with me for getting this work done. I want to mention also Tony Schönherr who gave me helpful and useful tips for my thesis from Japan.
Further thanks to all the IRS group who made me feel very welcome from the very first days in Stuttgart.

Thank to Dr. Daniele Pavarin for his support to my work from Italy.

A. Diagrams

In this appendix some diagrams which are helping to clarify some statements done through this master thesis.

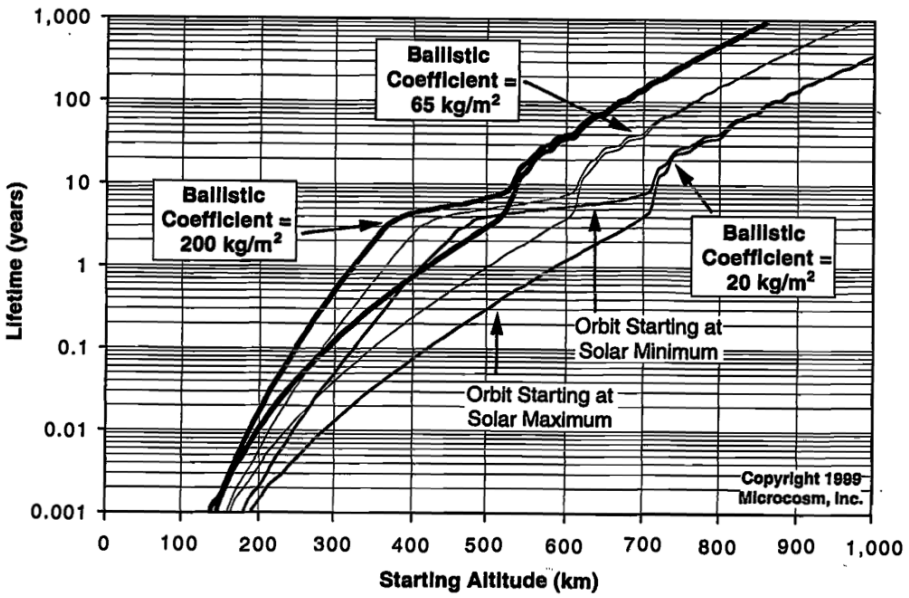

Figure 8.3: S/C Lifetime as a function of altitude, solar cycle phase, ballistic coefficient [29, p. 210].
For each ballistic coefficient, the upper curve represents launch at the start of solar minimum when there will be a low level of decay and the lower curve represents launch at the start of solar maximum when the satellite will decay most rapidly for several years. Data generated with SatLife program 1998.

B. Matlab scripts

In this Appendix the Matlab scripts used for the calculations are displayed in form of block diagrams.
In this appendix the logic scheme of the following Matlab scripts will be presented:

- 8.1 Molar Mass;
- 8.2 Heat Fluxes;
- 8.3 Knudsen Number;
- 8.4 Drag in Free Molecular Flow.

8.1 Molar Mass Script

This scripts calculates the atmosphere's molar mass as a function of the altitude by using the NRLMSISE-00 Model.

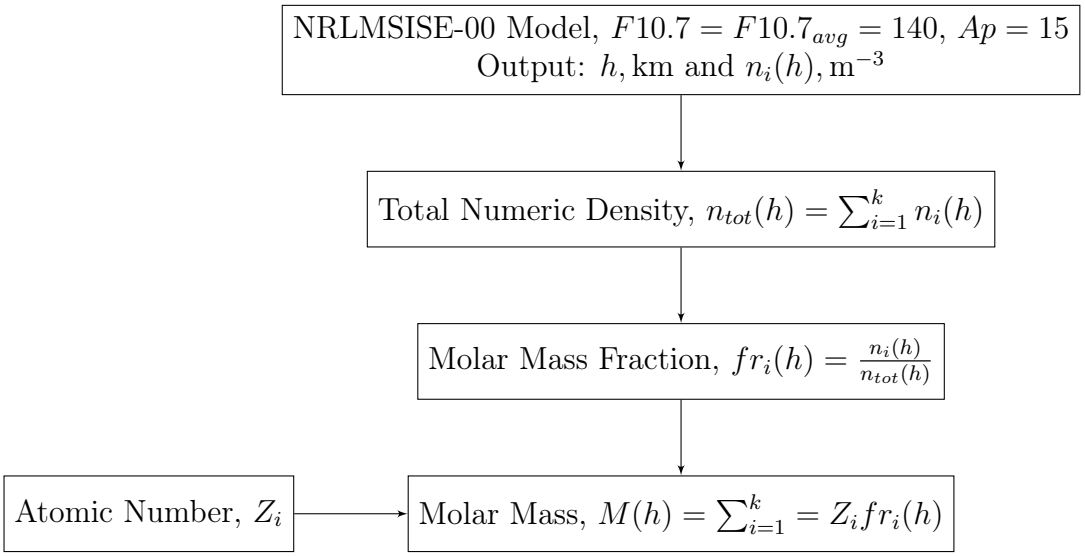

8.2 Temperature and Heat Flux Calculation

This script calculates the different heat fluxes acting on the S/C in the altitude range considered using the NRLMSISE-00 model and values of standard heat fluxes from literature.

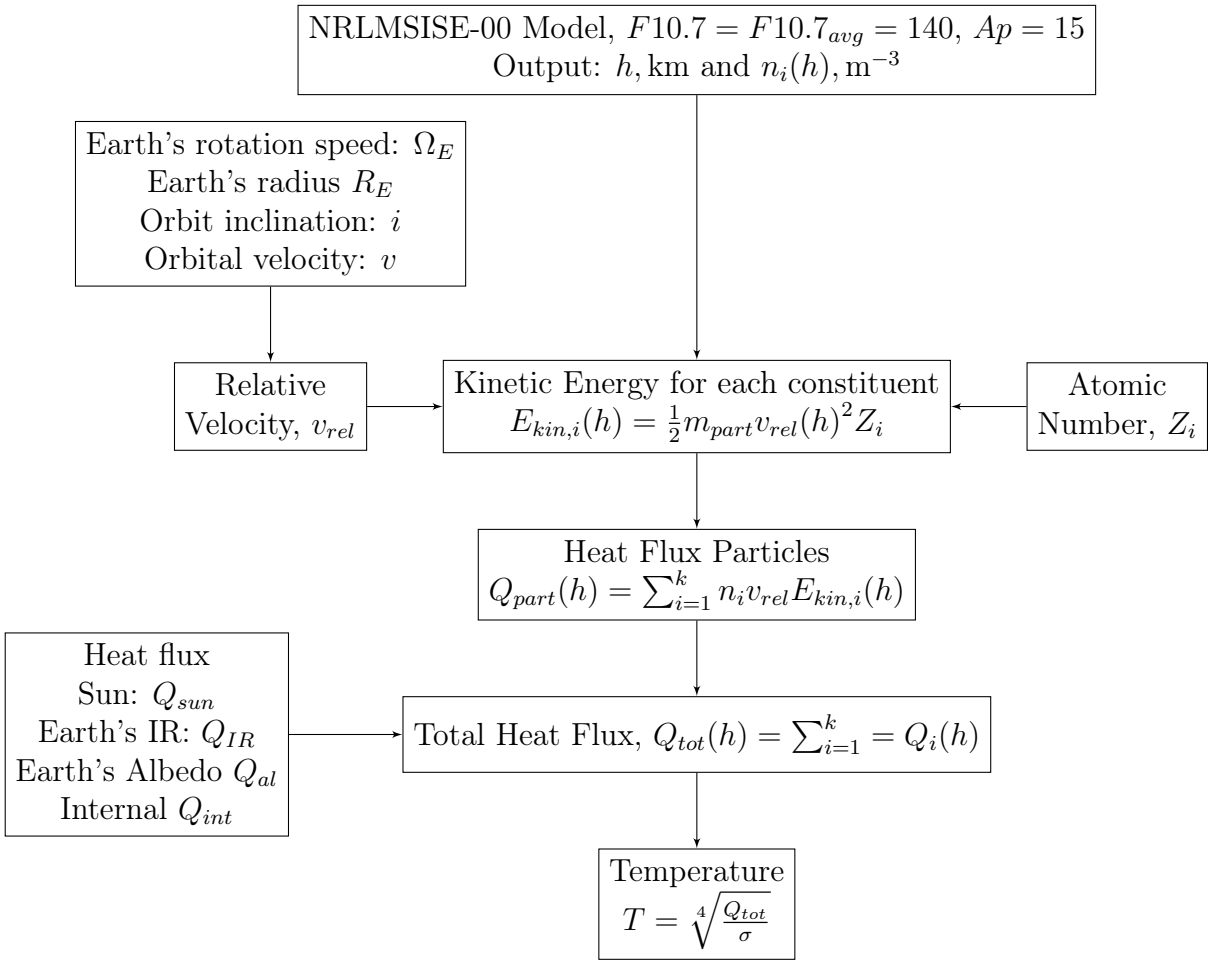

8.3 Knudsen Number Calculation

This scripts calculates the Knudsen number as a function of altitude for different mean lengths using the NRLMSISE-00 model.

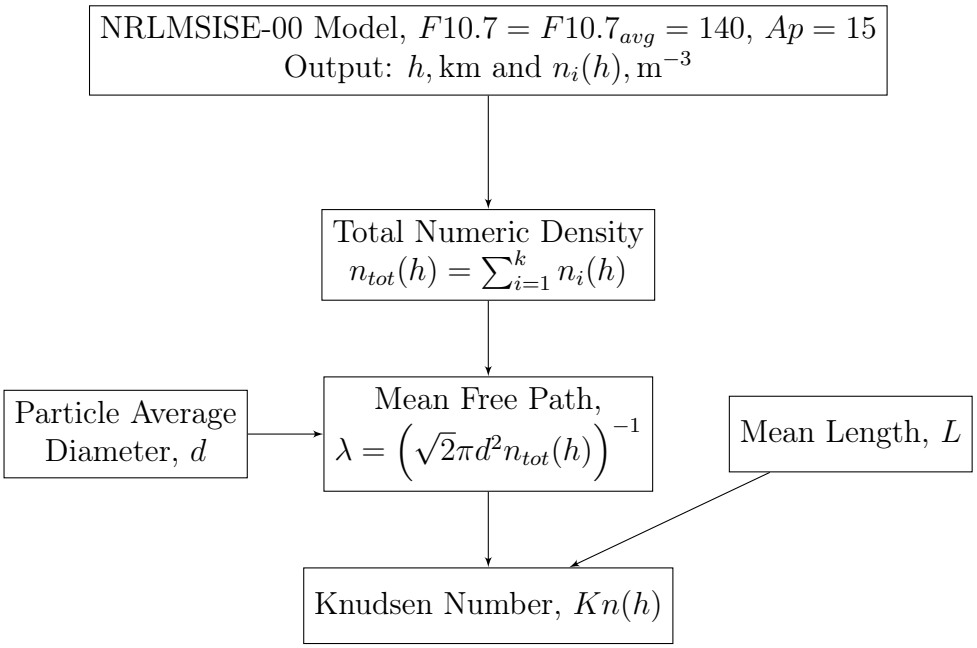

8.4 Drag Calculation Script

This script calculates the drag in free molecular flow as a function of the altitude using the NRLMSISE-00 model with Eq. 8.1, 8.2 and 8.3.

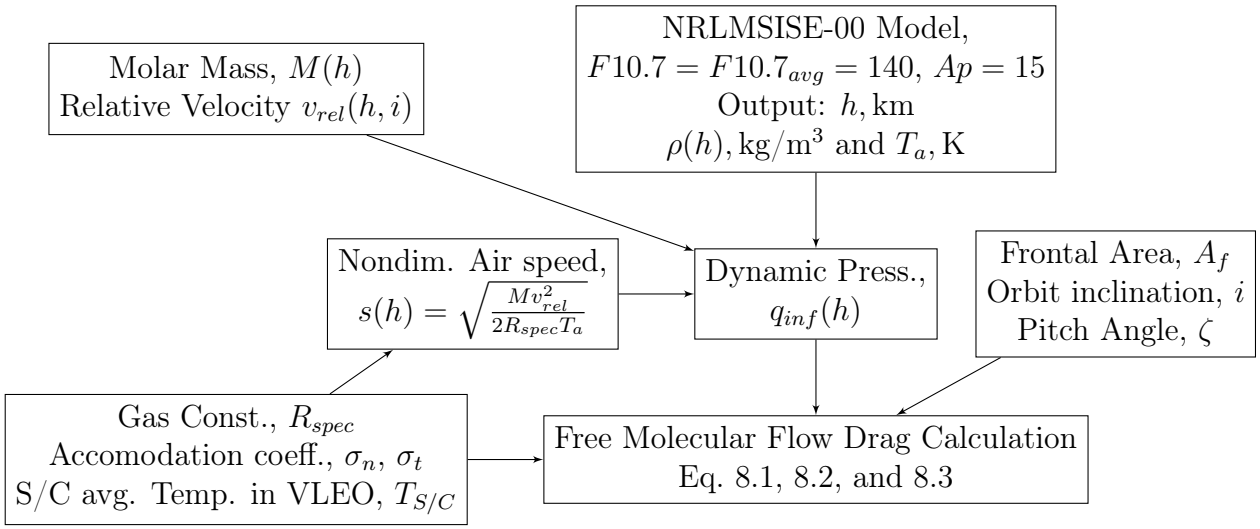

$$\vec{F}_D = A_f \left[-\hat{n}p + \left(\hat{n}\sin\zeta - \hat{v}_{rel} \right) \left(\frac{\tau}{\cos\zeta} \right) \right] \tag{8.1}$$

$$\begin{aligned} \frac{p}{q_\infty} =& \left\{ \left[\frac{2-\sigma_n}{\sqrt{\pi}} \right] \sin\zeta + \frac{\sigma_n}{2s} \sqrt{\frac{T_s}{T_a}} \right\} \left\{ \frac{1}{s} e^{-s^2 \sin\zeta^2} + \sqrt{\pi} [1 + \operatorname{erf}(s\sin\zeta)] \sin\zeta \right\} + \\ &+ \left[\frac{2-\sigma_n}{2s^2} \right] [1 + \operatorname{erf}(s\sin\zeta)] \end{aligned} \tag{8.2}$$

$$\frac{\tau}{q_\infty} = \sigma_t \left\{ \frac{1}{s\sqrt{\pi}} e^{-s^2 \sin\zeta^2} + \operatorname{erf}(s\sin\zeta)] \sin\zeta \right\} \tag{8.3}$$

8.5 Solar Array

In this section the procedure for the calculation of the S/A degradation, and the calculation of the panel and string surface is shown.
The reference values for the solar cell are those referred to [45].
S/C lifetime is chosen to be 7 years, considering a SSO, the angle θ, that is the angle between the solar panel and the sun vector is considered to be 0°. The solar cell manufacturer gives a minimum average cell efficiency in BOL of $\eta_{cell} = 29.5\%$ and a cell area of $A_{cell} = 26.6 \times 10^{-4}\text{m}^2$ operating at maximum power with a voltage of $V_{oc} = 2.726\,\text{V}$.
Considering a standard solar power flux of $P_I = 1353\,\text{W/m}^2$ the following procedure has been followed.
The calculation of the life degradation L_d is done considering a 2.75% degradation per year for GaAs:

$$L_d = \left(1 - \frac{2.75}{100}\right)^{S/C_{life,y}} \tag{8.4}$$

The inherent degradation is an average from literature of $I_d = 0.77$.
The power density at BOL is calculated as:

$$P_{BOL} = P_0 I_d \cos\theta = \eta_{cell} P_I I_d \cos\theta \tag{8.5}$$

as well as the voltage:

$$V_{BOL} = V_{oc} I_d \cos\theta \tag{8.6}$$

The respective EOL values are for power:

$$P_{EOL} = P_{BOL} L_d \tag{8.7}$$

and for voltage:

$$V_{EOL} = V_{BOL} L_d \tag{8.8}$$

From these equations the S/A area, the number of cells are calculated

$$A_{S/A} = \frac{P_{req}}{P_{EOL}} \tag{8.9}$$

$$n_{cell} = \frac{V_{req}}{V_{EOL}} \tag{8.10}$$

following the required S/A module area for the voltage and the numbers of modules required

$$A_{S/AV} = \frac{A_{cell}}{n_{cell}} \tag{8.11}$$

$$n_{S/AV} = \frac{A_{S/A}}{A_{S/AV}} \tag{8.12}$$

C. Experiments Data

In this Appendix the experimental results of the tests are shown. Afterwards the checklist followed for every experiment and the emergency checklist are attached.

8.6 Low Mass Flows Air

8.6.1 0.550 kV

IPG6-S	GAS: AIR	SCREEN VOLTAGE: 0.550kV	PROJECT: RAM-EP	DATE: 13/05/2014	OPERATORS: ROMANO F., MASSUTI B.	
Mass Flow Controller	**Calibrated mass flow**	**Power Anode**	**Current Anode**	**P_inj**	**P_tank**	**P_cal**
%	mg/s	kW	A	Pa	Pa	W
2	0.24534345565434	0.5	1.6	36	26	126.2
7	0.61296296274724	0.8	1.6	39	29	128.2
5	0.70633657234543	1	1.6	39	29	133
10	1.76584144736842	1	1.65	41	28	145.5
15	2.8945108777938	1	1.7	44	30	153.15
20	4.02318030821917	1	1.7	46	32	145
35	7.45742342353453	1	1.7	52	38	157.05
50	10.8983847887324	1.5	1.8	56	38	166.65
70	15.4497935222672	1.5	1.8	62	43	176.7
80	17.7673428127772	1	1.7	65	46	187.75
90	20.1304256916996	1	1.7	66	46	203.1

8.6.2 0.850 kV

IPG6-S	GAS: AIR	SCREEN VOLTAGE: 0.850kV	PROJECT: RAM-EP	DATE: 13/05/2014	OPERATORS: ROMANO F., MASSUTI B.	
Mass Flow Controller	Calibrated mass flow	Power Anode	Current Anode	P_inj	P_tank	P_cal
%	mg/s	kW	A	Pa	Pa	W
2	0.24534345565434	0.5	2.3	39	27	74.42
7	0.61296296274724	0.8	2.3	38	28	76.34
5	0.70633657234543	1	2.3	39	27	82.59
10	1.76584144736842	1	2.3	41	28	86.91
15	2.8945108777938	1	2.3	43	30	91.71
20	4.02318030821917	1	2.3	46	32	115.7
35	7.45742342353453	1	2.3	53	36	132
50	10.8983847887324	1.5	2.3	60	38	140.2
70	15.4497935222672	1.5	2.4	67	42	149.3
80	17.7673428127772	2	2.4	71	46	191.55
90	20.1304256916996	2	2.5	74	50	194.45

8.6.3 1.000 kV

IPG6-S	GAS: AIR	SCREEN VOLTAGE: 1.000kV	PROJECT: RAM-EP	DATE: 13/05/2014	OPERATORS: ROMANO F., MASSUTI B.	
Mass Flow Controller	Calibrated mass flow	Power Anode	Current Anode	P_inj	P_tank	P_cal
%	mg/s	kW	A	Pa	Pa	W
2	0.24534345565434	0.5	2.7	38	27	68.18
7	0.61296296274724	0.9	2.7	37	27	70.58
5	0.70633657234543	0.9	2.7	39	27	85.51
10	1.76584144736842	1	2.7	41	28	90.94
15	2.8945108777938	1	2.7	43	30	109.95
20	4.02318030821917	1	2.7	46	32	122.4
35	7.45742342353453	1	2.7	53	35	116.3
50	10.8983847887324	1.5	2.7	61	39	140.1
70	15.4497935222672	1.6	2.6	69	45	147.4
80	17.7673428127772	2	2.6	74	48	193.9
90	20.1304256916996	2	2.7	78	49	200.25

8.7 Low Mass Flows Oxygen

8.7.1 0.550 kV

IPG6-S	GAS: OXYGEN	SCREEN VOLTAGE: 0.550kV	PROJECT: RAM-EP	DATE: 13/05/2014	OPERATORS: ROMANO F., MASSUTI B.	
Mass Flow Controller	Calibrated mass flow	Power Anode	Current Anode	P_inj	P_tank	P_cal
%	mg/s	kW	A	Pa	Pa	W
2	0.24691358016	0.5	1.6	37	26	145
7	0.6172839504	0.5	1.6	38	28	153.15
5	0.711315789473684	0.5	1.6	39	28	149.4
10	1.77828947368421	0.5	1.6	40	30	152.2
15	2.9149152847873	0.5	1.6	43	31	153.15
20	4.0515410958904	0.8	1.6	44	30	154.6
35	6.01070094539844	1	1.7	50	33	157.3
50	10.9752112676057	1.25	1.7	56	38	167.65
70	15.5587044534412	1	1.7	61	42	167.6
80	17.8925909494232	1	1.7	63	45	161.85
90	20.2723320158102	1	1.7	67	47	166.65

8.7.2 0.850 kV

IPG6-S	GAS: OXYGEN	SCREEN VOLTAGE: 0.850kV	PROJECT: RAM-EP	DATE: 13/05/2014	OPERATORS: ROMANO F., MASSUTI B.	
Mass Flow Controller	Calibrated mass flow	Power Anode	Current Anode	P_inj	P_tank	P_cal
%	mg/s	kW	A	Pa	Pa	W
2	0.24691358016	0.5	2.4	36	27	118.6
7	0.6172839504	0.5	2.4	37	28	123.85
5	0.711315789473684	0.5	2.4	38	29	121
10	1.77828947368421	0.5	2.35	40	29	125.3
15	2.9149152847873	0.5	2.35	43	30	125.3
20	4.0515410958904	0.6	2.3	45	32	133.95
35	6.01070094539844	1	2.3	52	34	159.9
50	10.9752112676057	1	2.3	59	39	170.45
70	15.5587044534412	1.4	2.3	68	43	182
80	17.8925909494232	1.5	2.35	73	45	189.65
90	20.2723320158102	1.6	2.4	74	46	195.45

8.7.3 1.000 kV

IPG6-S	GAS: OXYGEN	SCREEN VOLTAGE: 1.000kV	PROJECT: RAM-EP	DATE: 13/05/2014	OPERATORS: ROMANO F., MASSUTI B.	
Mass Flow Controller	Calibrated mass flow	Power Anode	Current Anode	P_inj	P_tank	P_cal
%	mg/s	kW	A	Pa	Pa	W
2	0.24691358016	0.5	2.8	36	27	133.95
7	0.6172839504	0.5	2.8	38	29	135.85
5	0.711315789473684	0.5	2.8	39	28	137.8
10	1.77828947368421	0.5	2.8	40	30	128.5
15	2.9149152847873	0.5	2.75	42	30	117.65
20	4.0515410958904	0.6	2.7	45	30	116.65
35	6.01070094539844	1	2.7	52	35	123.85
50	10.9752112676057	1	2.7	58	39	140.65
70	15.5587044534412	1.2	2.7	68	44	157.5
80	17.8925909494232	1.5	2.7	73	45	158.95
90	20.2723320158102	1.5	2.7	78	46	175.5

8.8 High Mass Flows Air

8.8.1 0.550 kV

IPG6-S	GAS: AIR	SCREEN VOLTAGE: 0.550kV	PROJECT: RAM-EP	DATE: 16/05/2014	OPERATORS: ROMANO F., MASSUTI B.
Mass Flow	Power Anode	Current Anode	P_inj	P_tank	P_cal
mg/s	kW	A	Pa	Pa	W
20	1	1.7	74	55	182
40	1.25	1.7	98	72	185.85
60	1.25	1.7	120	92	188.25
80	1.25	1.75	140	110	197.85
100	1.5	1.75	160	120	202.15
120	1.5	1.8	190	140	195.2

8.8.2 0.850 kV

IPG6-S	GAS: AIR	SCREEN VOLTAGE: 0.850kV	PROJECT: RAM-EP	DATE: 13/05/2014	OPERATORS: ROMANO F., MASSUTI B.
Mass Flow	Power Anode	Current Anode	P_inj	P_tank	P_cal
mg/s	kW	A	Pa	Pa	W
20	2	2.5	74	50	225.65
40	2.5	2.6	120	67	235.25
60	2.5	2.6	130	88	239.6
80	2.5	2.6	150	110	235.7
100	2.5	2.6	170	120	237.65
120	2.5	2.6	190	140	222.3

8.8.3 1.000 kV

IPG6-S	GAS: AIR	SCREEN VOLTAGE: 1.000kV	PROJECT: RAM-EP	DATE: 13/05/2014	OPERATORS: ROMANO F., MASSUTI B.
Mass Flow	Power Anode	Current Anode	P_inj	P_tank	P_cal
mg/s	kW	A	Pa	Pa	W
20	2	2.9	87	50	171.9
40	3	3.15	120	70	231.9
60	3.25	3.1	140	86	278
80	3.25	3.1	160	100	280.4
100	overload	overload	overload	overload	overload
120	overload	overload	overload	overload	overload

8.9 High Mass Flows Oxygen

8.9.1 0.550 kV

IPG6-S	GAS: OXYGEN	SCREEN VOLTAGE: 0.550kV	PROJECT: RAM-EP	DATE: 16/05/2014	OPERATORS: ROMANO F., MASSUTI B.
Mass Flow	Power Anode	Current Anode	P_inj	P_tank	P_cal
mg/s	kW	A	Pa	Pa	W
20	1	1.7	76	53	113.3
40	1.25	1.8	97	72	131.65
60	1.5	1.8	120	85	165.15
80	1.5	1.8	140	100	167.1
100	1.5	1.8	160	110	165.15
120	1.5	1.8	180	130	171.45

8.9.2 0.850 kV

IPG6-S	GAS: OXYGEN	SCREEN VOLTAGE: 0.850kV	PROJECT: RAM-EP	DATE: 16/05/2014	OPERATORS: ROMANO F., MASSUTI B.
Mass Flow	Power Anode	Current Anode	P_inj	P_tank	P_cal
mg/s	kW	A	Pa	Pa	W
20	1.8	2.45	83	52	163.3
40	2.5	2.65	110	69	186.75
60	2.6	2.7	130	84	188.7
80	3	2.7	150	90	234.8
100	3	2.75	170	110	238.65
120	3	2.8	190	130	245.85

8.9.3 1.000 kV

IPG6-S	GAS: OXYGEN	SCREEN VOLTAGE: 1.000kV	PROJECT: RAM-EP	DATE: 16/05/2014	OPERATORS: ROMANO F., MASSUTI B.
Mass Flow	Power Anode	Current Anode	P_inj	P_tank	P_cal
mg/s	kW	A	Pa	Pa	W
20	1.8	2.75	86	51	159.9
40	2.8	3	110	68	204.1
60	3.3	3.1	140	83	230
80	3.5	3.15	160	100	249.2
100	3.5	3.15	180	110	251.2
120	overload	overload	overload	overload	overload

8.10 Checklist

8.10.1 Operation Checklist

I

IPG6-Stuttgart Universität Stuttgart

IPG6-S Test Checklist Nr:.....

DATE, START TIME	
RESPONSIBLE	
GAS	
PROJECT	

Start-up procedure

- ■ ***0. PRELIMINARY OPERATIONS***
- ☐ All O-rings are inserted
- ☐ Install generator over tank
- ☐ All metallic components grounded
- ☐ Screw water connections
- ☐ Screw electric connections
- ☐ Fix injector head
- ☐ Grounding far from oscill. circ. el. conn.
- ☐ Screw pressure sensor to injector head
- ☐ Tank **ventil** closed
- ☐ ALCATEL pump **ventil** open
- ☐ PC and electronics ON
- ☐ Sensor positions and connections OK
- ■ ***A. VACUUM AND WATER SUBSYSTEMS***
- ☐ **Run ALCATEL** Vacuum Pump
- ☐ Tank pressure < 5.0E-1 mbar, 50Pa
- ☐ **Open** all water sources
- ☐ **Run** Secondary Water Pump
- ☐ No pressure increment observed
- ☐ Check all water connections
- ☐ **Run VAROVAC** Vacuum Pump
- ☐ Tank pressure achieved: .....Pa
- ☐ **Run** Power Supply Water Pump
- ☐ Green LED in both water flow meters
- ■ ***B. GAS SUPPLY SUBSYSTEM***
- ☐ Check connections & valves are closed
- ☐ **Run** heater (if present)
- ☐ **Open** bottle vale
- ☐ **Open** reducer valve
- ■ ***C. INITITALIZATION AND SET UP***
- ☐ Install **Faraday** box over IPG
- ☐ Check Mass flow controller **inlets clear**
- ☐ Select mass flow rate .....mg/s
- ☐ Tank pressure is stable at .....Pa
- ☐ Injector pressure is stable at .....Pa
- ☐ **Run "pwkmain"**
- ☐ Water ***temperatures*** stable at: fill in
- ■ ***D. POWER SUBSYSTEM***
- ☐ **Run** power supply
- ☐ Press "reset": all red lights turn off
- ☐ Pulse mode is **off**
- ☐ Screen voltage at **minimum**
- ☐ **High voltage (HS) ON**
- ☐ Wait for the voltage to reach 100 V
- ☐ **High frequency (HF) ON**
- ☐ Check plasma colour
- ☐ Stay 60s at minimum & check sensors
- ■ ***D. IN PULSE MODE ONLY***
- ☐ Select "Pulse Time" and "Pause Time"
- ☐ Select Grid voltages "1st and 2nd"

■ ***Temperatures***
■ **Inj. Aus: °C / Gen. Aus: °C**
■ **Zu Wasser: °C / Kal. Aus: °C**

Experiment control

Voltage, kV	100									
Power, kW										
Anode Current, A										
Mass flow, mg/s										
Start Time, s	0									
End Time, s										
Pulse Time	0									
Pause Time	0									

II

IPG6-Stuttgart Universität Stuttgart

Shutdown procedure

- ***E. POWER SUPPLY***
- High frequency (HF) **OUT**
- High voltage (HS) **OUT**
- Power supply turned **off**
- ***F. VACUUM***
- **Stop** mass flow rate
- **VAROVAC** Vacuum Pump Switched **off**
- **ALCATEL** Vacuum Pump Switched **off**
- Tank main valve **open** (gradually)
- Press **ESC** to finish "pwkmain"
- ***G. WATER SUBSYSTEM***
- Water pumps switched **off**
- Water sources all **closed**

- ***H. GAS SUPPLY SUBSYSTEM***
- Main valve **closed**
- **Expell** gas from flow controller
- Secondary valve **closed**
- Gas pipe **unplugged**
- Valve assembly **unplugged** from
- Bottle cap **screwed**
- ***I. FINAL PROCEDURES***
- Faraday Box **removed** from IPG6-S
- **Save** data from PC, file:
- **Shut down** PC and electronics
- ***J. IF ANY FAILURE OR IF REQUIERED***
- **Unscrew** all IPG connections
- **Remove** generator from Tank
- **Install** glass window to close the Tank
- Note any damage

8.10.2 Emergency Checklist

IPG6-Stuttgart Universität Stuttgart

IPG6-S EMERGENCY CHECK LIST

In case of WATER leakage into tank: water must not enter VAROVAC pump!
(If change of the oil required)

In Phase A of the checklist **(no power applied):**

1. **Unplug** ALCATEL pump (and VAROVAC if on);
2. **Open** main tank **VENTIL** to refill;
3. **Disconnect** VAROVAC **flange** (before the L junction to pump);
4. **Remove generator** and leave **top** tank open;
5. Let Tank and Pump duct dry for a couple of days;
6. Disconnect **pressure gauges** and **mass flow controllers** → check for water
7. Run pump for half an hour with **Air Ballast on** (read VAROVAC manual for reference).

In Phase D of the checklist **(power applied):**

1. Press **emergency button** to **switch off** VAROVAC and Power supply;
2. **Unplug** ALCATEL pump;
3. **Open** main tank **VENTIL** to refill;
4. **Disconnect** the VAROVAC **flange** (before the L junction to the pump);
5. See points 4, 5, 6, 7 of the checklist before.

D. Drawings

In this Appendix the technical drawings realized for the design for the introduction of the new water cooled bottom flange are presented.
In particular the drawings for these list of modified and new components are shown:

- 8.11 Plexiglas Case;
- 8.12 Adapter;
- 8.13 Bottom Flange;
- 8.14 Bottom Closure.

8.11 Plexiglas Case

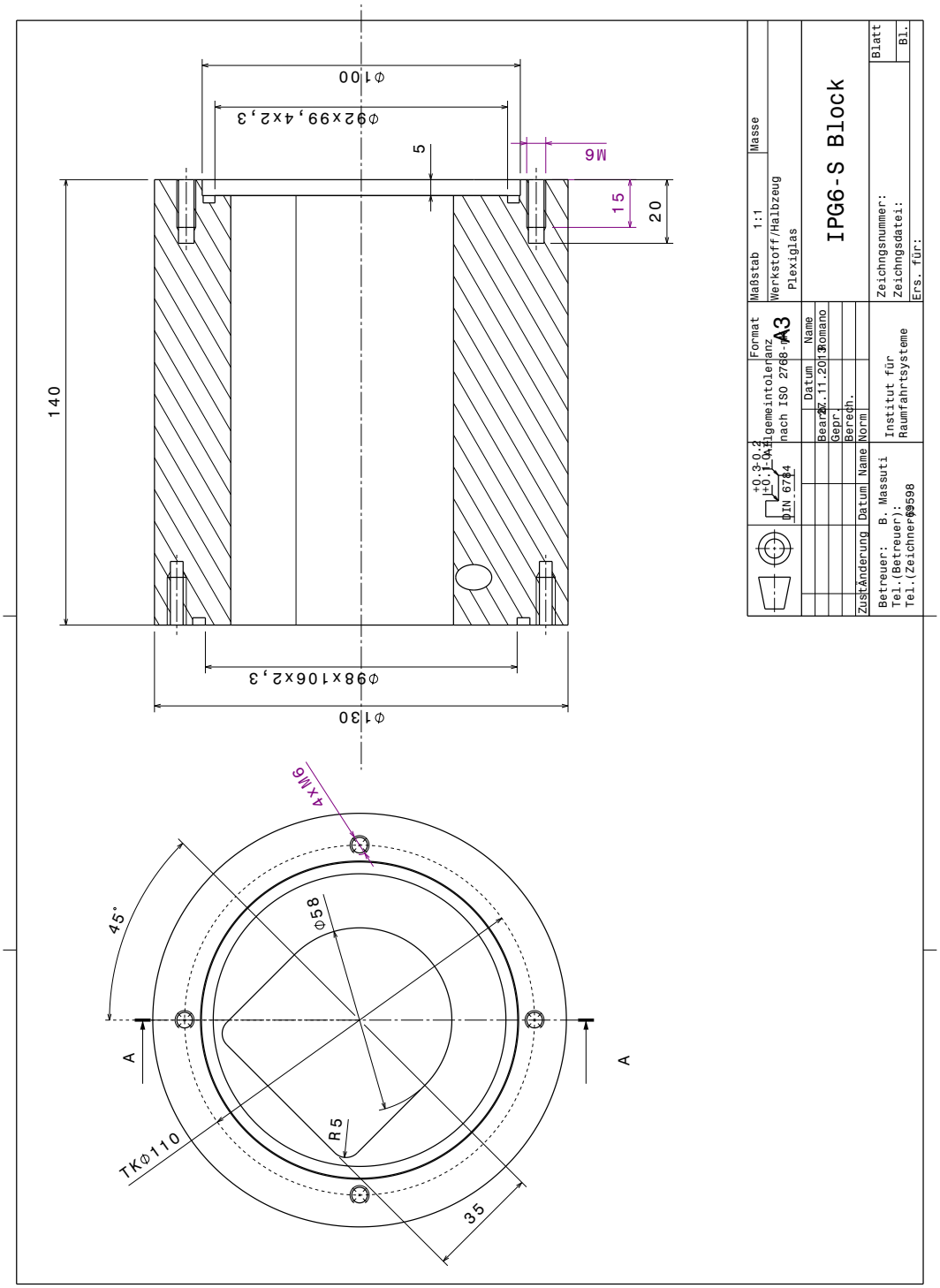

Figure 8.4: Modified Plexiglas case of IPG6-S.

8.12 Adapter

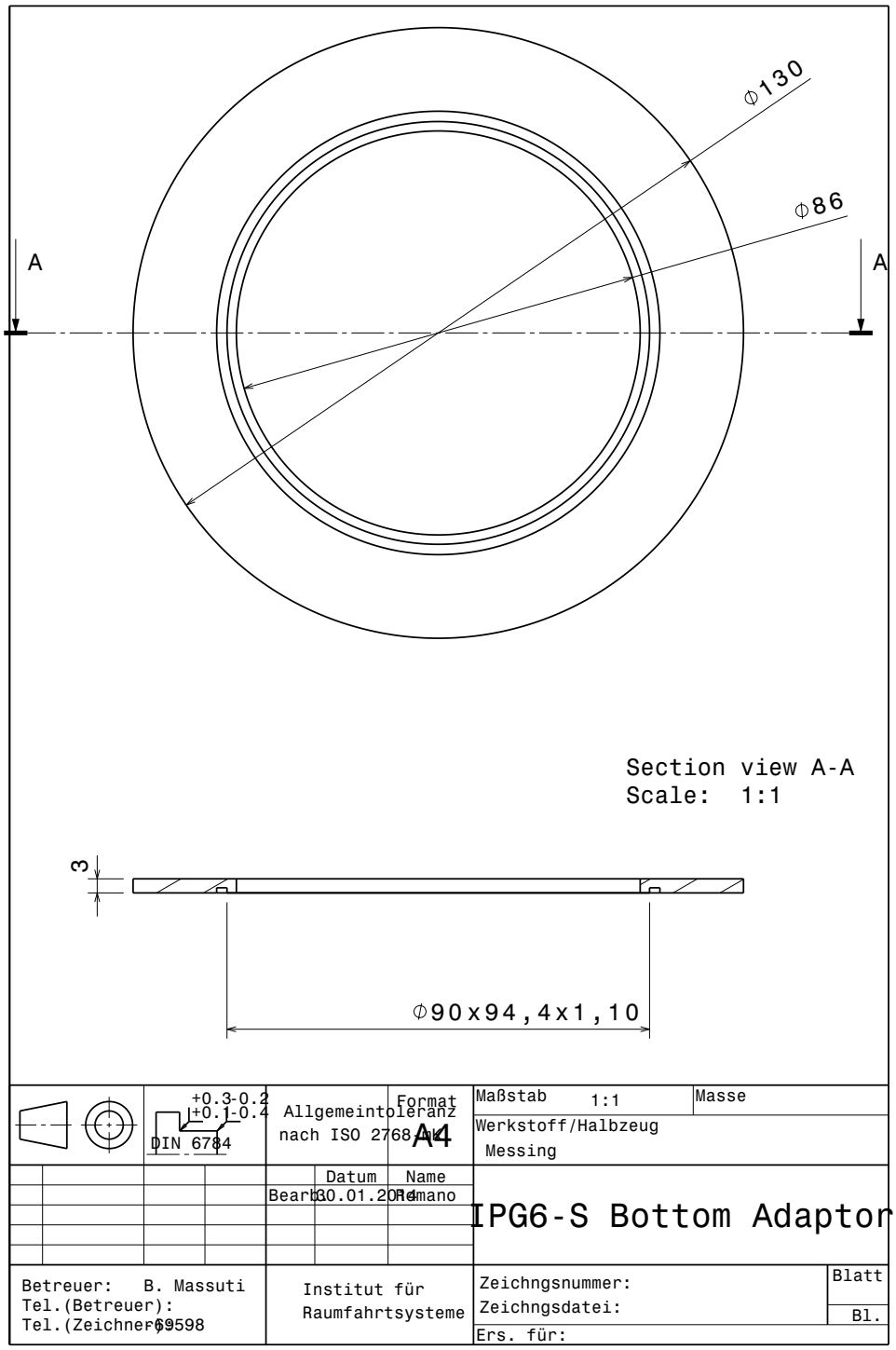

Figure 8.5: Adapter for the connection of the bottom flange to the vacuum chamber.

8.13 Water Cooled Bottom Flange

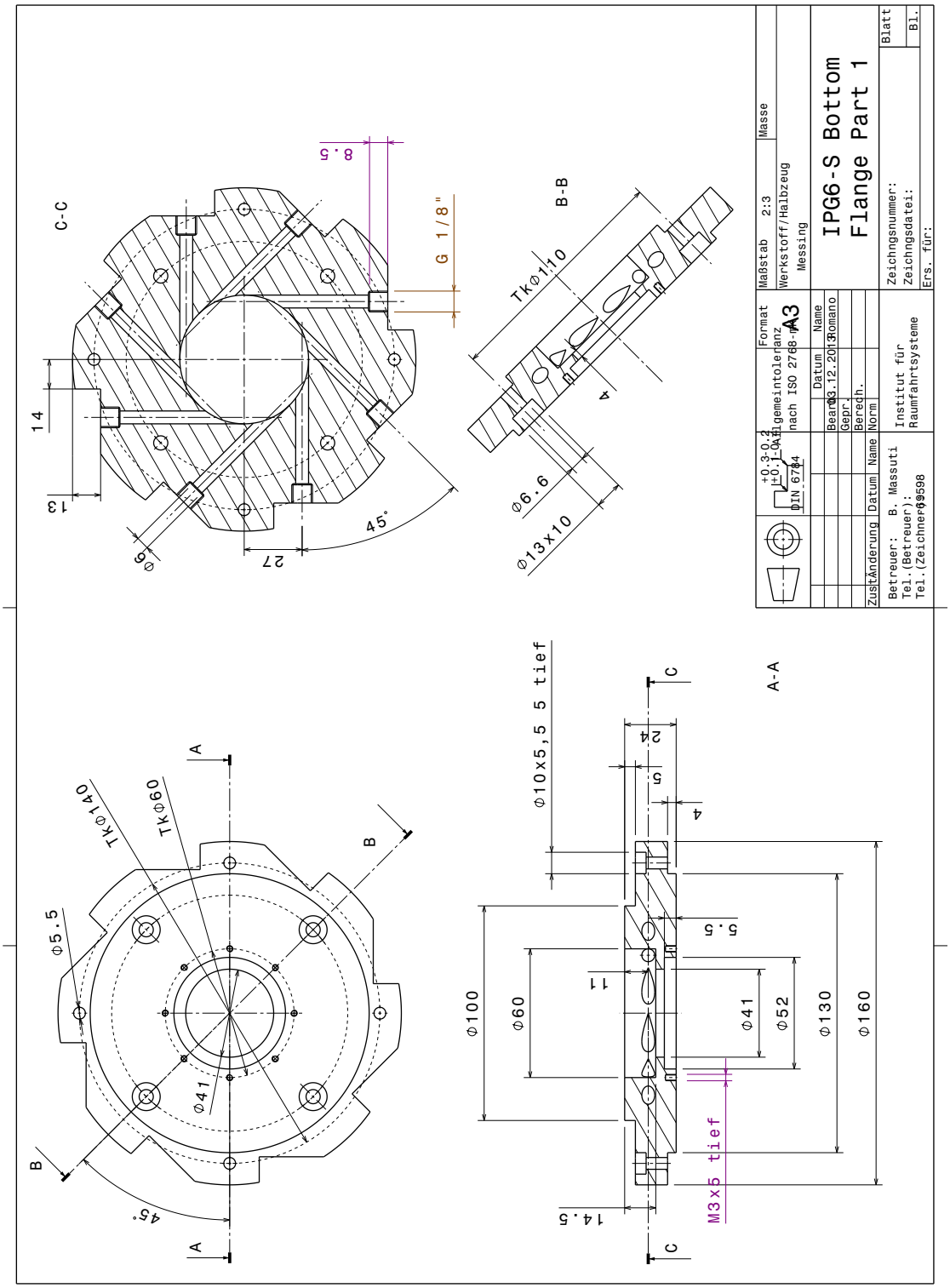

Figure 8.6: Water Cooled Bottom Flange.

8.14 Closure of the Water Cooled Bottom Flange

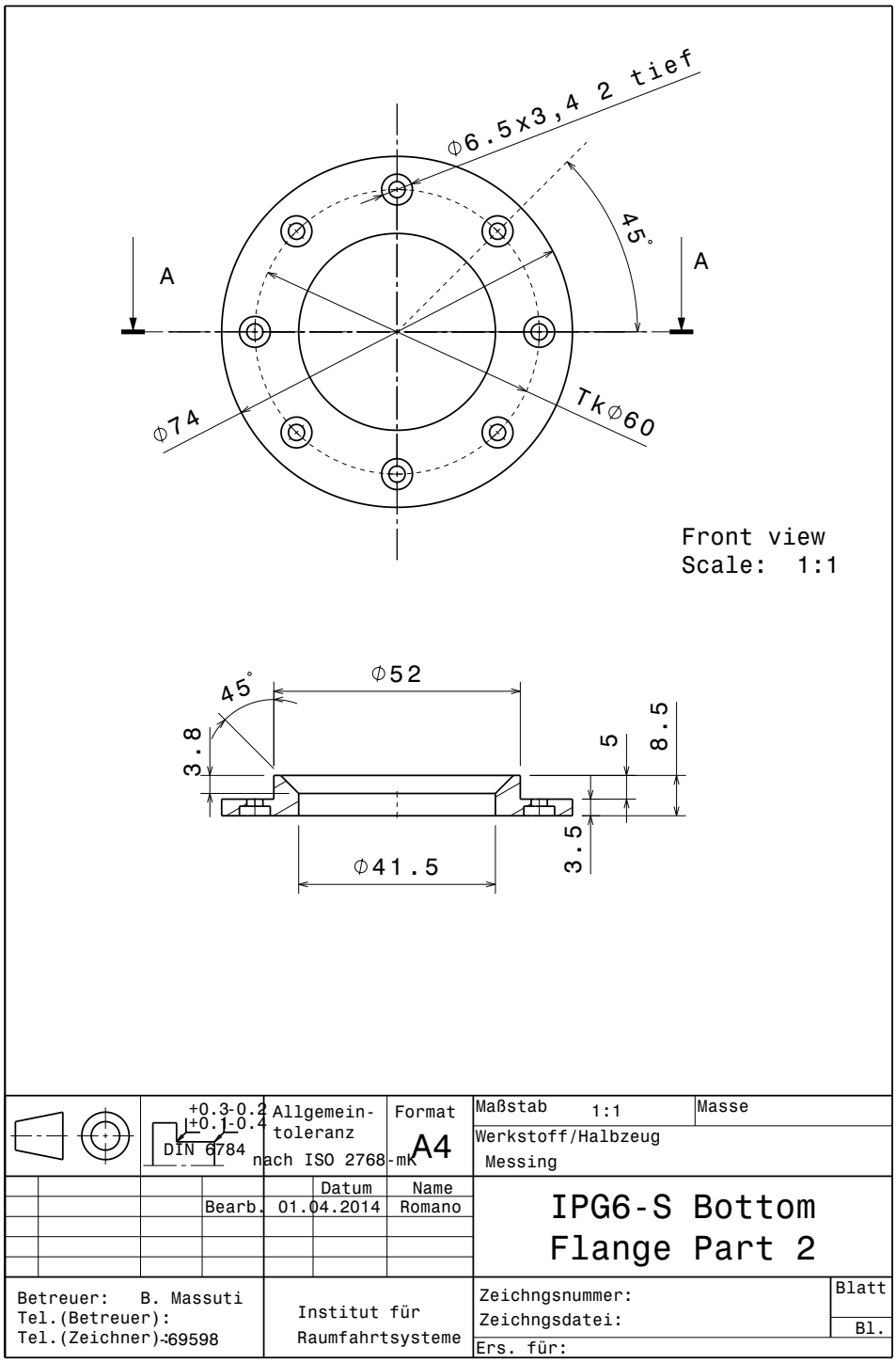

Figure 8.7: Closure of the Water Cooled Bottom Flange.